Università degli Studi di Napoli Federico II
Dipartimento di Fisica E. Pancini

Dottorato di ricerca in
FISICA
Ciclo XXXII
Coordinatore: Prof. S. Capozziello

Novel technique to measure Lepton Universality ratio R_K at NA62

Settore scientifico disciplinare: FIS-01

Dottorando:
Michele Corvino

Tutor:
Prof. Fabio Ambrosino

Anni 2017/2020

"Ma se io avessi previsto tutto questo,
dati causa e pretesto,
forse farei lo stesso"
Francesco Guccini

Contents

List of Figures

Acknowledgments

This work would have not been possible without some people I want sincerely to thank.

Thanks to my supervisors, Prof. Fabio Ambrosino and Prof. Paolo Massarotti, for having given me the opportunity to follow my path, always offering me their support and experience to help me.

Thanks to Dr. Karim Massri, for having taught me so many things in the time I have spent at CERN. His advices throughout these years have been fundamental.

Thanks to the members of the NA62 collaboration, I have learnt something from all of you.

Thanks to my family: my parents, my sisters, Anna, Ernesto, Felice and Alessia, for having always been there whenever I needed.

Last but not least, many thanks to Lia: thank you for the help, suggestions and patience you had during these tough years. The best is yet to come.

Introduction

The Standard Model (SM) of elementary particles is the theory describing three of the four fundamental interactions. Despite the great success of its predictions, SM is incomplete for several reasons and therefore it can be considered only an effective theory. In order to find a way towards a complete theory, great experimental efforts are made to find new physics which is not described by the SM. For experiments at accelerators, two main approaches can be adopted: the first one, used at LHC, is the direct search at high energy, making particle beam of several TeV collide to have the possibility to observe new resonances. The second path to physics beyond SM is the indirect search with high intensity experiments: in this case the beam energies are orders of magnitude lower but they are used to perform precise measurements of very well predicted observables, in order to spot any discrepancy. New physics can enter into higher order diagrams as virtual particles in loops, allowing to probe mass scales even higher than those explored by direct searches.

In this pioneering context, a still relevant role is played by particles discovered more than 70 years ago: K mesons. Kaons, observed for the first time by Rochester and Butler, have been the main characters in many extraordinary results of the last century, from flavour oscillations to the discovery of indirect and direct CP violations. Nowadays, they represents a very clean initial state to perform new physics searches with high intensity beam. The NA62 experiment, which started its data taking in 2016, is using an high intensity kaon beam to search for new physics beyond the Standard Model. Its main goal is the measurement of the branching ratio of the ultra-rare decay $K^+ \to \pi^+ \nu\bar{\nu}$ but the physics program is quite broad.

In the recent years, interesting results have been obtained from the test of one of the key properties of the SM, Lepton Universality: measurements performed by the B factories and LHC suggested possible deviations between the theoretical predictions and the experimental values. In kaon physics,

Lepton Universality can be tested measuring the ratio $R_K = \Gamma(K^+ \to e^+\nu(\gamma))/\Gamma(K^+ \to \mu^+\nu(\gamma))$. Despite the remarkable precision obtained by the previous measurements - few ‰- the theoretical uncertainty is still one order of magnitude smaller: to spot any evidence of new physics, then, big efforts from the experimental point of view are needed.

The statistical error on R_K is dominated by the number of $K^+ \to e^+\nu(\gamma)$ decays collected: this limit can be easily overcome by NA62 due to its high intensity beam. The experiment takes data in simultaneous trigger streams, with different configurations: the most suitable stream for this search has no downscale factors but it contains a veto condition on muons. A new approach, then, is adopted: $K^+ \to \mu^+\nu(\gamma)$ sample is extracted collecting the events where muons decay in flight into positrons, allowing to use the same trigger setup for both samples with subsequent cancelation of most systematic effects. This new measurement will also profit from the improved experimental layout of NA62, in terms of particle identification and background suppression.

The thesis is structured as follows:

- In Chapter 1, an overwiew on lepton universality - and particularly R_K - is presented, from both theoretical and experimental points of view;
- In Chapter 2, the NA62 experiment is described;
- In Chapter 3, the experimental strategy, the sample used and the event selection is reported;
- In Chapter 4, the R_K result with its statistical and systematic uncertainties is presented;
- Finally, in Appendix A a separate study, related to $K^+ \to \pi^+\nu\bar{\nu}$ analysis, is also reported.

Chapter 1

State of the art on R_K

1.1 R_K in the Standard Model

The interactions between elementary particles are successfully described by the Standard Model (SM) [1–3]. The model is built on a gauge group $SU(3)_C \otimes SU(2)_L \otimes U(1)_Y$, where the labels correspond to the QCD color charge, left handed chirality and hypercharge respectively. Lepton and quark fields are separated into their left-handed and right-handed chirality components and arranged into doublets and singlets of $SU(2)_L$ respectively; neutrinos are described as purely left-handed fields as ν_R have not been observed so far. Gauge fields emerges from imposing the local gauge invariance, while the Higgs [4, 5] mechanism provides lepton masses.

Being a non-abelian gauge theory, one of the key properties of the SM is lepton universality: the coupling constant between the gauge bosons and the leptons is the same indipendently from lepton flavour; Yukawa interactions break this symmetry, so that muon, electron and tau are different particles only because of their masses. In the recent years, the interest on lepton universality tests has grown because of the observations of "tensions" between the experimental results and the theoretical predictions, especially in $b \to s$ transitions. If confirmed, these discrepancies could clearly indicate the presence of new physics beyond the SM.

Hints on the need of an extended theory arrived also from neutrino physics, expecially from the discovery of neutrino oscillations. This phenomenon is related to the violation of another symmetry involving leptons, lepton family number; unlike lepton universality, lepton family number is

an "accidental" symmetry because it is not a consequence of a conserved current in the lagrangian, as stated by Noether's theorem. In order to have oscillations, neutrinos mass terms have to be present in the lagrangian, while this is not the case for the SM as right-handed chirality neutrinos are not included in the model; therefore, an explanation of the process is possible only with an extended theory.

Lepton universality tests are performed studying leptonic or semileptonic decays of hadrons, comparing the results for two modes which differ only by the lepton flavours in the final state; in order to reduce systematic uncertainties, it is useful to compute the ratios between the two decay widths

$$R_h = \frac{\Gamma(h \to l_\alpha \nu_\alpha + others)}{\Gamma(h \to l_\beta \nu_\beta + others)} \quad or \quad R_h = \frac{\Gamma(h \to l_\alpha^+ l_\alpha^- + others)}{\Gamma(h \to l_\beta^+ l_\beta^- + others)} \tag{1.1}$$

where the two ratios are referred to tests in charged or neutral current transitions respectively and *others* represent the remaining particles in the final states.

In lepton universality tests via charged current processes in B sector, the measured quantities are the ratios

$$R_{D^{(*)}} = \frac{BR(B \to D^{(*)} \tau \bar{\nu})}{BR(B \to D^{(*)} l \bar{\nu_l})} \tag{1.2}$$

where the lepton l can be muon or electron. In Figure 1.1 the measurements of R_D and R_{D^*} performed by BaBar, Belle and LHCb [6–14] are reported. The SM predictions for both ratios are shown as well in the plot: R_D and R_{D^*} exceed the theoretical values by 2.3 and 3 standard deviations respectively, for a combined discrepancy of about 2.8σ.

A comparable disagreement with respect to the SM expectation has been obtained also in $b \to sll$ transitions, measuring the ratios:

$$R_{K^{(*)}} = \frac{BR(B \to K^{(*)} \mu^+ \mu^-)}{BR(B \to K^{(*)} e^+ e^-)} \tag{1.3}$$

Lepton universality implies that this ratios should be 1, as differences due to lepton masses can be neglected in heavy meson decays. The most recent measurements of the two observables, performed by the LHCb collaboration [16, 17], are reported in Figure 1.2. The experimental values are compatible with the theoretical prediction at the level of 2.5σ for R_K and $2.2 - 2.5\sigma$ for R_{K^*}.

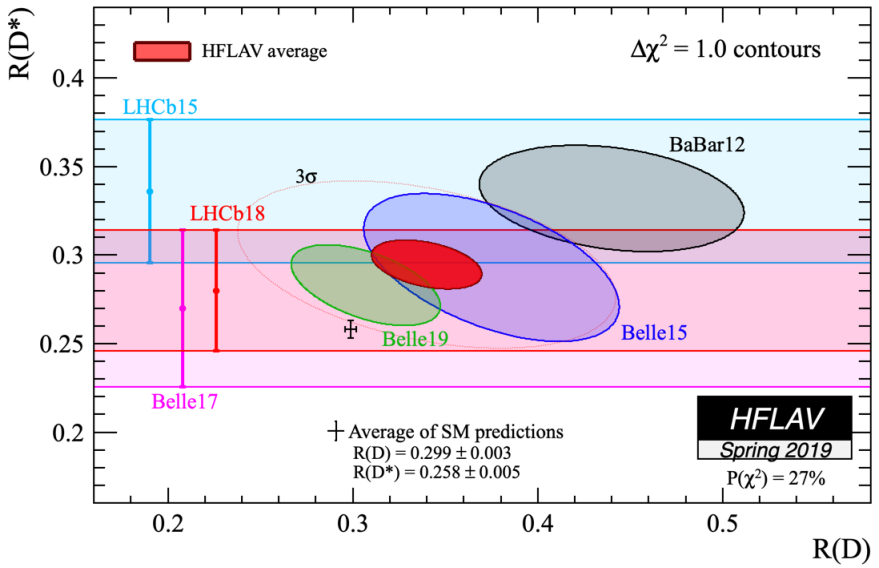

Figure 1.1: Combination of the measurements of R_D and R_{D^*} performed by BaBar, Belle and LHCb. The SM predictions are also reported on the plot. Figure from [15]

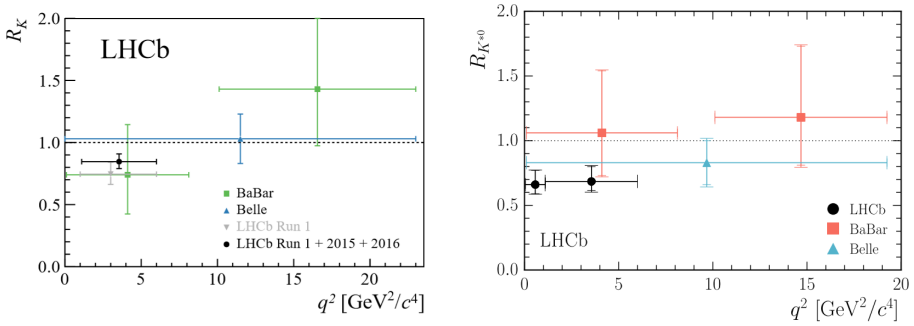

Figure 1.2: Results obtained by LHCb and by B-factories for R_K (left) and R_{K^*} (right); the dashed line at 1 represent the theoretical expectation in case of lepton universality. Figures from [18] and [19]

Given these results, the natural question that can be raised is whether this tension can be observed also in light mesons decays.

In kaon physics, lepton universality can be effectively tested measuring the ratio R_K,

$$R_K = \frac{\Gamma(K^+ \to e^+\nu_e)}{\Gamma(K^+ \to \mu^+\nu_\mu)} \tag{1.4}$$

which has several features that makes it suitable for new physics searches. The first reason is represented by the helicity suppression. The V-A structure of the charged current weak interactions selects the left-handed chirality components of the fields; for a massless particle, as neutrinos can be reasonably considered, chirality and helicity are the same. On the other hand, this property does not belong to massive leptons: the momentum conservation in case of a two body decay, such as K_{l2}, translates into the choice of the "wrong" helicity component for the charged lepton, whose amplitude is proportional to m_l/E_l. Despite the larger phase space, then, K_{e2} decay mode is suppressed with respect to the muon channel by a factor $\approx m_e^2/m_\mu^2$. The helicity suppression makes the prediction for R_K very small in the SM, allowing tiny contributions coming from new physics to be visible.

The second reason is that, being a ratio between two decay widths of the same meson, most of the theoretical uncertainties contained in the hadronic matrix element are canceled out, leading to a very precise computation. From the experimental point of view, most of the systematic uncertainties are the same for the two modes and therefore the experimental measurement can be very precise as well.

Finally, the experimental signatures for R_K are very clean, as two body decays are characterized by a sharp peak around zero in the missing mass distribution between the lepton and the kaon, corresponding to the neutrino masses.

R_K can be precisely estimated using the low energy effective theory of the QCD, the Chiral Perturbation Theory (χPT): in this context, amplitudes are expressed as a series of power of the meson masses (using the parameter $p \sim m_K/4\pi F_\pi$, with $F_\pi \sim 93$ MeV) and the electric charge.

The expression for R_K can be written as the sum of a constant term, which depends only on the kaon and leptons masses, and radiative correction, expanded in powers of p^2 [20]:

$$R_K = R_K^{(0)}\left(1 + \Delta_{e^2p^2} + \Delta_{e^2p^4} + \Delta_{e^2p^6} + ...\right) \tag{1.5}$$

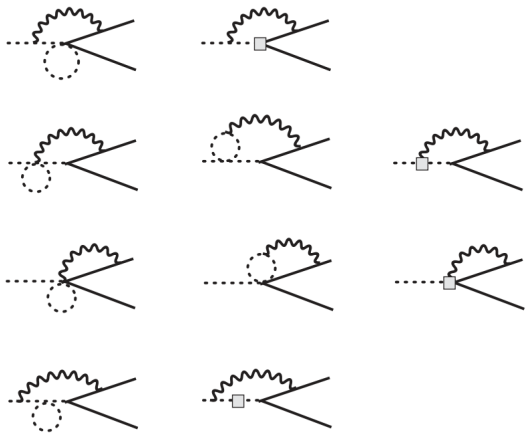

Figure 1.3: Feynman diagrams giving contribution to R_K at $O(e^2p^4)$. Dashed lines correspond to the kaon, solid lines to leptons and wavy lines to photons. The squares represent the $O(p^4)$ vertex of the effective lagrangian.

with

$$R_K^{(0)} = \frac{m_e^2}{m_\mu^2}\left(\frac{m_K^2 - m_e^2}{m_K^2 - m_\mu^2}\right)^2 . \tag{1.6}$$

The leading term, $\Delta_{e^2p^2}$, corresponds to a pointlike approximation of the kaon, while the most general parametrization for the NLO contribution, neclecting terms in $(m_e/m_\rho)^2$ is given by [20]:

$$\Delta_{e^2p^4} = \frac{\alpha}{\pi}\frac{m_\mu^2}{m_\rho^2}\left(c_2 \log\frac{m_\rho^2}{m_\mu^2} + c_3 + c_4(m_\mu/m_K)\right) + \frac{\alpha}{\pi}\frac{m_K^2}{m_\rho^2}\tilde{c_2}\log\frac{m_\mu^2}{m_e^2} \tag{1.7}$$

where $\alpha = e^2/4\pi$, c_i are dimensionless coefficients, and the mass of the ρ meson arises from the vector meson dominance. All the one-particle-irreducible (1PI) diagrams contributing to R_K up to $O(e^2p^4)$ are reported in Figure 1.3. The computation of the coefficients c_i is done using the physical meson mass to $O(p^4)$ in the $O(e^2p^2)$ amplitude and calculating one loop "effective" diagrams with appropriate form factors that are derived to $O(p^4)$ in d-dimensions.

The results obtained following this approach are summarized in Table 1.1.

$\Delta_{e^2p^2}$ (%)	c_2	c_3	c_4	$\tilde{c}_2$	$\Delta_{e^2p^4}$ (%)
-3.786	4.3	-4.73	0.22	0.0784	0.135

Table 1.1: Results from NLO evaluation of radiative corrections to R_K [20].

Including NLO radiative correction, SM prediction for R_K is [20]:

$$R_{K_{SM}} = (2.477 \pm 0.001) \times 10^{-5} \tag{1.8}$$

1.2 Beyond SM contributions to R_K

Many different models of new physics beyond the Standard Model (BSM) include the possibility of violating lepton flavour universality. From an experimental perspective, however, only models which can give a sizeable contribution to R_K are discussed in this work.

Lepton flavour violation in light mesons decays can be obtained in two ways: the first possibility is via corrections to the SM charged current vertex $lW\nu$, while the other way is through a modification of the four fermions interaction due to the presence of a new Lorentz structure in the lagrangian. Two examples of both approaches are presented in the following sections.

The first mechanism can involve new physics at a scale Λ_{NP} which gives loop corrections to the vertex; however, this contribution can be written as

$$\frac{\alpha}{4\pi}\frac{m_W^2}{\Lambda_{NP}^2}, \tag{1.9}$$

well below any experimental limit; on the other hand, tree-level modifications of the vertex are possible in presence of sterile neutrinos and they can give significant results.

1.2.1 Sterile neutrinos

In the SM, left-handed chirality components of fermion fields are organized into doublets of $SU(2)_L$, while right-handed components are represented by singlets. In the case of leptons, one has:

$$\begin{pmatrix}\nu_e\\ e\end{pmatrix} \quad , \quad \begin{pmatrix}\nu_\mu\\ \mu\end{pmatrix} \quad , \quad \begin{pmatrix}\nu_\tau\\ \tau\end{pmatrix} \tag{1.10}$$

Mass terms, which mix left and right chirality components, are not allowed in the lagrangian since the would break the gauge invariance. Right handed neutrinos are not included in the model as they do not interact with any gauge boson but their addition can lead to neutrino mass terms, necessary to explain the phenomenon of neutrino oscillation, well established after many experimental confirmations. The presence of righ-handed neutrino lead to a mixing matrix for leptonic sector, similar to the CKM.

In this context, the charged current lagrangian can be written as [21]:

$$-\mathcal{L}_{cc} = \frac{g}{\sqrt{2}} U_{\nu}^{ji} \bar{l}_j \gamma^{\mu} \mathrm{P_L} \nu_{\mathrm{i}} \mathrm{W}_{\mu}^{-} + \mathrm{c.c.} \tag{1.11}$$

where P_L is the left-handed chirality projector while U_{ν}^{ji} represents the leptonic mixing matrix, where the index $j = 1, ...n_{\nu}$ refers to the number of neutrino states and $i = 1, 2, 3$ labels the lepton flavour. In case of three generations of neutrinos, the mixing matrix corresponds to the PMNS matrix [22] and no lepton flavour violation can be observed: since neutrinos are not detected, the total amplitude is proportional to $U_{\nu} U_{\nu}^{\dagger} = 1$ and lepton flavour universality is preserved. The scenario changes introducing at least one sterile neutrino, namely an additional neutrino field - not necessarily right-handed - that do not interact with the gauge bosons. In this case, the leptonic mixing matrix becomes a $n_{\nu} \times 3$ matrix and the mixing between left-handed letptons is expressed by a 3×3 block of U_{ν}:

$$U_{PMNS} \rightarrow \tilde{U}_{PMNS} = (\mathbb{1} - \eta) U_{PMNS}. \tag{1.12}$$

The deviation from the unitary matrix is parametrized by the matrix η: it is clear, then, that a contribution to tree-level interactions can be sizeable only in presence of large mixing terms with the left-handed neutrinos.

In presence of $1, 2...3 + N_s$ neutrinos, semileptonic kaon decays are described by the following effective lagrangian [21]:

$$H_{eff} = \frac{4 G_F}{\sqrt{2}} V_{CKM}^{qq'} \left(U_{\nu}^{ij} \bar{q} \gamma_{\mu} P_L q' l_j \gamma^{\mu} P_L \nu_i \right) \tag{1.13}$$

The expression for R_K can be written in a compact form [21]:

$$R_K = \frac{\Sigma_i F^{i1} G^{i1}}{\Sigma_k F^{k2} G^{k2}}. \tag{1.14}$$

with

$$F^{ij} = |U_{\nu}^{ij}|^2 \tag{1.15}$$

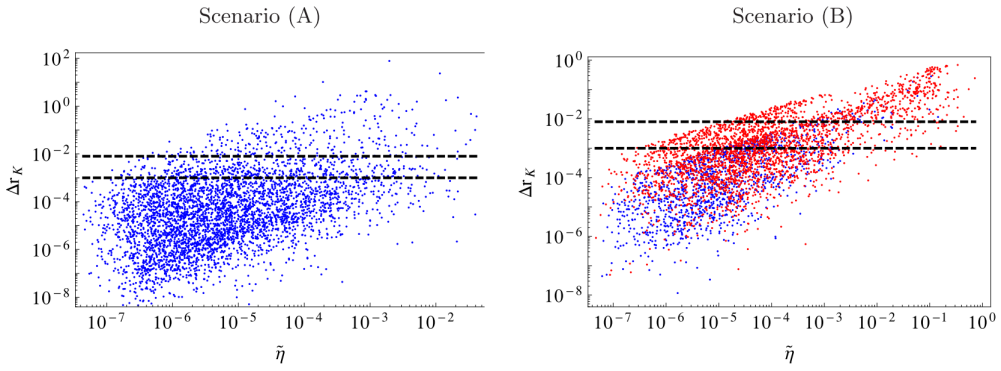

Figure 1.4: ΔR_K for a Inverse SeeSaw (ISS) model. Scenario (A) represent a configuration in which all the sterile neutrinos are lighter than the kaon but heavier than the active neutrinos, while Scenario (B) refers to a regime where the sterile neutrinos are heavier than the kaon. Figure from [21].

$$G^{ij} = \left[m_K^2\left(m_{\nu_i}^2 + m_{l_j}^2\right)\right]\left[\left(m_K^2 - m_{l_j}^2 - m_{\nu_i}^2\right) - 4m_{l_j}^2 m_{\nu_i}^2\right]^{1/2} \tag{1.16}$$

The meaning of the two factors is the following: F^{ij} contains the effect of the new interactions - not present in the SM - while G^{ij} the mass-dependent factors. Neglecting the presence of sterile neutrino, i.e. in the limit of $F^{ij} = \delta^{ij}$ and $m_{\nu_i} = 0$, Equation (1.6) is recovered.

This procedure is model independent: as example, it can be applied to Inverse See-Saw mechanism [23]. Two scenarios are considered:

- Scenario A: sterile neutrinos are lighter than the kaon but heavier than the left-handed neutrinos, $m_\nu << m_N < m_K$

- Scenario B: all the sterile neutrinos are heavier than the kaon.

Figure 1.4 shows ΔR_K as a function of $\tilde{\eta}$, which reflects the deviation from the unitarity of the leptons mixing matrix ($\tilde{\eta} = 1 - |\tilde{U}_{PMNS}|$). Both cases lead to configurations where the effect of ΔR_K is up to O(1), however Scenario (A) is strongly excluded by constraints from CMB and X-rays observations. From the figure, a large set of values for $\tilde{\eta}$ that translate into a deviation of R_K from the SM by few permilles can be observed, justifying the interest of a more precise measurement.

1.2.2 SUSY

SUSY contributions to R_K [24] arise from one loop diagrams involving several particles, such as charged or neutral Higgs scalars, charginos, neutralinos and sleptons. This various contributions can be grouped in two cathegories:

- lepton flavour conserving (LFC) interactions, where the kaon decays as in the SM: $K \to l\nu_l$;
- lepton flavour violating (LFV) interactions, where all the cases $K \to l_i\nu_k$ have to be considered.

In the first case, as stated before, the contribution to R_K is well below the experimental sensitivity. As an example, the term coming from Higgs scalar can be written as [24] $\Delta R_{KSUSY} = \alpha/4\pi \frac{m_\mu^2 - m_e^2}{m_H^2} tan\beta$, where $tan\beta$ is the ratio between the vacuum expectation values of the two Higgs. Even with $tan\beta = 50$, the value of ΔR_{KSUSY} cannot be larger than 10^{-6}.

The second case is more interesting. The presence of LFV terms in a model that includes at least two Higgs doublets is almost unavoidable. Despite the naive idea that LFV contributions are even smaller than LFC ones, this is not what happens since some of the former can be enhanced. Allowing LFV terms, the definition of R_K changes:

$$R_K = \frac{\Sigma_i \Gamma(K \to e\nu_i)}{\Sigma_i \Gamma(K \to \mu\nu_i)} \qquad i = e, \mu, \tau \tag{1.17}$$

The dominant contribution is represented by the charged Higgs exchange, expressed by the following effective coupling (Figure 1.5) [24]:

$$lH^+\nu \to \frac{g_2}{\sqrt{2}} \frac{m_\tau}{m_W} \Delta_R^{3l} tan^2\beta \tag{1.18}$$

The terms Δ_R^{3l} come from Bino exchange; in the mass insertion (MI) approximation, they are given by [24]

$$\Delta_R^{3l} \simeq \frac{\alpha_1}{4\pi} \mu M_1 m_R^2 \delta_{RR}^{3l} \left[I'(M_1^2, \mu^2, m_R^2 - (\mu \leftrightarrow m_L) \right] \tag{1.19}$$

where μ is the Higgs mixing parameter, M_1 is the Bino mass and α_1 its coupling, $m_{L(R)}^2$ and $\delta_{XX}^{3l} = (\tilde{m}_l^2)_{XX}/m_X^2$ $X = L, R$ are respectively are the left-left (right-right) and the off diagonal terms of the slepton mass matrix and I' is the loop function. As shown in [25, 26], $\Delta_R^{3l} \leq 10^{-3}$.

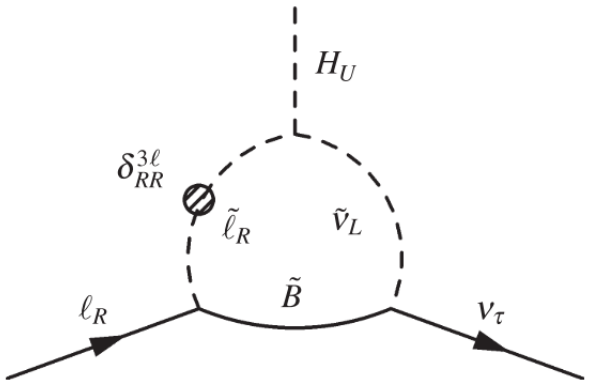

Figure 1.5: Contribution to effective $lH^+\nu$ coupling

The LFV contribution to R_K can be written, then, as [24]:

$$R_K^{LFV} \simeq R_K^{SM}\left[1+\left(\frac{m_K^4}{m_H^4}\right)\left(\frac{m_\tau^2}{m_e^2}\right)|\Delta_R^{31}|^2 tan^6\beta\right] \tag{1.20}$$

while the term proportional to Δ_R^{32} is suppressed by a factor m_e^2/m_μ^2. Despite large part of the parameter space $(tan\beta, M_H)$ has been excluded by LHC experiments, a sizeable contribution to R_K due to charged Higgs exchange is still possible: using $\Delta_R^{31} = 5\cdot 10^{-4}$, $tan\beta = 30$ and $M_H = 350\text{GeV/c}^2$ one obtains $R_K^{LFV} \simeq R_K^{SM}\,(1+0.009)$.

It is possible, then, that some region of the SUSY parameters space leads to a deviation of R_K from the SM up to few percents.

1.3 Experimental status

The most precise measurement of R_K has been obtained in 2013 by the NA62 collaboration[27] analyzing data collected in 2007-2008 with simultaneous $K^\pm$ beams. The experimental setup reused the NA48/2 beamline (Figure 1.6), with a beam momentum of 74 GeV/c and an rms of 1.4 GeV/c; the two components of the beam were selected by the first two dipoles of an achromat and by two slits in a iron-copper proton beam dump, which could block one of the two beams. Momenta from charged particles produced by kaon decays were measured by four Drift CHambers (DCHs), placed in an helium tank at atmospheric pressure downstream the fiducial volume. Triggers from charged

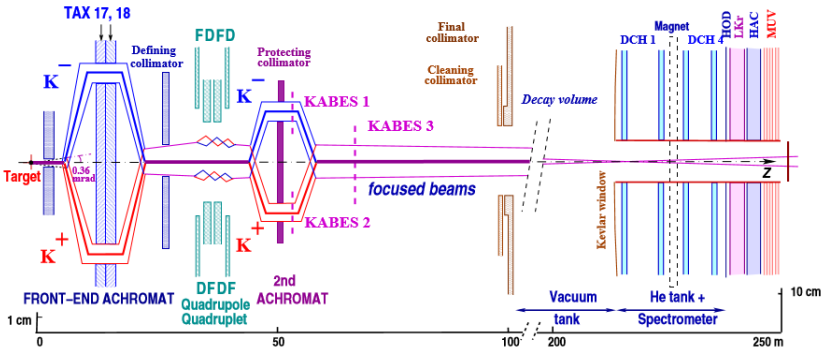

Figure 1.6: Scheme of the beamline used by NA48/2 experiment at CERN. Figure from [28].

particles were produced by a charged hodoscope and particle identification was provided by an electromagnetic liquid krypton calorimeter, with excellent energetic and spatial resolution. More details on the NA62-RK setup can be found in [28].

Two minimum bias trigger masks were used to select the samples. Both channels were selected requiring the coincidence between two planes of DCHs and a multiplicity in the spectrometer compatible with a single track; in addition, the K_{e2} trigger mask asked for at least 10 GeV of energy deposit in the calorimeter. $K_{\mu 2}$ trigger mask had a relative downscale factor $D = 150$.

Events were selected requiring exactly one good track reconstructed in the spectrometer consistent with an upstream kaon decay and with the decay vertex inside the fiducial volume; no LKr clusters in time with the track were allowed, apart from those directly associated to leptons via energy deposit or bremsstrahlung. Additional geometric cuts were used to suppress the halo background extrapolating the tracks to the final collimator plane and selecting the appropriate region. Lepton identification relied on the measurement of E/p, namely the ratio between the energy deposit in the LKr for a track and the momentum of the track itself measured by the DCHs: positrons were selected asking for $0.9 < E/p < 1.1$, while tracks with $E/p < 0.85$ were identified as muons. Finally, K_{l2} events were collected around the peaks of the squared missing mass distributions $m_l^2 = (P_K - P_l)^2$ using the average beam momentum for the upstream particles, evaluated through $K_{3\pi}$ samples. Figure 1.7 shows the squared missing mass distribution for events passing the K_{l2} selections in the two different lepton mass hypotheses.

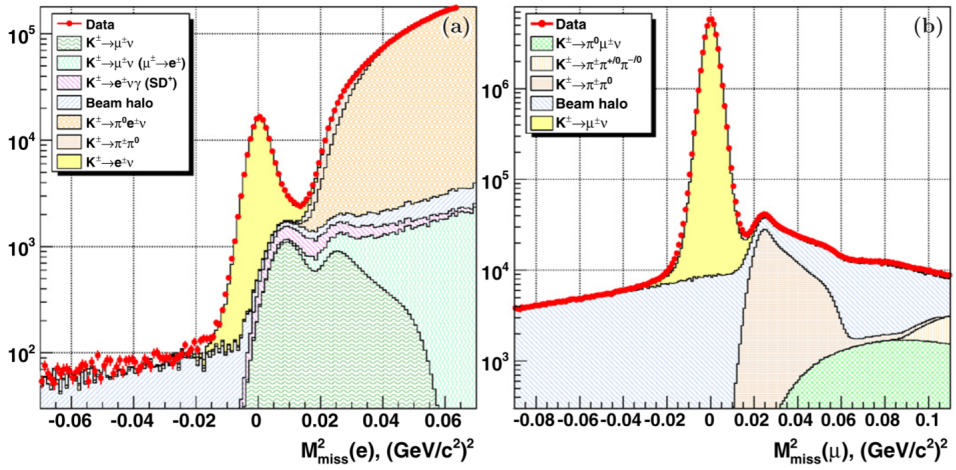

Figure 1.7: Squared missing mass distributions in the electron (left) and muon (right) mass hypothesis for events passing the full selection. Figure from [27].

Since no upstream tracking system was present, muons coming from beam halo contributed as a background for the measurement; they have been taken into account selecting K^+ and K^- blocking the negative and positive component of the beam, respectively. Another important source of background come from "catastrophic bremsstrahlung", namely the possibility of muons to deposit large amount of their energy in the calorimeter, mimicking a K_{e2} events. This background contribution have been evaluated selecting a pure $K_{\mu 2}$ sample placing a 9.2 X_0 deep lead bar upstream the calorimeter. R_K, then, has been evaluated analyzing the four different data samples: $K^+(Pb)$, $K^+(noPb)$, $K^-(Pb)$ and $K^-(noPb)$. For each subset, 10 measurements were performed in bins of track momentum, from 13 to 65 GeV/c, for a total of 40 indipendent measurements. The value of R_K in each bin is given by

$$R_K = \frac{1}{D} \cdot \frac{N_{K_{e2}} - N^{bg}_{K_{e2}}}{N_{K_{\mu 2}} - N^{bg}_{K_{\mu 2}}} \cdot \frac{A_{Ke2}}{A_{K\mu 2}} \cdot \frac{f_\mu \epsilon^{K_{\mu 2}}_{trigg}}{f_e \epsilon^{K_{e2}}_{trigg}} \cdot \frac{1}{f_{LKr}} \tag{1.21}$$

where $N_{K_{e2}}$ and $N_{K_{\mu 2}}$ are the number of signal candidates, $N^{bg}_{K_{e2}}$ and $N^{bg}_{K_{\mu 2}}$ the number of expected background events, A_{Ke2} and $A_{K\mu 2}$ the geometric acceptances, $\epsilon^{K_{l2}}_{trigg}$ the efficiencies of the trigger streams, f_l are the particle identification efficiencies for the two leptons and f_{LKr} is the global LKr

readout efficiency, which affects K_{e2} mode only.

As mentioned before, background events from muon were studied selecting control samples with one of the two charged beams blocked by the dump; a MC simulation used the properties of the halo (spatial, angular and momentum distributions) as inputs in order to estimate the background contribution to K_{e2} events. The results of this simulation were in good agreement with the direct measurement of this background source, obtained from the negative tail of the squared missing mass in the muon mass hypothesis. Uncertainties on the background came from the limited control samples size, normalization due to kaon and pion decays upstream the fiducial volume and from the time dependence of the geometric efficiencies, because of variations in the beam geometry.

Apart from muon halo, $K_{\mu 2}$ events had very low background. K_{e2} region, on the other hand, showed several background contribution to be taken into account. One important source, already mentioned, are $K_{\mu 2}$ decays with "catastrophic bremsstrahlung" before the LKr. Muon misidentification probability was measured on data by tracks from $K_{\mu 2}$ events crossing the Pb bar in front of the calorimeter in the $K^{\pm}(Pb)$ samples, in an almost background free configuration (the contribution for positron crossing the bar and producing a LKr cluster was $O(10^{-5})$). From the measured misidentification probability, the contribution due to the traverse of the bar was removed, evaluating the latter by a MC simulation. The uncertainty on the background came from the limited sample size with the bar installed.

Another source of background was represented by $K^{\pm} \to e^{\pm}\nu\gamma$ decays: kaon radiative decay can occurr via inner bremsstrahlung (IB) or direct emission (DE) processes (Figure 1.8). The latter depends on the hadron structure, therefore it is tipically denoted as structure dependent (SD); depending on the polarization of the emitted photons, two contributions can be distiguished, labelled as SD^{+} and SD^{-}. R_K definition includes IB radiative decay but neglects the $SD^{\pm}$ contributions, which have to be properly subtracted from the K_{e2} samples. The $SD^{\pm}$ component was evaluated by a MC simulation, with the uncertainty on the background estimation mainly due to the limited experimental precision on the BR.

Also hadronic and semileptonic decays, such as $K^{\pm} \to \pi^{\pm}\pi^{0}$ or $K^{\pm} \to \pi^{0}e^{\pm}\nu$, could contribute to K_{e2} background if the π^{0} was not reconstructed, and $\pi^{\pm}$ were misidentified as $e^{\pm}$ for the second mode, or if the only reconstructed particle was one lepton from the Dalitz decay of the neutral pion, $\pi^{0} \to e^{+}e^{-}\gamma$. These decay modes could enter into the K_{e2} region only if

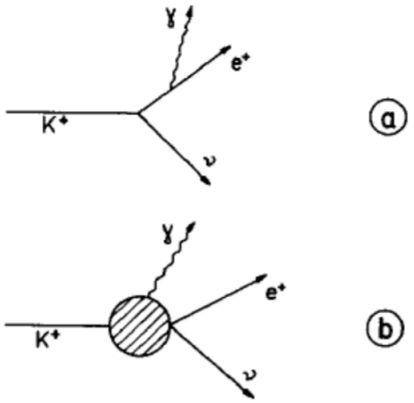

Figure 1.8: Feynman diagrams for $K^{\pm} \to e^{\pm}\nu\gamma$ decays: (a) Inner Bremsstrahlung; (b) Structure Dependent.

they came from high momentum kaons or because of multiple scattering in the spectrometer. The systematic uncertainty on this background came from limited precision of the non Gaussian tails of the multiple scattering.

Other sources of systematic uncertainties came from acceptance corrections to take into account the not hermetic decay region, which allowed bremsstrahlung photons to be undetected. The evaluation of this correction required an accurate description of the material before the DCHs, translating into a systematic uncertainty of $\delta R_K = 0.002 \times 10^{-5}$. Table **??** summarizes all the contribution to the systematic uncertainty.

The result obtained by NA62 with a total of ~ 150000 K_{e2} candidates is

$$R_K = (2.488 \pm 0.007_{stat} \pm 0.007_{syst}) \times 10^{-5} \tag{1.22}$$

and it is still the most precise measurement of this observable. The measurements obtained in each bin of momentum and in each sample are reported in Figure 1.9.

1.3.1 KLOE measurement

A O(‰) measurement of R_K has been performed also by KLOE collaboration in 2009. This measure dedicated particular attention to the study of the $K_{e2\gamma}$ decay, with a different technique compared to NA62-RK. The approach

Source	$\delta R_K \times 10^5$
$K_{\mu 2}$ background	0.004
$K^{\pm} \to e^{\pm}\nu\gamma$ (SD$^+$) background	0.002
$K^{\pm} \to \pi^{\pm}\pi^0$, $K^{\pm} \to \pi^0 e^{\pm}\nu$ backgrounds	0.003
Muon halo background	0.002
Spectrometer material composition	0.002
Acceptance correction	0.002
Spectrometer alignment	0.001
Electron identification inefficiency	0.001
1-track trigger inefficiency	0.001
LKr readout inefficiency	0.001

Table 1.2: Contributions to systematic uncertainty for R_K measurement by NA62 experiment in 2013. Table from [27].

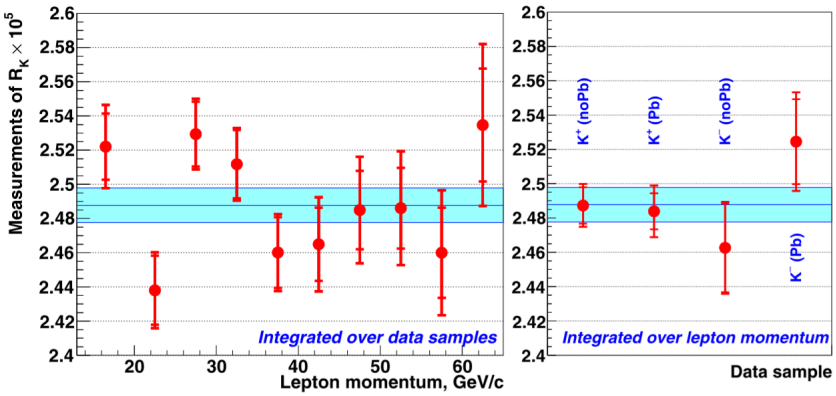

Figure 1.9: Measurement of R_K by NA62 experiment in 2013 in bins of momentum (left) and for the different samples collected (right). Figure from [27].

followed by KLOE [29] was measuring the ratio

$$R_{10} = \frac{\Gamma(K_{e2\gamma}),\ E_\gamma < 10\ \text{MeV}}{\Gamma(K_{\mu 2})} \tag{1.23}$$

for which χPT up to $O(e^2p^4)$ predicts the following relationship with R_K:

$$R_{10} = R_K \times (0.9357 \pm 0.0007) \tag{1.24}$$

The contribution due to direct emission in this range is negligible; in addition, KLOE collaboration studied $K_{e2\gamma}$ decay measuring the integral of the differential decay width

$$\frac{dR_\gamma}{dE_\gamma} = \frac{1}{\Gamma(K_{\mu 2})}\frac{d\Gamma(K_{e2\gamma)}}{dE_\gamma} \tag{1.25}$$

for $E_\gamma > 10$ MeV.

KLOE detector analyzed data from ϕ decays produced by DAϕNE facility, a e^+e^- collider with $\sqrt{s} = m_\pi \sim 1.02$ GeV; ϕ meson decayed in a K^+K^- pair with a BR of $\sim 49\%$. KLOE apparatus was made by a drift chamber (DC) and an electromagnetic calorimeter (EMC). DC was a cylinder with a diameter of 4 m and a length of 3.3 m: the detector contained 12582 sense wires - made by tungsten - and 37746 aluminium field wires, placed almost uniformly in the sensitive volume. The gas mixture contained 90 % hydrogen and 10 % isobutane to minimize multiple scattering and a magnetic fiel of 0.52 T was used to measure particle momenta. DC had spacial resolutions $\sigma_{xy} = 150$ μm and $\sigma_z = 2$ mm, while the momentum resolution at large polar angle was $\sigma(p_\perp/p_\perp) \leq 0.4\%$. EMC was a sampling calorimeter made by lead and scintillating fibers, covering 98% of the solid angle. The material lenght was $X_0 \sim 1.5$ cm and five layers are used to ensure electromagnetic shower collection. The energy and time resolutions for EMC are $\sigma_E/E \sim 5.7\%/\sqrt{E(\text{GeV})}$ and $\sigma_t = 54\ \text{ps}/\sqrt{\text{E(GeV)}} \oplus 140$ ps respectively. A scheme of the KLOE apparatus is shown in Figure 1.10.

Kaon from ϕ decays were selected by the observation of two tracks: the first one, associated to the kaon, had to be produced at the beams interaction point with a momentum in the range $[70-130]$ MeV/c while the second track origin had to be equal to the end point of the kaon track. From the track momenta, P_K and P_l as they refer to the kaon and the lepton respectively, the squared missing mass was computed:

$$m_l^2 = (E_K - |P_K - P_l|)^2 - P_l^2 \tag{1.26}$$

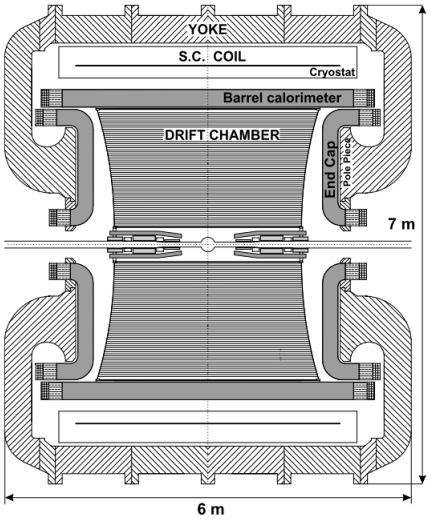

Figure 1.10: Vertical section of the KLOE detector. Figure from [30].

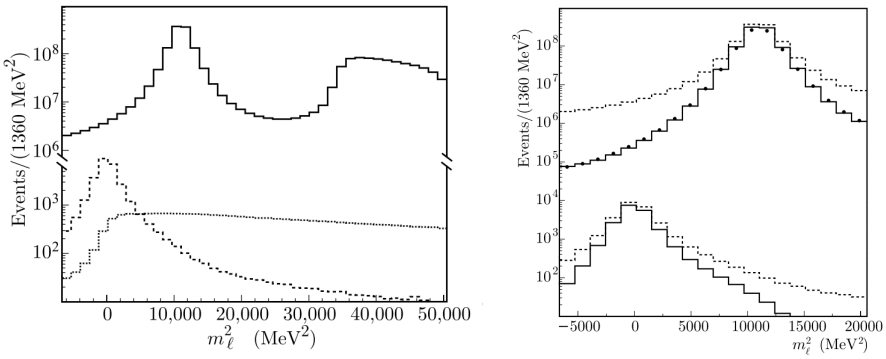

Figure 1.11: Left: m_l^2 distribution obtained for MC simulation. The contributions due to $K_{e2\gamma}$ with $E < 10$ MeV ($E > 10$ MeV) is shown by dotted (dashed) lines. Right: m_l^2 distributions for K_{e2} and $K_{\mu 2}$ samples; dashed lines show the distribution for the same variables before the quality cuts. Figures from [29].

Figure 1.11 shows the missing mass distribution obtained by MC simulations: despite the $K_{\mu 2}$ peak is well visible, great efforts in terms of background rejection were necessary in order to select K_{e2} sample. Quality cuts on both DC and EMC were applied to remove background from badly reconstructed tracks and events with pion or muons in the final state: in particular, a big contribution to the overall background rejection was due to a neural network built on the calorimeter information, namely shower profile and energy deposition. The number of K_{l2} candidates was obtained using a binned maximum likelyhood fit to the 2D NN - the neural network output - vs m_l^2 plane, with the signal shape distributions taken from MC. $K_{e2\gamma}$ sample was collected using a selection similar to that used for K_{e2} with with tighter cuts in terms of PID. Additional background rejection was achieved estimating the energy of the photon in the laboratory frame from the photon direction and from the kaon and lepton momenta, with a resolution of ~ 12 MeV. The number of $K_{e2\gamma}$ candidates was given by a binned maximum likelyhood fit in the $\Delta E_\gamma/\sigma$, m_l^2 plane, with $\Delta E_\gamma = E_{\gamma(lab)} - E_{\gamma,EMC}$.

The total number of K_{e2} and $K_{\mu 2}$ events collected were $12412 \pm 129 \pm 45$ and 5.620×10^8 respectively. Table 1.3 summarizes the uncertainties for both R_{10} and R_γ measurements.

Results by KLOE are, then [29]:

$$R_{K_{KLOE}} = (2.493 \pm 0.025_{stat} \pm 0.019_{syst}) \times 10^{-5} \tag{1.27}$$

$$R_\gamma = (1.483 \pm 0.066_{stat} \pm 0.013_{syst}) \times 10^{-5} \tag{1.28}$$

Both measurements are in agreement with the SM expectations.

	$\delta_{R_{10}}$ $(\times 10^5)$	δ_{R_γ} $(\times 10^5)$
Statistical	0.024	0.066
Counting:		
fit	0.007	0.004
DE	0.005	-
Efficiency:		
kinematics	0.014	0.009
trigger	0.009	0.006
e, μ cluster	0.005	0.003
γ cluster	-	0.003
Total systematic error	0.019	0.013

Table 1.3: Error contributions to R_{10} and R_γ measurements by KLOE. Table from [29].

Chapter 2

The NA62 experiment at CERN

NA62 is a fixed target experiment located in the CERN North Area (NA). It has been designed for high intensity and high precision kaon physics, with the main goal of measuring the branching ratio of the very rare decay $K^+ \to \pi^+\nu\bar{\nu}$ at 10% precision. After a commissioning phase, the experiment took data from 2016 until Long Shutdown 2 (LS2) in 2018 and new data taking is scheduled after LS2 from 2021. In this chapter, the main characteristics of the NA62 experiment are described.

2.1 Physics motivations

$K^+ \to \pi^+\nu\bar{\nu}$ decay is a Flavour Changing Neutral Current (FCNC) process, forbidden at tree level in the SM by the GIM mechanism and therefore described by higher order Feynman diagrams, such as those reported in Figure 2.1. For each quark involved in the loops, the contribution to the amplitude of the $s \to d\nu\bar{\nu}$ transition is proportional to:

$$A_q \propto \frac{m_q^2}{M_W^2} V_{qd} V_{qs}^* \qquad q = u, c, t \tag{2.1}$$

From the latter is clear that the process is dominated by top quark loops: the corresponding CKM matrix elements entering in the amplitudes are $V_{td}V_{ts}^*$, which make the decay very suppressed. The theoretical prediction for $BR(K^+ \to \pi^+\nu\bar{\nu})$ is very precise since the hadronic matrix element

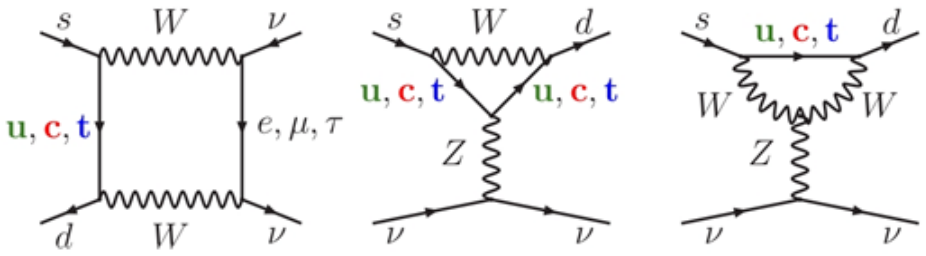

Figure 2.1: Lowest order Feynman diagrams in the SM for $K^+ \to \pi^+\nu\bar{\nu}$ decay.

can be related, via isospin symmetry, to the one of the semileptonic decay $K^+ \to \pi^0 e^+ \nu$, experimentally well known; the most recent estimate is [31]:

$$BR(K^+ \to \pi^+\nu\bar{\nu}) = (8.4 \pm 1.0) \times 10^{-11} \tag{2.2}$$

$K^+ \to \pi^+\nu\bar{\nu}$ decay can be significantly different from the SM expectation because of new physics effects: several models can affect both $K \to \pi\nu\bar{\nu}$ modes, with different correlation between the two observables. The most precise experimental result so far has been obtained by the E949 experiment at Brookhaven [32]:

$$BR(K^+ \to \pi^+\nu\bar{\nu}) = 1.75^{+1.15}_{-1.05} \times 10^{-10} \tag{2.3}$$

A more precise measurement, then, is mandatory to probe the existence of new physics.

One of the keystone of $K^+ \to \pi^+\nu\bar{\nu}$ analysis is the background suppression, in particular from $K^+ \to \pi^+\pi^0$ because of its large Branching Ratio. To succesfully reject events with photons in the final state, strict veto conditions are used in the analysis, with the result of having a certain probability to discard events only because of random activity in the detectors ("random veto"). A study on the optimization of random veto and π^0 rejection is reported in Appendix A.

2.2 Main aspects of NA62 apparatus

Given its goal, the NA62 apparatus has been designed in order to fulfill the following characteristics:

- high intensity K^+ beam, with 1% momentum spread and high momentum to have decays in flight;
- high resolution tracking system for kaons and downstream tracks;
- O(100 ps) time coincidences between the detectors;
- particle identification detectors for the upstream and downstream tracks;
- higly efficient veto system, especially for photons and muons.

Each item is discussed in the following sections, while a complete and exhaustive description of the apparatus can be found in [33]

2.3 Beam line

NA62 uses a 75 GeV/c beam, produced by the interactions between 400 GeV/c proton beam from CERN SPS accelerator and a beryllium target. Using a high energy proton beam the accidental non-kaon background is suppressed, altough the discrimination among kaons, pions and protons requires more effort.

The beam is extracted from the SPS accelerator via the P42 beam line and directed to T10, a 400 mm long, 2 mm wide beryllium target. A secon beamline, K12, connects T10 with the decay region, selecting particles with a momentum of +75 GeV/c and maximizing the kaon component within the beam. The total length of K12 is 101.3 m.

Downstream T10 a 950 mm long copper collimator is located, which offers a set of bores to select the transversal size of the beam; typical chosen value is 15 mm. A set of three quadrupoles (Q1, Q2, Q3) which have a large angular acceptance ($\pm$2.7 mrad horizontally and $\pm$1.5 mrad vertically), followed by an achromat (A1), selects particle with a central momentum of 75 GeV/c and 1% rms.

The achromat is made by four dipole magnets deflecting the beam along the vertical axis: the first two magnets apply a displacement of the beam

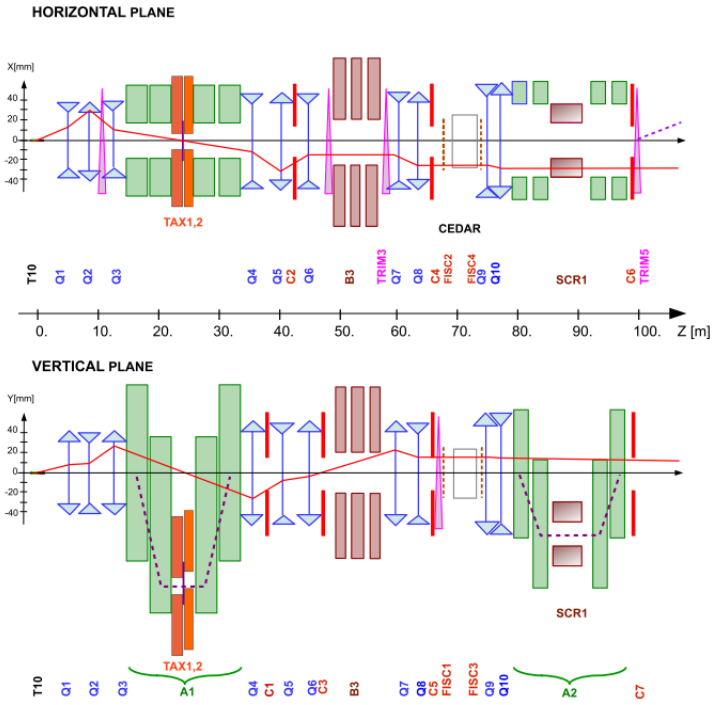

Figure 2.2: Schematic layout of K12 beamline. Figure from [33].

by 110 mm, while the other two take it on the originary direction. Within the achromat, the beam goes across graduated holes in two motorized units, TAX1 and TAX2: depending on the hole sizes, the beam intensity can be adjusted; on the other hand, closing the TAXes a data taking in dump mode can be performed.

A "radiator", made by tungsten plates with different thickness up to 5 mm, is placed between TAX 1 and TAX 2: its role is to make positron lose enough energy by bremsstrahlung in order to be rejected, minimizing the hadron losses due to scattering. The beam is then refocused along the vertical axis by three quadrupoles (Q4, Q5, Q6) and two collimators (C1, C2). A subsequent collimator (C3) can absorb positron which have been degraded in momentum by the radiator.

C3 is followed by a 40 mm diameter bore, made by iron plates, located between the poles of a 2 m long dipole (B3), whose vertical field around the beam sweep aside muons of both signs. K^+ in the beam are identified by a Cherenkov differential counter (CEDAR); to be effective, it requires that the beam is parallel to the z axis and this is ensured via two quadrupoles (Q7 and Q8). Two additional collimators (C4, C5) absorb the particles in the tails of the beam.

Beam parameters, i.e. its mean and standard deviation, are measured by two pairs of filament scintillating counters, FISC1,3 and FISC2,4, installed upstream and downstream of the CEDAR respectively: the mean beam divergence can be measured and tuned to zero while the remaining intrinsic divergence can be monitored in both planes.

After the CEDAR, the beam is focused by two quadrupoles (Q9, Q10) into the tracking system (GiGaTracker, GTK). GTK is made by three station of silicon pixel detectors operating in vacuum. The stations are disposed in such a way that between GTK1 and GTK3 a second achromat (A2) is placed, made by four C-shaped dipole magnets. A2 provides also muon defocusing via the return yokes of the third and the fourth magnets and by an iron-magnetized collimator (SCR1). The beam displacement due to A2 is $\Delta Y = -60$ mm.

The GTK3 position, 102.4 m from the target, defines the beginning of the decay region: before it, two collimators (C6 and C7) intercept background outside the beam acceptance. Beam particles enter into the decay region with a deflection towards the X axis by +1.2 mrad, provided by a final collimator (TRIM5). The deflection is such that the subsequent -3.6 mrad deviation towards negative X - due to downstream spectrometer magnet MNP33 - let

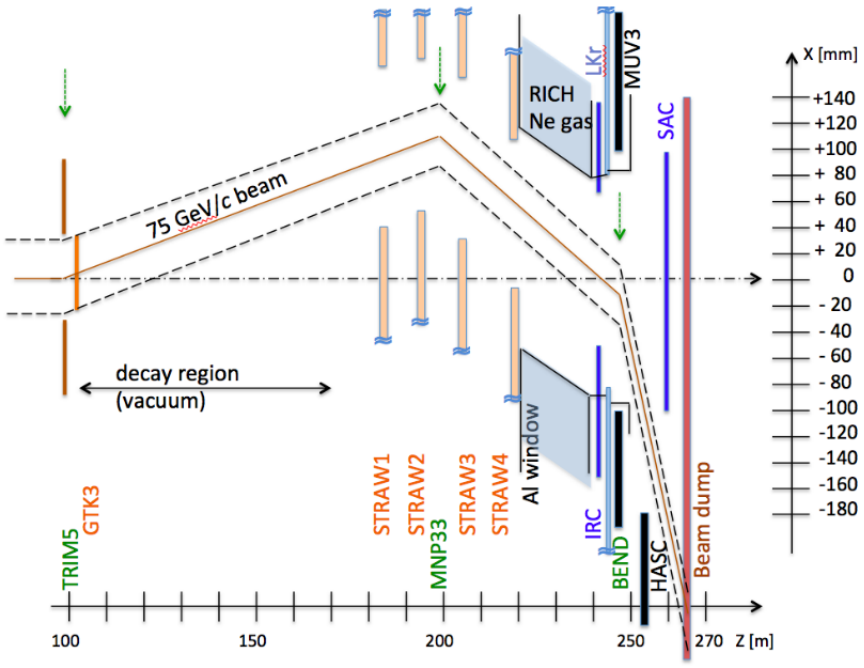

Figure 2.3: Sketch of the downstream part of the NA62 beamline (P42). Figure from [33].

the not-decayed beam particles pass through the center of LKr calorimeter and other downstream detectors, as shown in Figure 2.3.

The beam is extracted in packets ("bursts") following the SPS cycle; the duration of a burst can be 6 s or 4.8 s depending on the SPS operational conditions. The beam intensity can be evaluated by the number of protons on T10 (POT) in a burst: in 2017 the beam intensity was around 20×10^{11} POT, 60% of the design value.

2.4 KTAG

Kaons produced at T10 are only 6% of the secondary beam, therefore a K^+ identification is the first requirement in every physics analysis at NA62.

The identification is provided by a ChErenkov Differential counters with Achromatic Ring (CEDAR), designed at CERN in 1970s to provide $p/\pi/K$ separation in beams extracted from SPS. The CEDAR detector used by NA62

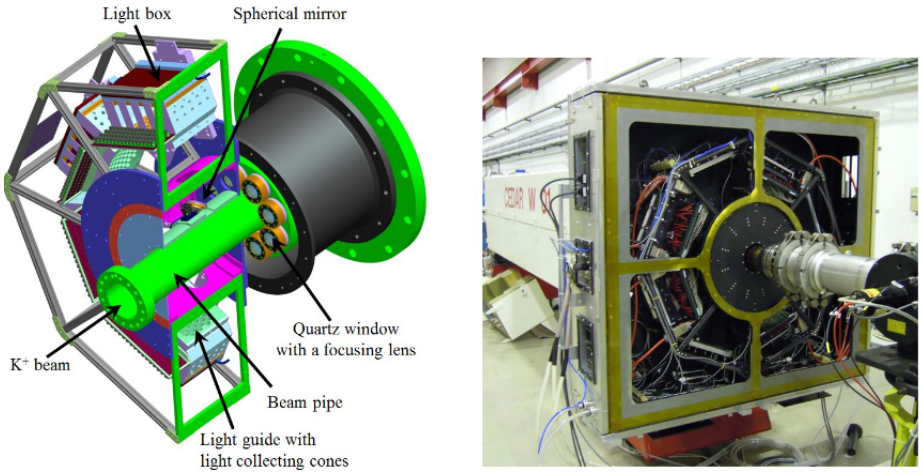

Figure 2.4: Left: scheme of the KTAG; right: Cedar vessel with the KTAG installed on it. Figures from [33].

consist of a 0.93 m^3 radiator vessel filled with gas and a diaphragm of fixed central radius and adjustable annular aperture: the beam particles produce Cherenkov light passing through the radiator and the desired particles can be selected adjusting the gas pressure in order to let their Cherenkov light cone pass through the diaphragm.

NA62 CEDAR typically operates with nitrogen at 1.75 bar, corresponding to $3.5 \times 10^{-2} X_0$ of material that the beam has to go through; alternatively, the radiator can be filled with hydrogen at 3.9 bar, for a total material length of $7 \times 10^{-3} X_0$.

Although the CEDAR vessel and optics were suitable for NA62, new readout system including photomultipliers (Kaon Tagger, **KTAG)** has been built in order to handle 45 MHz of kaons and have a time resolution of O(100 ps). Cherenkov light emitted by kaons passes through the annular diaphragm and exits from eight quartz windows. At the exit of the window, a spherical mirror reflects the light radially into a light box, equipped with a matrix of 64 light cones of 15 mm outer and 4 mm inner radius, each hosting 48 Hamamatsu photomultipliers. The time coincidence between an high number of sectors of the detector ensures the presence of a K^+. A scheme showing KTAG components and its installation next to Cedar vessel is reported in Figure 2.4. KTAG performances have been measured in 2015 and the following results have been achieved:

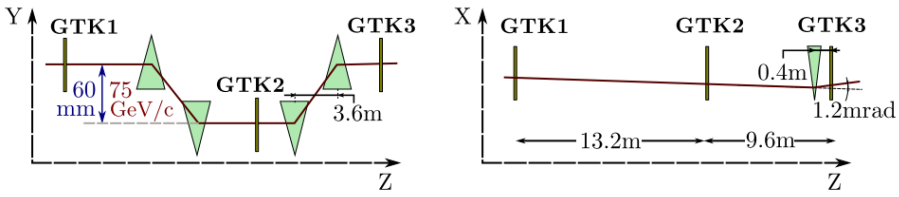

Figure 2.5: Sketch of the three GigaTracker station placement with respect to the ideal trajectory of a beam particle. Figure from [33].

- $\sigma_t = 70$ ps ;
- $\epsilon_K = 98\%$ with $N_c > 5$;
- π mis-identification $O(10^{-4})$.

2.5 GigaTracKer (GTK)

The GTK measures beam particles momentum and their directions with an excellent time resolution. The detector is made by three identical stations operating in vacuum; the second station is placed inside an achromat that deflects the beam by 60 mm in y axis, as can be seen in Figure 2.5. The spectrometer is able to measure beam momentum with a resolution of 0.2% and track slopes to 16 μrad. The requirements for the detector in terms of resolution, rate sustainability and radiation hardness took significant design efforts, making the GTK the state of the art for pixel trackers in high rate environments. Radiation damages, however, are not negligibe since they create defects reducing signal yields and worsening the time resolution. A combination of cooling, increasing bias voltages and chip replacements mitigates the effects of radiation, allowing the detector to work in its optimal conditions.

Each station contains an hybrid silicon sensitive volume of 18000 pixels, with a size of 300×300 μm^2 and a thickness of 200 μm, corresponding to less than $0.5\%X_0$. Pixels are arranged in an area of 62.8×27 mm^2, which covers to the transverse section of the secondary beam.

GTK stations are cooled at $-15°$ C using a challenging technique ("microchannel cooling"): a cooling fluid (C_6F_{14}) flows through 150 parallel channels, etched on a 140 μm thick silicon plate. The cooling plate is glued on the back side of the readout chip, which is connected to the sensor (Figure 2.6).

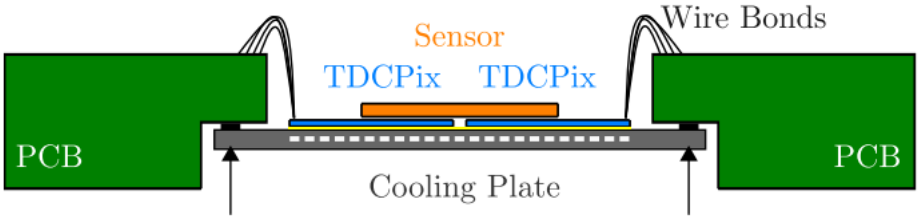

Figure 2.6: GTK cooling system. Figure from [33].

2.6 CHANTI

Despite the modest thickness, probability of interactions between beam particles and GTK stations is not negligible; the most dangerous category among these interactions are inelastic scatterings where pions of several GeVs are produced. If one of the pions reaches the decay region, it would mimic the signature of a $K^+ \to \pi^+ \nu\bar{\nu}$ decay.

Particles produced by interactions occurring in GTK1 and GTK2 are mostly swept away by the magnets in K12 beamline, while no deflections is available for interactions in GTK3; these events are rejected by a specific detector: the CHarged ANTIcounter (**CHANTI**).

CHANTI is made by six stations of plastic scintillators, put in the same vacuum vessel of GTK3, with an area of 300×300 mm^2;in the central part of the stations an aperture of 95×65 mm^2 allows the passage of the beam. The distance between stations follows a geometric progression, in order to cover an angular region between 1.34 rad and 49 mrad; hermeticity for inelastic interactions rejection at smaller angles is ensured by downstream detectors. Due to the small distance between the detector and the beam, the main contribution to CHANTI rate comes from muon halo, produced by kaon and pion decays along the beam line.

Each station contains 48 bars of plastic scintillators with different lengths oriented to form X and Y planes; a triangular cross section is used for the bars, so that a particle has to cross tipically two bars in each plane.

At the center of the bars a fast Wavelength Shifting (WLS) fiber collects the scintillation light and emits photons that are read by Silicon PhotoMultipliers (SiPM). SiPM gain is kept constant monitoring the temperature and consequently adjusting the bias voltage.

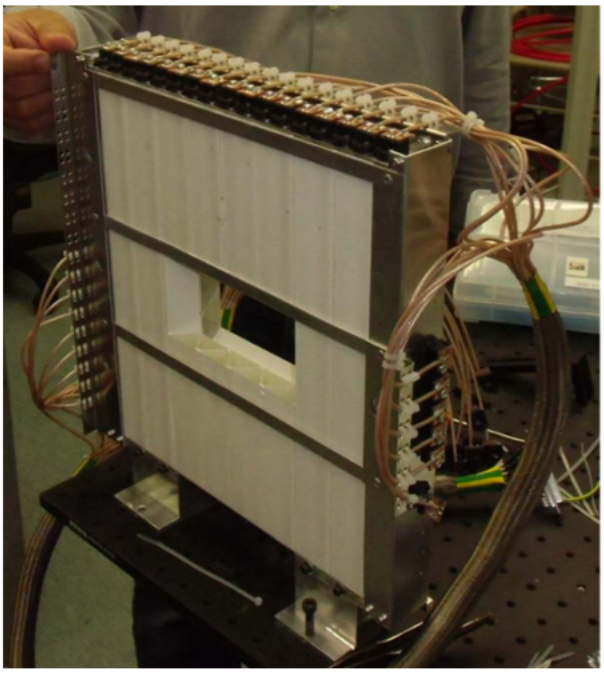

Figure 2.7: One of the six CHANTI stations, fully equipped and ready to be installed in vacuum vessel. SiPM are well visible in the top side of the station. Figure from [33].

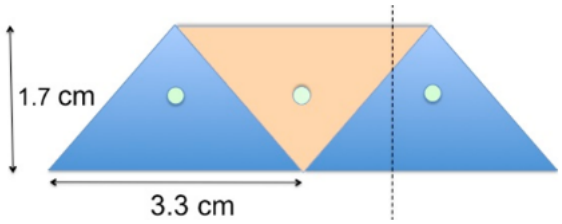

Figure 2.8: Arrangement of the CHANTI scintillating bars; the direction of the beam is represented by the dashed line. Figure from [33].

CHANTI performances has been mesured using dedicated muon runs in 2015. The efficiencies of all the views of all the stations are found to be constant and above 99%, while the spatial and time resolution are about 2.5 mm and 800 ps respectively. More details on CHANTI design and performances can be found in [34].

2.7 Large Angle Veto

The decay region starts immediately after CHANTI, for a total of 75 m. The high momentum of the beam provides a boost to the decay products, however the challenging goal of NA62 requires a reliable photon detection capability at higher angles, up to 50 mrad. Photons emitted at angles between 50 mrad and 8.5 mrad are detected by the 12 stations of the Large Angle Veto system (LAV). Results from a simulation of $K^{\rightarrow}\pi^{+}\pi^{0}$ decays showed that only 0.2% of the events with one photon emitted at an angle higher than 50 mrad, while no events can be generated with both photons above 50 mrad. Anticorrelation between emission angle and photon energy requires that LAV has to be higly efficient to low energy photons; in particular, the design inefficiency was 10^{-4} for photons with energies greater than 200 MeV.

LAV stations uses lead glass scintillators coming from the OPAL calorimeter, tested in 2007 to ensure that their performances were suitable for NA62. The material contains 75% of PbO by weight, has a radiation length $X_0 =$ 1.50 cm and a refraction index $n = 1.85$ cm at $\lambda = 550$ nm. Lead glass blocks are 37 cm long with front and rear faces of 10×10 and 11×11 cm^2 respectively; the rear face of each blocks is connected to a 76 mm photomultiplier via a 4 cm long light guide. Photons are detected collecting the Cherenkov light produced by the charged particles of the electromagnetic shower.

The blocks are arranged in rings of different radii surrounding the decay tube. Each station contains more than one ring (or layer) in order to have high detection efficiency and the layers are staggered with respect to each other to ensure the absence of blind spots. As a result, particles impinging on LAVs at any angle traverses at least three blocks, for a total of at least 21 X_0. The first 11 stations are in vacuum while LAV 12 operates in air, with several changes in the design in order to cope with the different operating situation. Geometrical parameters of LAV stations are described in Table 2.1.

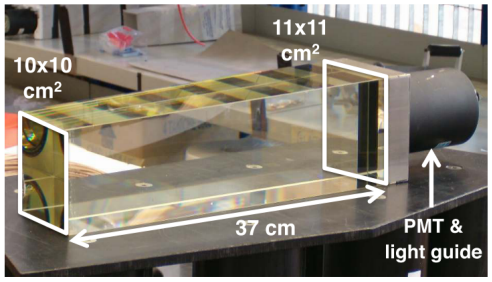

Figure 2.9: Left: one of the lead-glass blocks used for the Large Angle Veto (LAV). Right: a LAV station fully assembled. Figure from [33].

Station ID	Inner radius [mm]	Outer radius [mm]	Number of blocks
1-5	537	907	160
6-8	767	1137	240
9-11	980	1350	240
12	1070	1440	256

Table 2.1: Parameters of Large Angle Veto system

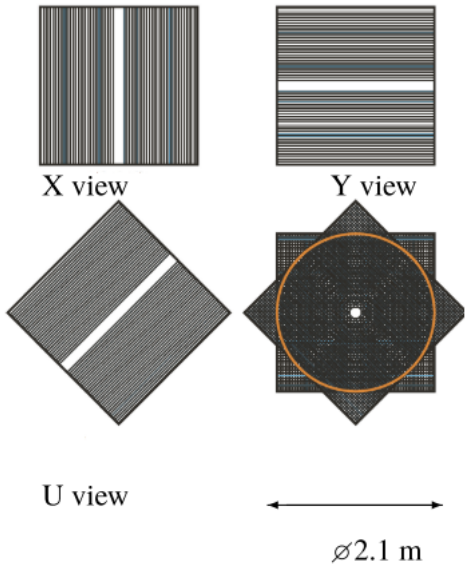

Figure 2.10: Scheme of a STRAW chamber. Figure from [33].

2.8 Downstream spectrometer

Momenta of downstream particles are measured by a straw chambers spectrometer, placed at the end of the decay region. It consists of four chambers and a large aperture dipole magnet (MNP33) which provides a integrated magnetic field of 0.9 Tm. The design choice is guided by minimize multiple scattering: light materials were used and the detector is installed in vacuum tanks; the total amount of material of the whole detector is 1.8% X_0. Each station is made by two planes of straw tubes, rotated by 45° as shown in Figure 2.10. A complete station, then, measures X and Y position by one plane and U and V coordinates by the other plane, ensuring redundancy which reduces the reconstruction of ghost tracks.

Each STRAW station contains 1792 straws of 9.82 mm diameter and 2160 mm length. The central region of each plane contains a gap of 12 cm without straw tubes, so that an octagon of 6 cm apothem is created in the fully equipped station to let the beam pass; the outer diameter of the active area is 2.1 m. The gas used in the straw tubes is a mixture of 70% Ar and 30% CO_2 at room pressure. The tubes are flexible and spatially separated to allow the increase of their diameter when the detector is in vacuum.

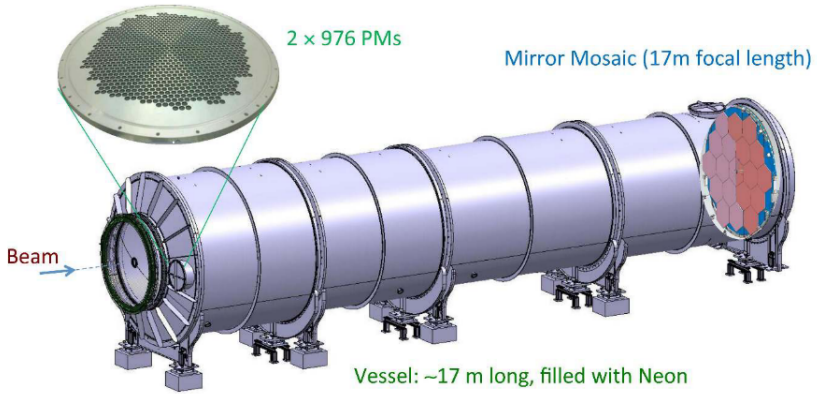

Figure 2.11: Scheme of the RICH. Figure from [33].

Spectrometer performances were evaluated in 2015: the reconstruction efficiency was found to be greater than 95 % in a momentum range [10-40] GeV/c while the momentum resolution was in agreement with the design requirement:

$$\frac{\sigma_p}{p} = 0.30\% \oplus 0.005\% \cdot p[\text{GeV/c}] \tag{2.4}$$

2.9 RICH

A reliable particle identification (PID in the following) is a necessary requirement for most of NA62 analyses; information provided by calorimeters, which will be discussed later, doesn't allow to reach the challenging performances mandatory for $K^+ \to \pi^+\nu\bar{\nu}$ branching ratio measurement and therefore a Ring Imaging CHerenkov detector (RICH) has been built.

The detector is made by a cylindrical vessel of 17.5 m length and gradually decreasing diameter, from 3.88 m to 3.25 m, filled with neon at 990 mbar. The vessel is traversed by an aluminium pipe, connected to the vacuum tank, that allows the passage of the beam. The downstream face of the vessel contains 20 mirrors, 18 hexagonal and 2 semi-hexagonal around the beam hole, made by 25 mm of glass coated with aluminium and a dielectric film to improve reflectivity. Cherenkov light is reflected by the mirrors into a ring in their focal plane, which corresponds to the front face of the detector where two arrays of 976 Photomultipliers are installed (Figure 2.11).

The support of the mirrors allows fine alignment of the detector via two

thin aluminium ribbons and a piezoelectric system; mirrors alignment has been checked periodically with data.

RICH performances, evaluated on a pion sample, showed that the detector has a time resolution of about 140 ps and an efficiency of:

$$\epsilon_\pi = 83\% \quad \epsilon_\mu = 0.2\% \quad [15 - 35] \text{ GeV/c} \tag{2.5}$$

2.10 Charged hodoscopes

Signals from charged particles produced by kaon decays are collected by two charged hodoscopes (CHODs). Since one of them was used in the previous experiment, we refer to them as NA48-CHOD and CHOD. The main reason for having a second hodoscope is the higher rate NA62 operates with, compared to the NA48 experiment.

2.10.1 NA48-CHOD

The NA48-CHOD is made by two planes of 64 scintillating slabs of 2 cm thickness. The slabs are assembled in four quadrants to form an octagon of 1210 mm apothem, with an hole in the center of 128 mm radius. Slabs widths vary from 65 mm in the central region to 99 mm at the edges of the detector. Each slab is connected at one edge to a photomultiplier, as shown in Figure 2.12-left.

The two planes provide indipendent measurements, reducing the accidental activity when used in coincidence. The NA48-CHOD is mainly used to provide a timing information at the first trigger level, as well as event time for charged particles. Its time resolution is about 210 ps with an inefficiency of O(1‰).

2.10.2 CHOD

The new hodoscope is installed on the front plane of the LAV12 station; it has 152 scintillating tiles organized in an annulus with inner and outer radii of 140 and 1070 mm respectively (Figure 2.12-rigt). The overall dimensions of the detector are those of an octagon of 1550 mm apothem. The light produced in each tile is transfered by four WLS fibers to SiPMs, mounted on mother-boards placed on the sided of the octagon. The time resolution of

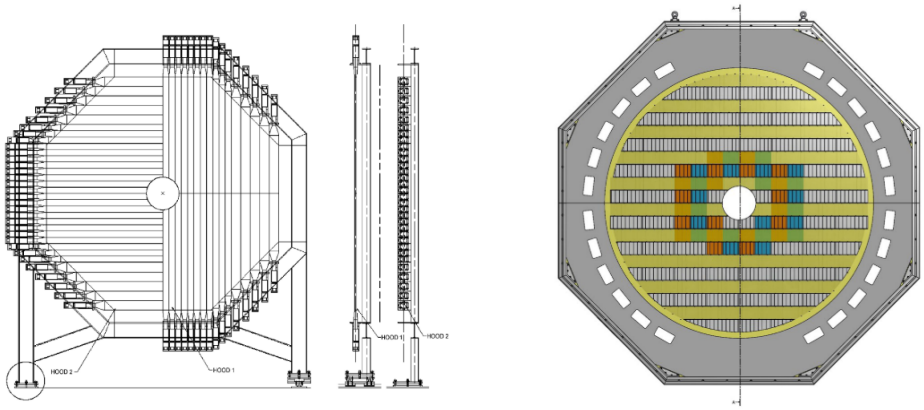

Figure 2.12: Charged hodoscopes used by NA62: the NA48-CHOD (left) and the CHOD (right). Figures from [33].

CHOD signal is about 1 ns. Tiles offers the advantages of optimizing the rate distribution in the readout channels and improving the flexibility of trigger configuration, allowing the use of a group of cells for specific trigger purposes. Expected rates and probability to have a signal produced by a $K^+ \to \pi^+\nu\bar{\nu}$ in each tile has been evaluated via MonteCarlo simulation, suggesting the group of channels that can be masked at trigger level because of low signal acceptance.

2.11 Liquid Krypton calorimeter (LKr)

The Liquid Krypton electromagnetic calorimeter (LKr) is the central piece of the NA62 photon veto system. It is a quasi-homogeneous calorimeter, already used in the NA48 experiment, filled with 9000 litres of liquid krypton at 120 K. The inner and outer radii are 8 and 128 cm respectively, while its depth is 127 cm (27 X_0).The active area of the calorimeter is divided into 13248 longitudinal cells, with a section of 2×2 cm^2. A beam pipe passes through the detector to allow the passage of not-decayed particles. Each cells is made by three Cu-Be electrodes, two anodes and a central cathode; to avoid inefficiencies when a particle is close to the anode, the longitudinal development of the cell follows a zig-zag shape, as showed in Figure 2.13. Six plates ("spacers") sustain the electrodes inside the detector. The former readout electronics for the LKr was decommissioned and new boards were

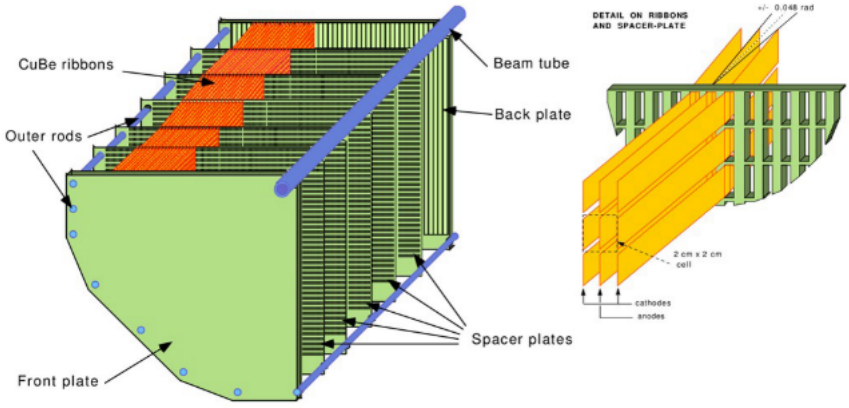

Figure 2.13: Scheme of LKr. Figure from [33].

developed to sustain an higher rate environment, which will be discussed in the following. The most significant change in the detector operation involves the cells readout, with the introduction of a Zero-Suppression (ZS) algorithm to reject noise counts: each cell is sampled into eight 25 ns windows and the energy deposits are read by flash ADCs and only cells with at least one sample above a certain threshold (corresponding to the pedestal) are read. The implementation of the ZS algorithm has the disadvantage of making the calorimeter response non linear, then additional corrections are required offline to compensate the effect.

LKr performances, despite the degradation due to aging with respect to those obtained by NA48 [28], are still good:

$$\frac{\sigma_E}{E} = \frac{4.8\%}{\sqrt{E(\text{ GeV})}} \oplus \frac{11\%}{E(\text{ GeV})} \oplus 0.9\% \tag{2.6}$$

$$\sigma_t \sim 600 \text{ ps} \tag{2.7}$$

$$1 - \epsilon \sim 10^{-6}, \quad E > 5 \text{ GeV} \tag{2.8}$$

2.12 Small Angle Veto

Photon rejection hermeticity down to 0 rad is ensured by two detectors, the Intermediate Ring Counter (IRC) and the Small Angle Calorimeter (SAC),

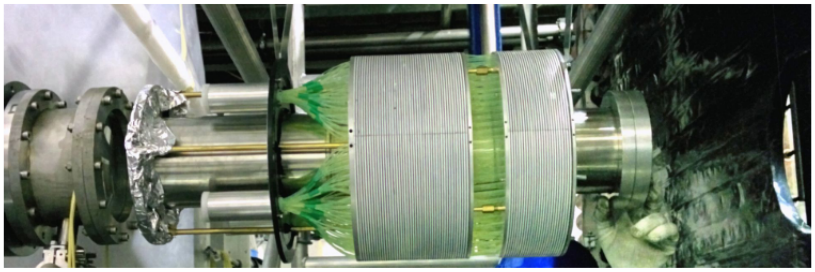

Figure 2.14: Intermediate Ring Calorimeter (IRC). Figure from [33].

tipically referred together as Small Angle Veto (SAV).

IRC (Figure 2.14) is an eccentric cylindrical calorimeter placed upstream LKr. The outer diameter is 290 mm and it is centered around Z axis, while the inner circle has a diameter of 120 mm with the center shifted by 12 mm along the positive X axis, to take into account the magnetic field provided by MNP33 to beam particles. The detector is longitudinally divided into two modules, separated by 40 mm. The depths of the upstream and downstream modules are 89 and 154 mm respectively. The modules contains a sequence of layers (25 in the upstream and 45 in the downstream module) made by 1.5 mm lead and 1.5 mm of scintillator plate, using a layout known as "shashlyk calorimeter". The modules are traversed by WLS fibers that collect scintillation light produced in the plates. The upstream face of the fibers is coated with black paper to avoid reflection and, on the downstream end, a photomultiplier produce the signal. The whole detector is covered with black paper to protect it from other ligth sources.

As well as IRC, SAC (Figure 2.15) is a shasklyk calorimeter made by 70 planes of lead and 70 planes of plastic scintillator, with tranverse dimensions of 205×205 mm^2. The detector is placed about 20 m downstream the LKr, after a dipole magnet (BEND) that finally deflects the beam along the negative X axis onto a beam dump. Light emitted by the scintillator plates is collected by WLS fibers, which are grouped into four arrays and read by four photomultipliers, located after the downstream face of the detector. Since no interal segmentation is present inside the plates, SAC operates as a single channel calorimeter.

SAV performances have been evaluated using muon runs, namely data collected closing the TAXes with MNP33 and BEND magnets switched off so that the beam contains only muons. The found inefficiency was at the

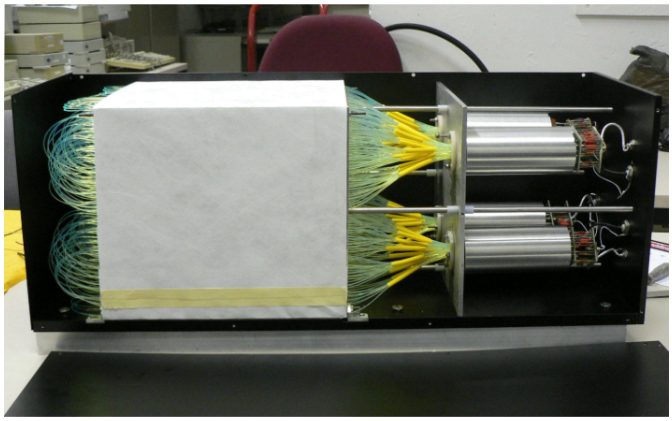

Figure 2.15: Small Angle Calorimeter (SAC). Figure from [33].

level of 7×10^{-4}, with time resolution better than 2 ns.

2.13 Muon Veto System

Muon identification and rejection is partially exploited by RICH and LKr, nevertheless a dedicated system is necessary to perform the measurement of $BR(K^+ \to \pi^+ \nu\bar{\nu})$. NA62 muon veto system is composed by an hadron calorimeter divided in two detectors (MUV1 and MUV2), an 80 cm iron wall, and a fast detector (MUV3) used at the first trigger level.

2.13.1 Hadron calorimeter

The MUV1 detector is made by 24 layers of steel plates and 23 layers of scintillator strips. The ticknesses of the steel and scintillator layers are 26.8 mm and 9 mm respectively. Strips are alternatively oriented vertically and horizontally between two consecutive scintillator layers; most of them span the whole transverse dimensions of the detector (2700×2600 mm^2) but the central ones are split in order to place the beam pipe inside the calorimeter. The strips are read by WLS fibers connected to photomultipliers. Each PM reads the signals from the similarly-aligned strips in the different planes.

MUV2 is the former NA48 hadron calorimeter: its layout is similar to MUV1, with a sandwitch of 24 couples of iron and scintillator layers. The latter contain 44 stripts in each plane and, as in MUV1, signals produced in

the scintillator are read by photomultiplier, coupled via WLS fibers. Even in this case, PMs read the information from strips corresponding to the same tranverse positions along the detector.

Pion identification with the calorimeters has been measured within the $\pi\nu\bar{\nu}$ analysis of 2016 data [35]: the π^+ selection efficiency is 78% with a muon mis-identification of 0.6×10^{-5}.

2.13.2 Fast muon veto (MUV3)

MUV3 is made by 140 tiles, with a tranverse section of 220×220 mm^2, and 8 smaller cells in the central region of the detector, where the expected rate is higher; the thickness of all the tiles is 50 mm while the total area of the detector is 2640×2640 mm^2. The front and lateral faces of the tiles are covered by a foil of aluminized Mylar, while the back face is connected to a light-tight box to avoid cross-talk between the channels. The box hosts two photomultipliers that read the signal produced by the tile.

MUV3 has a resolution of about 400 ps and a muon detection efficiency which exceeds 99.5%.

2.14 Trigger and Data AQuisition (TDAQ)

The NA62 TDAQ system is fully described in [36]. The high-intensity environment in which NA62 operates is handled by a multi-level trigger, with a first level (L0) hardware trigger and a second one (L1) software. The rate of decays is about 10 MHz, which is reduced to 1 MHz by L0 and further pushed down to 10 kHz by L1, in order to ensure data storage on tape. The system is sketched in Figure 2.16

Most of the detectors - all but GTK, STRAW and calorimeters - use a common TDC-based data aquisition system, whose centerpiece is the TEL62 board [37]. The TEL62 can host 4 TDC boards (TDCB), each controlled via a FPGA with up to 2 GB fast RAM, and a fifth FPGA which drives the output via an Gigabit Ethernet board. Each TDC controls 4 HPTDC with a time jitter of 100 ps allowing to measure leading and trailing time of 128 physical channels; as a consequence, the TEL62 can deal with 512 physical channels. When a signal from L0 is received by the central FPGA, data contained in a detector-dependent time window around the trigger are read by the TDCBs, merged and sent to the PC farm.

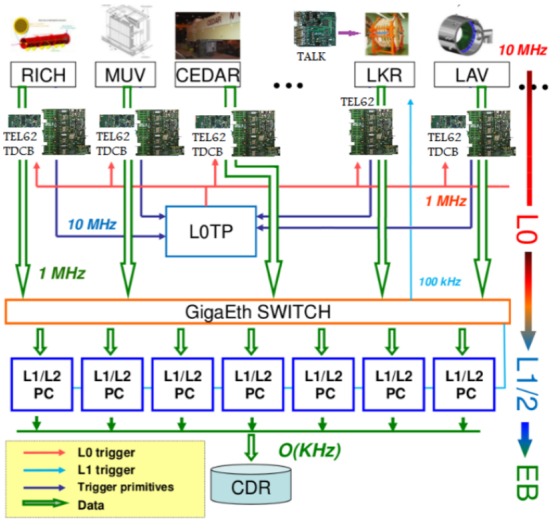

Figure 2.16: NA62 trigger and data aquisition system. Figure from [33].

GTK readout system is an interface between the on-detector readout system (TDCpix) and the clock and trigger system, centrally distributed. Each TDCpix sends the data to the corresponding board with a total bandwith of 128 Gb/s; data are organized by 6 sub-detector PCs and then sent to the central PC farm. No GTK information is needed at L0 so that data can be tranfered at the lower L1 rate.

STRAW readout boards (SRBs) contains two 8-channel front end chips, which are used to set the discriminating thresholds, and one FPGA with 32 TDCs to read leading and trailing times. Due to the intrisically lower time resolution of the detector, a less performant TDC, with a time bin of 0.78 ns, was adopted, reducing the electronics costs.

Calorimeters REAdout Modules (CREAMs) were developed for LKr and adopted also by MUV1-2 and SAV. The system is based on FADCs, which sample the signals at 40 MHz and store them in a buffer waiting for the L0 response. As for GTK, complete LKr data are only read at L1 level; however, the digital sum in a 4×4 group of cells ("supercell") is read and sent to a system of 32 TEL62 in order to produce a LKr L0 trigger primitive.

All the trigger primitives produced by the designed detectors are managed by the Level 0 Trigger Processor (L0TP), which combines them following a set of predefined configuration ("trigger masks"). If one mask is satisfied, data around the trigger time are extracted and the L1 software algorithm

analyze them.

2.15 Detector performances

In this section, some of the detector performances have been reported; the main variables used in the R_K analysis have been chosen, namely kinematic resolution and particle identification capabilities.

2.15.1 Kinematic resolution

The kinematic resolution has been evaluated in 2015 with a data sample collected with a minimum bias trigger mask. A sample of $K^+ \to \pi^+\pi^+\pi^-$ was used to calibrate STRAW spectrometer and GTK, while performances have been tested with a $K^+ \to \pi^+\pi^0$ sample. Events were selected asking for two photons in LKr, compatible with a π^0 and a single track in the final state, in time with the upstream kaon.

Given the upstream and downstream momentum, the squared missing mass in the pion mass hypothesis is defined as follows:

$$m^2_{miss} = (P_K - P_\pi)^\mu (P_K - P_\pi)_\mu \tag{2.9}$$

Figure 2.17 shows the resolution on m^2_{miss} as a function of the downstream track momentum. The resolution is compatible to an angular resolution on the upstream and downstream tracks smaller than 20 and 60 μm respectively. Full dots refer to m^2_{miss} using both GTK and STRAW spectrometers, while white boxes are obtained using the nominal beam momentum and direction. Using GTK, the resolution improves by a factor 3.

2.15.2 Particle Identification

Particle identification for R_K is based on the response of RICH and LKr.

Preliminary RICH perfomances have been evaluated in 2015: in Figure 2.18 the squared masses distributiond for e^+, μ^+ and π^+ samples producing a signal in the RICH are shown. The masses are computed using the velocity of the particles estimated by the RICH ring and their momentum measured by STRAW spectrometer. A momentum range of $[15 - 35]$ GeV/d has been used: for higher momenta, the separation between the three curves degrades quickly.

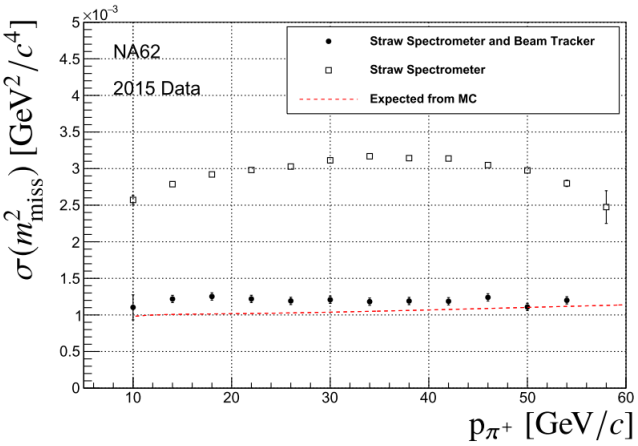

Figure 2.17: Resolution of m^2_{miss} as a function of the track momentum. Full dots refer to m^2_{miss} using both GTK and STRAW spectrometers, while white boxes are obtained using the nominal beam momentum and direction. Figure from [33].

Additional results have been obtained with 2016 data using positrons. Figure 2.19 shows a gaussian fit of the positron ring radius obtained with the RICH. The mean value is $R_{fit} = 189.6$ mm, corresponding to 11.2 mrad of Cherenkov angle; the fit result for σ_R is 1.47 mm (90 μrad). The same sample has been used to measure the ring centre resolution, as shown in Figure 2.20, where the differences between the fitted centre positions and the expected ones are plotted. The latter are obtained from the extrapolation of the track direction - measured by the spectrometer - to the RICH plane. Results from the fit are 2.96 mm and 2.92 mm for the X and Y resolutions respectively.

Particle identification in LKr is based on the ratio E/p between the energy deposit in the calorimeter and the track momentum; in Figure 2.21 the E/p distributions for muons, pions and positrons are reported.

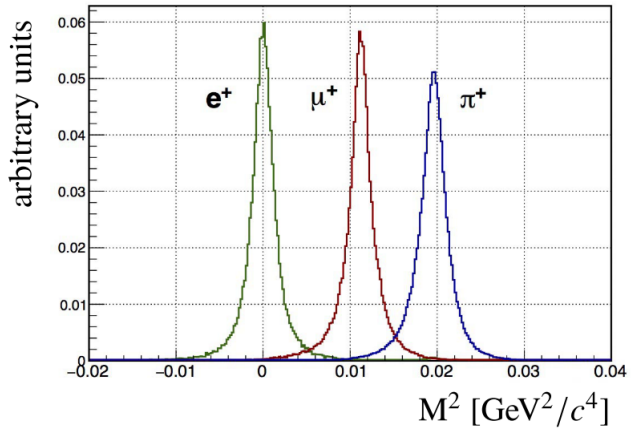

Figure 2.18: Squared masses distributions for e^+, μ^+ and π^+ in the momentum range $[15 - 35]$ GeV/c. The masses are obtained using the velocity of the particles estimated by the RICH and their momentum from the STRAW spectrometer. Figure from [33].

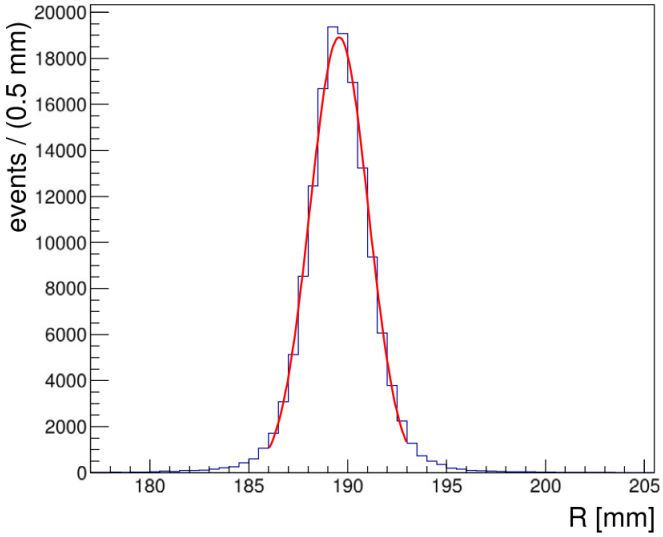

Figure 2.19: Gaussian fit to the radius of the Cherenkov ring produced by positrons in the RICH. Figure from [38].

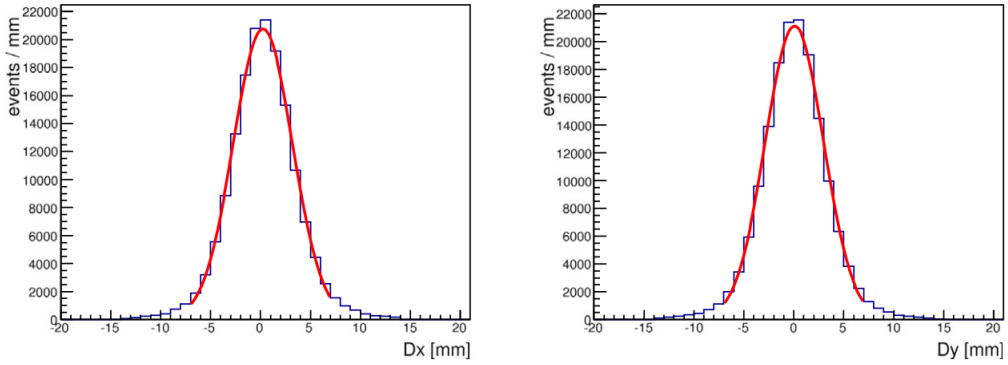

Figure 2.20: Difference between the fitted and the expected X (left) and Y (right) positions of the RICH ring centre for a positron sample. Figure from [38].

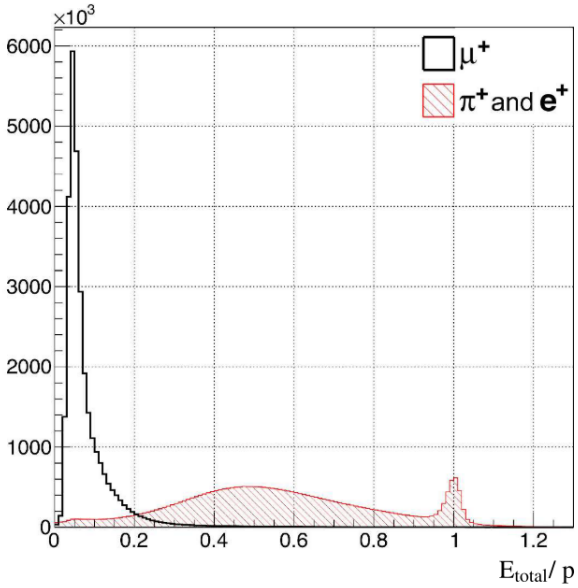

Figure 2.21: E/p distributions for muons, pions and positrons. Figure from [33].

Chapter 3

Event Selection

3.1 Experimental strategy

As discussed in Chapter 1, the measured value of R_K is statistically limited by the number of K_{e2} decays collected, while $K_{\mu 2}$ events are more abundant thanks to the larger Branching Ratio (BR). The total sample used to perform the previous measurements can be easily overcome since data collected by NA62 represent the largest sample in the world concerning most of kaon decays, including K_{l2}. Figure 3.1 shows the number of kaon decays collected by NA62 over the 2017 data taking, considering all the different trigger streams: a total number of kaon decays in the fiducial volume of about 3×10^{12} has been achieved.

In order to minimize the systematic uncertainties due to the trigger, a collection of K_{l2} decays using the same stream is preferred; NA62 TDAQ system allows to use several trigger streams simultaneously but, in order to keep the data rate under control, a downscaling factor (D) is applied to most of them. The ideal performances are obviously obtained choosing a common trigger stream with $D = 1$ and the only mask with this characteristic adopted by NA62 is the PNN configuration, used - as the name suggests - to collect the sample for $BR(K^+ \to \pi^+ \nu\bar{\nu})$ measurement.

It consists on the combination of a level 0 (L0) hardware trigger and a level 1 (L1) software algorithm, described in the next section.

The choice of the PNN trigger stream, however, present some disadvantages, as LKr and especially MUV3 are used in veto. The latter is a clear limitation to the possibility of collecting a sample of $K_{\mu 2}$. The way to have

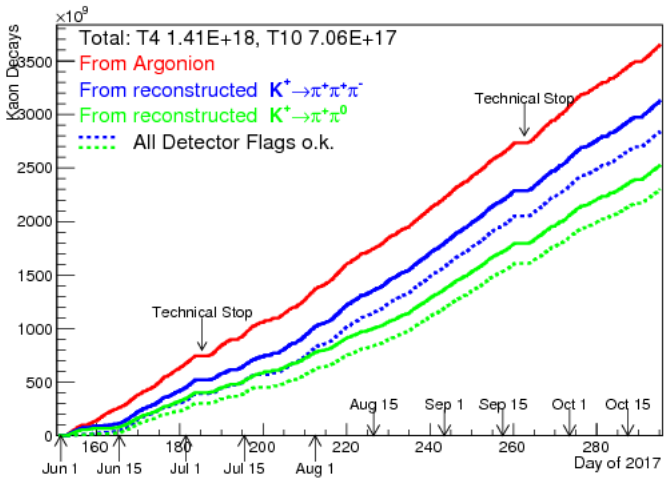

Figure 3.1: NA62 integrated number of kaon decays in 2017 data taking. The red curve refers to the delivered beam, measured by a ionization chamber at the end of K12 beamline, while blue and green ones refer to $K_{2\pi}$ and $K_{3\pi}$ decays respectively. Effects due to the veto of events because of random activities in the detectors - which plays a bigger role in $K_{2\pi}$ selection - are not taken into account.[39]

both a not-downscaled trigger stream and a $K_{\mu 2}$ sample which is statistically larger than the K_{e2} one is to extract $BR(K_{\mu 2})$ from a sample of

$$K^+ \to \mu^+ \nu_\mu \quad \mu^+ \to e^+ \nu_e \bar{\nu}_\mu \tag{3.1}$$

called $K_{\mu e}$ in the following. R_K value, then, is obtained by the formula:

$$R_K = \frac{N^{data}_{K_{e2}} - N^{bg}_{K_{e2}}}{N^{data}_{K_{\mu e}} - N^{bg}_{K_{\mu e}}} \frac{A_{Ke2}}{A_{K\mu e}} \tag{3.2}$$

as the trigger efficiency in Equation 1.21 cancels out.

A common selection is adopted proceeding through the following steps:

- single downstream track selection, in time with the trigger;
- upstream kaon identification, in time with the track;
- no more than two clusters in LKr, corresponding to the positron and the IB photon;
- no activity in the other veto detectors;
- downstream track identified as positron by LKr and RICH.

After the selection, K_{e2} and $K_{\mu 2}$ regions can be easily identified using m^2_{miss}, the squared missing mass defined as

$$m^2_{miss} = (P_K - P_e)^\alpha (P_K - P_e)_\alpha \tag{3.3}$$

where P_K and P_e represent the four momentum of the kaon and that of the downstream track under the positron mass hypothesis, respectively. The distributions for m^2_{miss} for two MonteCarlo samples of K_{e2} and $K_{\mu e}$ are shown in Figure 3.2.

3.2 PNN trigger stream

PNN trigger is a two-level trigger mask, made by a Level 0 (L0) software and a Level 1 (L1) software component. L0 response is obtained by the combination of signals from several detectors: RICH, CHOD, LKr and MUV3; since LKr and MUV3 are used in veto, they have to satisfy no signal condition. Data

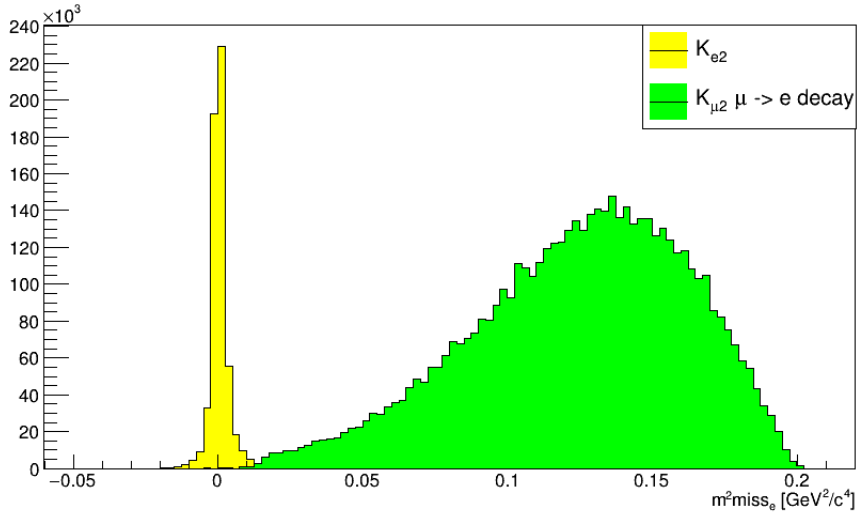

Figure 3.2: Squared missing mass distribution for MonteCarlo samples of K_{e2} and $K_{\mu e}$ decays

from each detector involved in the trigger chain are organized in **primitives**, namely 64 bit words containing the time of the event and its characteristics, and then sent to L0TP. In order to be considered, the primitives time has to be in a ± 6.5 ns with respect to the time of the RICH primitive. The trigger conditions are optimized on the experimental signature characterizing $K^+ \to \pi^+ \nu\bar{\nu}$ decay: an upstream kaon, identified by the KTAG, matched with a single downstream track with Cherenkov light produced in the RICH vessel with no extra activity in the veto detectors. The L0 PNN condition is:

$$CHOD \cdot !Qx \cdot UTMC \cdot RICH \cdot !L0calo \cdot !MUV3 \tag{3.4}$$

where "$\cdot$" and "!" represent the logical operators AND and NOT respectively. Each condition is satisfied by the following criteria:

- $CHOD$: at least one primitive from CHOD;
- Qx: hits in two adjacent CHOD quadrants;
- $UTMC$: no more than 4 hits in the CHOD;
- $RICH$: at least two hits in time;

- *L0calo*: more than 2 clusters or total energy deposit greater than 40 GeV;
- $MUV3$: at least one hit in time.

Once the event pass L0, data from all the detectors are sent from the temporary buffers installed on the front end boards to the PC farm. Here L1 algorithms are implemented: PNN trigger stream uses at L1 information coming from KTAG, LAV and STRAW: KTAG algorithm select events in time with L0 trigger with hits in more than 4 sectors. LAV is used in veto, rejecting events with more than 3 hits in a ± 5 ns time window. Finally STRAW algorithm ensures that the event contains at least one reconstructed track with longitudinal momentum component P_z smaller than 50 GeV/c.

3.3 Background contributions

The choice of selecting $K_{\mu 2}$ events from the muon decay products has the disadvantage of having background contribution entering in the $K_{\mu e}$ region, while the K_{e2} peak can be reconstructed in an almost zero background environment. In principle, all the decays with a positron in the final state can be considered a potential background source and should be taken into account. Background events are estimated using MonteCarlo simulations and then subtracted to the number of signal candidates, taken from data.

3.3.1 Upstream decays

The subsequent muon decay in flight for the $K_{\mu 2}$ mode does not allow to apply strict conditions on the vertex between the positron and the kaon; this leads to a irreducible background coming from "upstream" decays, namely decays of beam particles between the end of the CEDAR and GTK3. Upstream decays, referred to kaons as well as pions, need to be in time with an accidental K^+ in order to pass the selection criteria in the KTAG and GTK (described in Section 3.6.2); the accidental particle, then, must not decay because additional activity in the detectors would cause the event to be discarded. This is not an unlikely possibility since given the beam momentum and kaon lifetime, almost 90% of K^+ do not decay in the fiducial region. This contribution, however, is partially suppressed reducing the time window for coincidences between the upstream detectors.

3.3.2 Beam pion decays

Pion decays can occur not only in the upstream region but mostly in the decay volume, thanks to the larger dimensions of the fiducial region ($Z^{start}_{STRAW} - Z_{GTK3} \approx 77$ m) compared to the upstream one ($Z_{GTK3} - Z^{end}_{CEDAR} \approx 33$ m). Background can come from both $\pi^+ \to e^+\nu_e$ and $\pi^+ \to \mu^+\nu_\mu$ with subsequent muon decay in flight. Pion background is partially rejected by the timing coincidences between KTAG and RICH, while the remaining contribution is estimated using MonteCarlo simulations.

3.3.3 Direct emission (DE) K_{e2} decays

As discussed in Section 1.3, the definition of R_K includes inner bremsstrahlung (IB) emissions for the leptons, but radiative photons can be produced also by direct emission (DE) processes. Two distinct component of DE $K_{e2\gamma}$ decay can be due defined, depending on the polarization of the photon, which are labelled as $K_{e2\gamma}SD^+$ and $K_{e2\gamma}SD^-$. Both decay modes can contribute as background for $K_{\mu 2}$, as they are distributed in the positive side of m^2_{miss} distribution, without the peak at 0 because of the γ. The background contribution for $K_{e2\gamma}SD^\pm$ is reduced with respect to the previous measurement thanks to the photon veto system, which rejects with high efficiency events with extra photons.

3.3.4 K_{e3} decays

K_{e3} decay represented in the 2013 measurement a sizable background contribution and a non negligible source of systematic uncertainties, as well as $K_{e2\gamma}$. Also in this case, the installation of an hermetic and highly efficient photon veto system allows to have almost zero contribution from this decay.

3.3.5 Muon halo

Kaon and pion decays along the beamline produce a large number of muons that travel along the experimetal setup following the beam. This "muon halo" can give a contribution to R_K in case of a muon decay in flight matched in time with an upstream kaon. Part of the contribution has been already taken into account in the "upstream" decay modes; in addition, a dedicated

MonteCarlo simulation has been produced to account for muons produced before the CEDAR vessel.

3.3.6 Other decay modes

Also other kaon decay modes have been considered as potential background, like $K^+ \to \pi^+\pi^0$ ($K_{2\pi}$), $K^+ \to \pi^+\pi^+\pi^-$ ($K_{3\pi}$) and $K^+ \to \mu^+\pi^0\nu_\mu$ ($K_{\mu 3}$), although tiny background contributions from them are expected.

3.4 Data and MC samples

3.4.1 Data

Data sample used for this analysis has been collected by the NA62 collaboration in 2017 in a month of data taking. Data are organized in sets called **runs** of comparable length, typically corresponding to 8 hours. Each run is made by $\sim$ 1500 subsets or **bursts**, corresponding to SPS proton delivery cycles. The duration of one burst is 6 s while the period between two consecutive burst can vary depending on SPS operational conditions.

The beam intensity, measured in terms of number of proton impinging on T10, was not constant during the data taking. In Figure 3.3 the average intensity for each run of the data sample is reported; the average is based on the instantaneous intensity for each event, measured by the intensity in MHz on GTK.

3.4.2 MonteCarlo simulation

MonteCarlo simulation has been produced using GEANT4 software [40]. The simulation allows to reproduce:

- the beamline and the magnetic fields starting from KTAG;
- the geometry and the materials of the detectors
- the physics processes or particle interactions with matter and their decays.

To validate the assumption of the cancelation of systematic effects in the ratio R_K due to the trigger, an emulation of L0 PNN mask has been

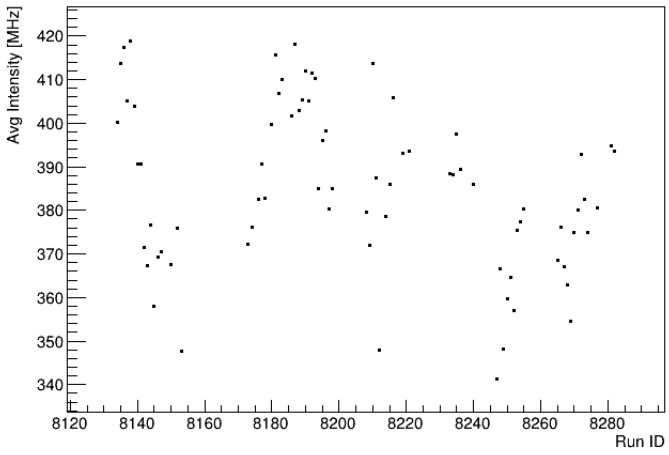

Figure 3.3: Beam intensity as a function of Run ID, estimated by the average on each run of the out-of-time activity in the GTK.

implemented; the emulated trigger, then, has been applied to MonteCarlo samples to evaluate the change in R_K. At the time of submission of this thesis, no L1 emulation was available in MonteCarlo production.

In order to reduce the CPU time necessary to produce a large enough $K_{\mu e}$ sample, the following approach has been adopted: muons from $K_{\mu 2}$ decays have a minimum energy in the laboratory frame of 3.2 GeV. The downstream region, from GTK3 to MUV3, has a length of 138 m $\approx 0.73\%\lambda$, where $\lambda = \beta\gamma c\tau$ is the decay length of the muons and $\tau = 2.2\ \mu s$ their lifetime. Therefore only muons with proper time $t^* < 0.0073\tau$ have been simulated since those exceeding this threshold would not decay in the apparatus. This approach speed up the simulation time by a factor $\frac{1}{1-e^{-0.0073}} \approx 137$. The same approach, with different speed up factors, has been used to produce $K_{\mu e}$ upstream , $\pi_{\mu e}$ and $\pi_{\mu e}$ upstream samples. In Table3.1 the list of the MC samples considered - with an validated description of L0 PNN emulators - and their size is reported.

3.5 Preselection

A common selection is used to collect K_{e2} and $K_{\mu e}$ samples, as mentioned in Section 3.1. The common selection is made by a preselection, i.e. a loose

Decay	Sample size
K_{e2}	1 M
$K_{\mu e}$	18 M
$K_{\mu e}$ UPS	31 M
π_{e2}	30 M
$\pi_{\mu e}$	30 M
$\pi_{\mu e}$ UPS	1 M
K_{e3}	1 M
K_{e3} UPS	20 M
$K_{e2\gamma}$ SD^+	1 M
$K_{e2\gamma}$ SD^-	1 M
K_{e2} UPS	1 M
$K_{2\pi}$	50 M
$K_{3\pi}$	50 M
$K_{\mu 3}$	10 M
π_{e2} UPS	1 M
halo	20 M

Table 3.1: Size of the MonteCarlo samples used

selection to reduce the files size, and a second part where the cut on the physical quantities are applied. This approach allows to speed up the CPU time required for the analysis and for the studies of systematic effects related to the analysis cuts. The preselection proceeds through the following steps:

- downstream track selection;
- upstream track selection;
- upstream - downstream matching;
- timing coincidence;
- veto conditions;
- preliminary particle identification;

In the following sections, two terms are largely used: detector **hits** and **candidates**; hits are referred to signals in a specific element of the detector, while candidates are obtained from the combination of hits. As an example,

LKr hits are the energy deposits in a single cell while clusters of cells are referred to as LKr candidates.

3.5.1 Tracks selection

The starting point of event selection is the downstream track reconstruction. A positively charged track is selected, with hits in at least three of the four STRAW chambers in order to allow one inefficient station in the spectrometer. The track has to be associated with a Cherekov ring reconstructed by the RICH and the time of the RICH candidate is used as the track time, thanks to its better time resolution compared to the STRAW. The selected track is the closest in time with respect to the time of the trigger. The association between STRAW and RICH is considered successful if $\Delta_{Ringcentre} < 10$ mm, where $\Delta_{Ringcentre}$ is the distance between the expected ring centre position - given by the extrapolation of the track momentum to the RICH - and the fitted ring centre position. At this stage, tracks are selected in the momentum range [5;40] GeV/c. A cut on the track χ^2 allows to select only good quality positron candidates. The track has to be in acceptance of the four spectrometer chambers, RICH, CHOD, LKr, MUV1, MUV2 and MUV3. A cluster has to be present in the LKr, associated in space and time to the downstream track, with a distance from any dead cell greater than 20 mm.

To reject events with multiple tracks like $K_{3\pi}$, no spectrometer candidates have to be in time with the selected track in a ± 5 ns window.

3.5.2 Upstream selection

The dowstream track time is used to select one candidate in the KTAG, corresponding to the upstream kaon. The closest candidate in time is selected, with the additional requirement that the candidate has to be produced by the coincidence of light in more than 4 sectors. The KTAG candidate is then matched with the closest in time candidate in GTK.

No vertex fit is used, since the muon decay in flight for $K_{\mu e}$ events does not allow to perform a strict vertex selection, therefore the two tracks are matched looking at the closest distance of approach (CDA): at this stage, no cut on the CDA is applied.

3.5.3 Timing

The excellent time resolutions of KTAG, GTK and RICH - $O(100$ ps) allows to realize strict timing coincidences between the upstream and downstream detectors, reducing the accidental background contribution. In the preselection, however, a loose timing condition is applied, asking for:

$$|t_{RICH} - t_{KTAG}| < 5 \text{ ns} \tag{3.5}$$

$$|t_{GTK} - t_{KTAG}| < 5 \text{ ns} \tag{3.6}$$

$$|t_{RICH} - t_{trigger}| < 5 \text{ ns} \tag{3.7}$$

$$|t_{RICH} - t_{GTK}| < 5 \text{ ns} \tag{3.8}$$

The choice of not applying a strict timing coincidence has been made to have the possibility to select a pure sample of pion decays, without the strict timing requirement between KTAG and RICH, and scale properly the MonteCarlo samples of pion decays.

3.5.4 Veto

The photon veto system is one of the major upgrades of the NA62 apparatus and it is extremely effective to reject background. Veto detectors for this analysis are LAV, IRC, SAC, CHANTI and - partially - LKr. No hits in time are allowed in IRC, SAC and in the 12 LAV stations in a time window of ± 5 ns, centered around the time of the track provided by the RICH.

In LKr, as mentioned in Section 3.5.1, one cluster associated to the track has to be selected; an additional cluster is also allowed if compatible with the photon produced by inner bremmstrahlung (IB) radiative decay. The radiative photon is allowed around its expected position, defined by a straight line extrapolation of the track direction to LKr plane. The maximum distance between the extrapolated point and the cluster, in order to be considered as due to radiative photon, is 50 mm. A threshold on the energy of the extra photon has to be applied since the current emulation of L0calo is not able to reproduce well the distribution observed on data: in Figure 3.4 the distributions of the extra cluster energy are reported, with and without the trigger emulation. A lack of MonteCarlo contribution can be observed when the trigger emulator is applied.

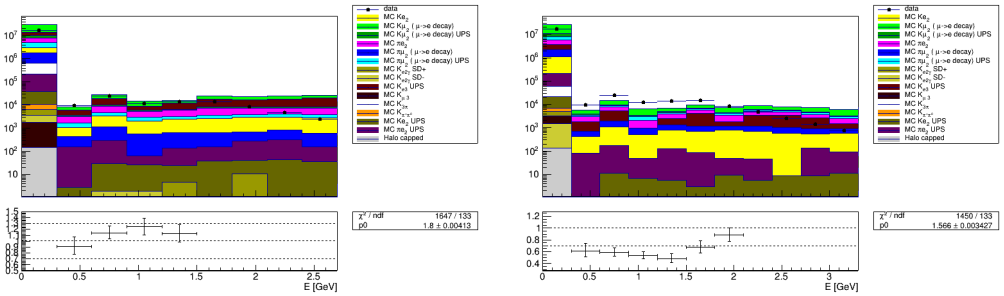

Figure 3.4: Distribution of the energy of the bremsstrahlung photon without (left) and with (right) the L0 trigger emulation applied.

Apart from the cluster associated to the track and the possible additional cluster due to IB, no other clusters with energies above 500 MeV are allowed in a ± 10 ns with respect to the track time.

Finally, upstream background and events with interactions between the beam and GTK spectrometer are rejected selecting events with no candidates in CHANTI in in a ± 3 ns time window centered around the time of the K^+ measured by KTAG.

3.5.5 Particle Identification

Positron Particle IDentification (PID) is based mainly on the RICH response but also on the activity in LKr and MUV3 detectors. RICH hits are associated to the charged track and a maximum likelihood fit of the ring under the different mass hypotheses is performed. Only events with maximum likely hypotesis corresponding to positrons are selected.

The fast muon veto detector (MUV3) is another hardware improvement compared to setup used for the 2013 R_K measurement and it is useful to reject residual undecayed muons. No MUV3 candidates have to be present in the events within a ± 5ns time window centered around track time.

3.6 Analysis cuts

After the preselection, the following requirements on the physical quantities are used to refine the event selection. Only MonteCarlo events that satisfy the L0 PNN emulated trigger conditions are selected. The cut chosen for

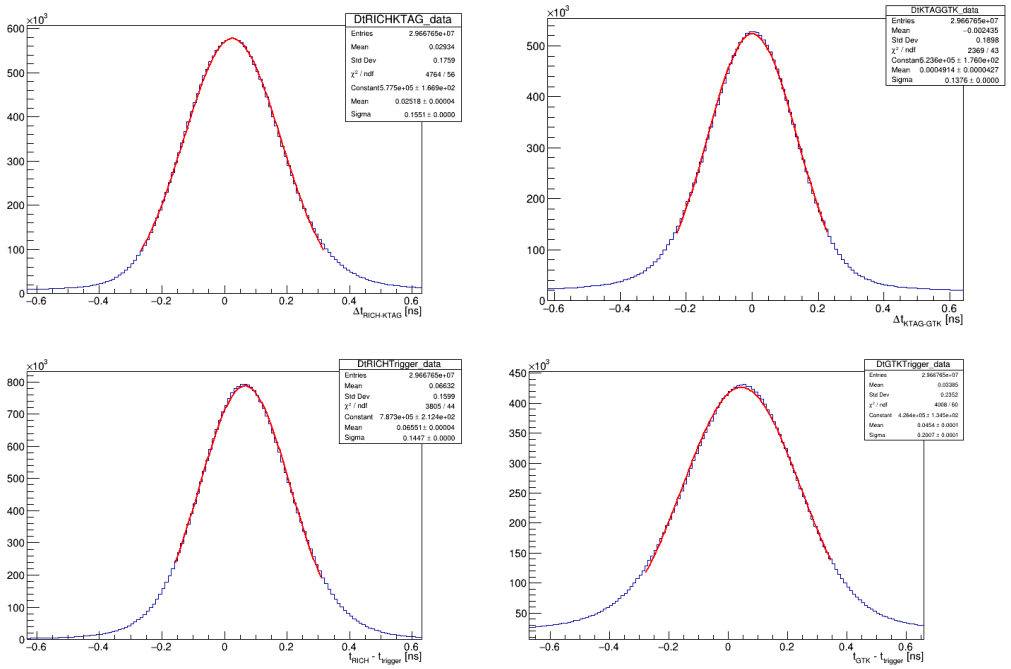

Figure 3.5: Time differences between subdetectors in data. Top: $t_{RICH} - t_{KTAG}$ (left), $t_{KTAG} - tGTK$; bottom: $t_{RICH} - t_{trigger}$ (left), $t_{GTK} - t_{trigger}$.

the maximum energy of the bremsstrahlung photon is 2 GeV; as discussed before, the lack of MonteCarlo events in the distribution, shown in Figure 3.4, could lead to a systematic effect, which will be taken into account.

Stricter time coincidences are requested:

$$|t_{RICH} - t_{KTAG}| < 0.5 \text{ ns} \tag{3.9}$$

$$|t_{GTK} - t_{KTAG}| < 0.5 \text{ ns} \tag{3.10}$$

$$|t_{RICH} - t_{trigger}| < 0.5 \text{ ns} \tag{3.11}$$

$$|t_{RICH} - t_{GTK}| < 0.5 \text{ ns} \tag{3.12}$$

Figure 3.5 shows the four time differences distributions obtained on data; a gaussian fit to each peak is also reported.

The tracks are selected in the momentum range [12.5; 32.5] GeV/c: this value have been chosen to avoid systematic effects due to positron misreconstruction at low momenta and to the trigger at high P_{track}, due to the

threshold on the maximum energy deposition in the LKr (Figure 3.6). The Z coordinate of the vertex has to be located in the decay volume, between 110 and 180 m from T10 (Figure 3.7). Events are selected up to 180 m - close to the starting plane of the spectrometer - since the distribution of K_{e2} events peaks to high values of the Z coordinate.

In addition to RICH likelihood, PID is performed selecting a region between 0.85 and 1.15 in the distribution of E/p, namely the ratio between the energy deposit of the track in the LKr and its momentum measured by the STRAW spectrometer, shown in Figure 3.8. Also in this case, a discrepancy between data and MonteCarlo around the peak of the distribution is observed and its effect in terms of systematic uncertainty on the measurement will be discussed in the next chapter.

Kaon momentum distribution shows a sizeable disagreement between data and MonteCarlo (Figure 3.9); the momentum reconstruction in GTK strongly depends on the station alignment procedure, which is clearly not optimal at present. Upstream tracks are selected in the momentum range [73; 77] GeV/c, however an improved algorithm for measuring beam particles momenta is under development. The discrepancy in the kaon momentum affects also the definition of the squared missing mass and it can provide a possible systematic uncertainty on R_K, which will be estimated in the next chapter.

Finally, a loose cut on the CDA at 150 mm is also applied and its distribution is shown in Figure 3.10

3.7 K_{e2} and $K_{\mu 2}$ regions

In Figure 3.11 the distribution of the squared missing mass between the kaon track and the downstream track - in the positron mass hypothesis - for data and MonteCarlo is reported. From m^2_{miss} distribution it is possible to define K_{e2} and $K_{\mu 2}$ regions:

$$K_{e2} \text{ region} : \mathrm{m}^2_{\mathrm{miss}} < 0.015 \text{ GeV}^2/\mathrm{c}^4 \tag{3.13}$$

$$K_{\mu 2} \text{ region} : \mathrm{m}^2_{\mathrm{miss}} > 0.02 \text{ GeV}^2/\mathrm{c}^4 \tag{3.14}$$

A comparison with Figure 1.7 allow to highlight the impact of the experimental layout improvements in terms of background contamination for the two channels; in particular, the K_{e2} peak is now in an almost zero background environment.

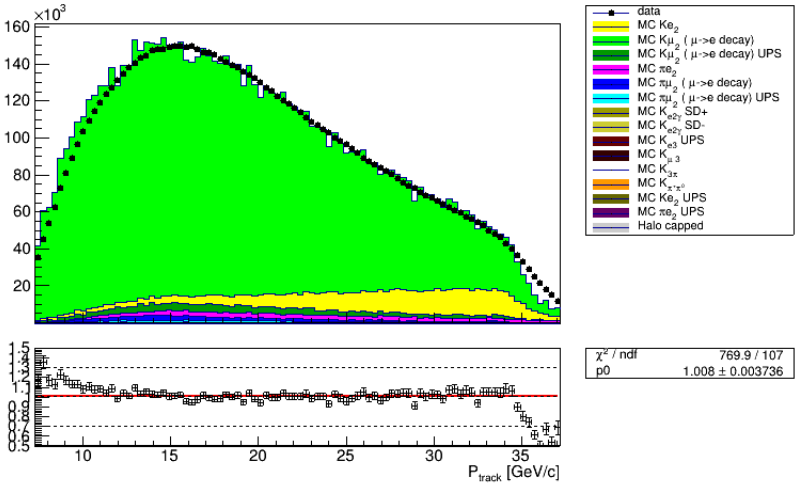

Figure 3.6: Distribution of the positron momentum

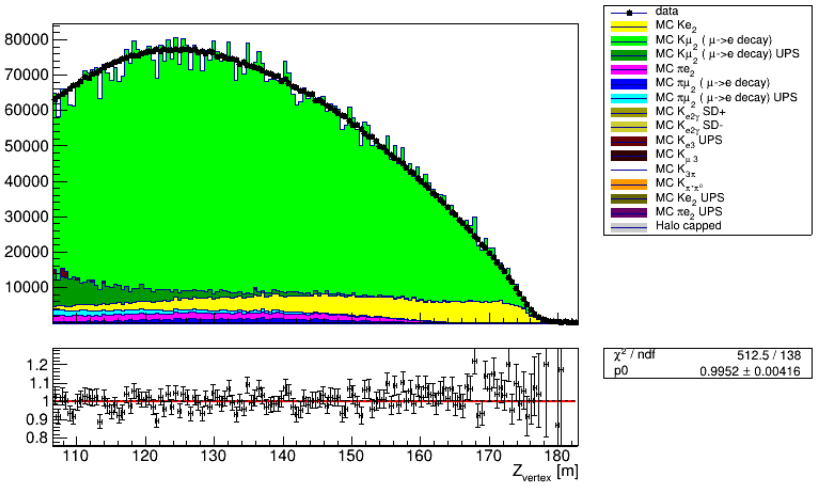

Figure 3.7: Distribution of the Z coordinate of the vertex

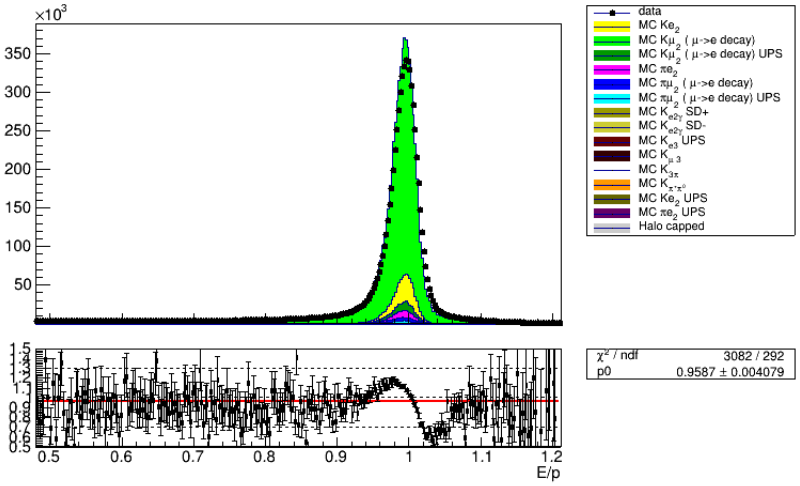

Figure 3.8: Distribution of the ratio between the energy deposit in LKr and the track momentum

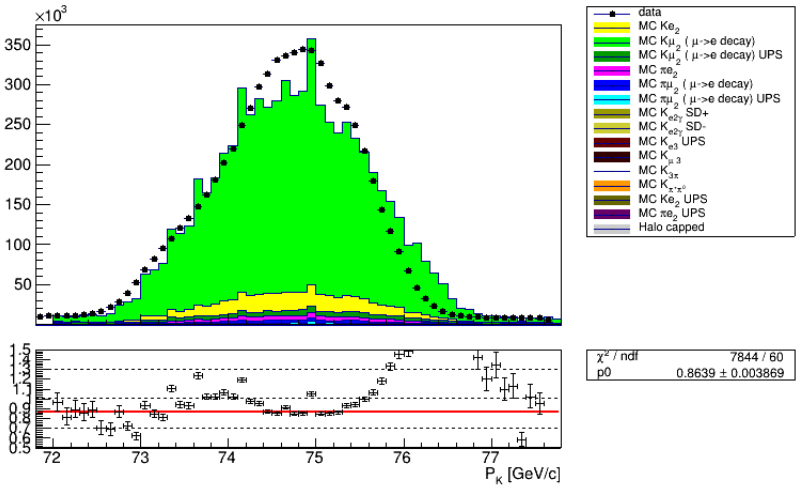

Figure 3.9: Distribution of the kaon momentum measured by GTK

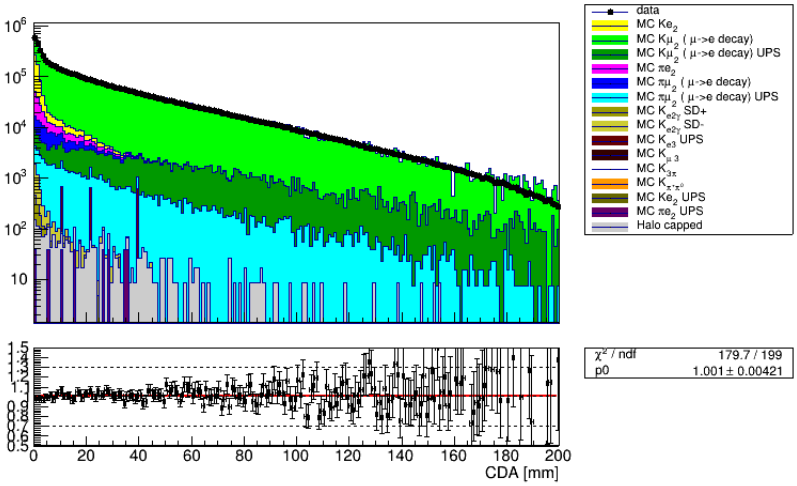

Figure 3.10: Distribution of the closest distance of approach (CDA) between the upstream and the downstream track

Requirement	$Acc_{K_{e2}}$	$Acc_{K_{\mu e}}$
Downstream track selection	0.206	1.59×10^{-3}
KTAG selection	0.206	1.59×10^{-3}
GTK selection	0.203	1.57×10^{-3}
Vertex	0.179	1.38×10^{-3}
Timing (± 5 ns)	0.155	1.25×10^{-3}
Photon veto	0.132	6.83×10^{-4}
Particle ID (RICH and MUV3)	0.128	3.67×10^{-5}
Emulated trigger	0.090	3.42×10^{-5}
$E_\gamma < 2$ GeV	0.089	3.41×10^{-5}
Timing (± 0.5 ns)	0.088	3.39×10^{-5}
$12.5 < P_e < 32.5$ GeV/c	0.065	2.44×10^{-5}
$110 < Z < 180$ m	0.063	2.04×10^{-5}
$0.85 < E/p < 1.2$	0.063	1.78×10^{-5}
$73 < P_K < 77$ GeV/c	0.0614	1.72×10^{-5}
$CDA < 150$ mm	0.0614	1.71×10^{-5}
K_{e2} region	0.0611	-
$K_{\mu e}$	-	1.70×10^{-5}

Table 3.2: Acceptances for K_{e2} and $K_{\mu e}$ MonteCarlo samples after each of the selection steps

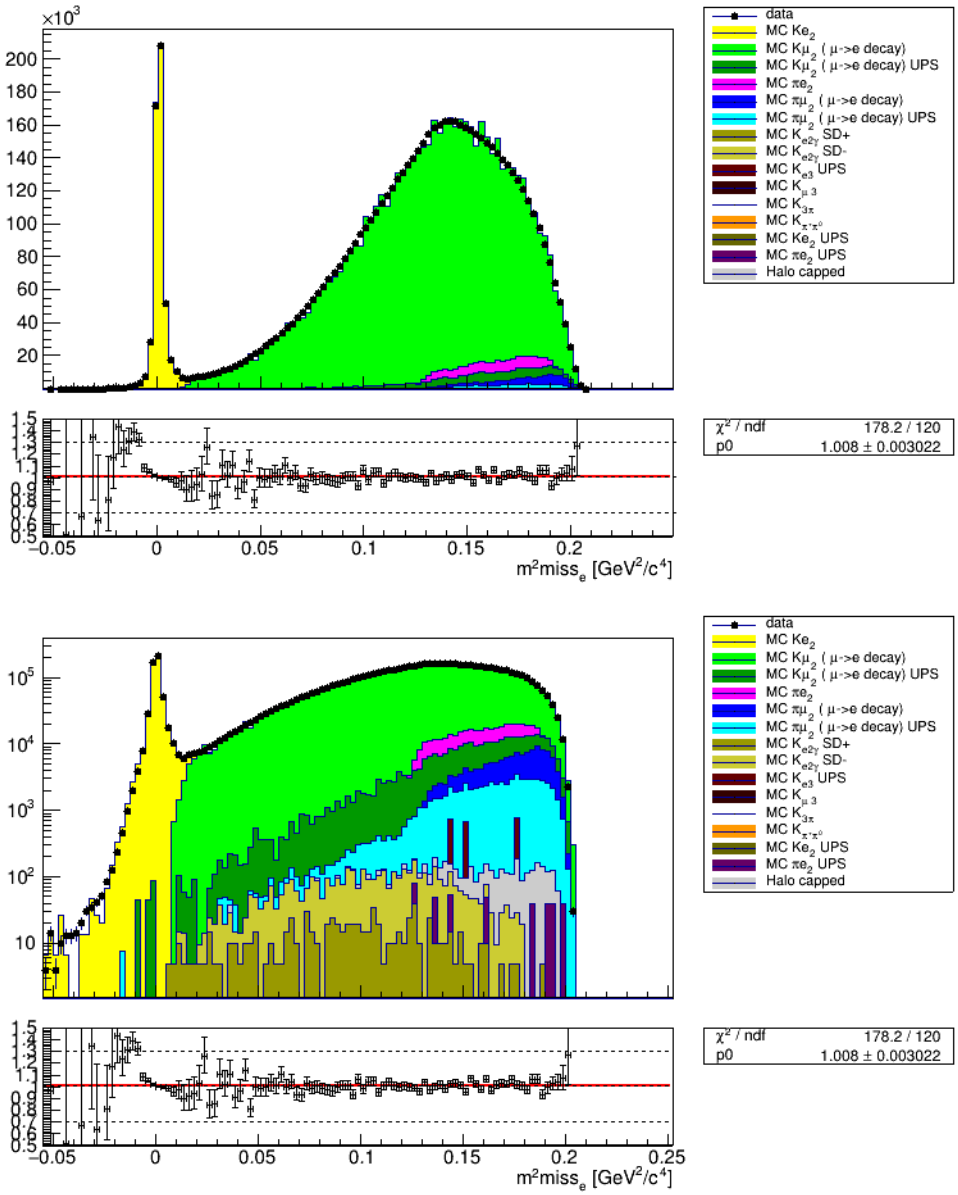

Figure 3.11: Distribution of the squared missing mass between the upstream kaon and the downstream track in the positron mass hypothesis in linear (top) and logarithmic scale (bottom).

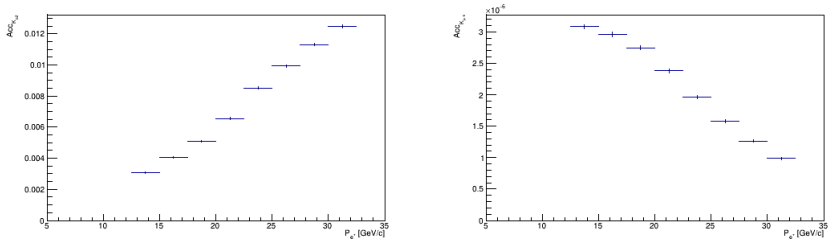

Figure 3.12: Acceptances of K_{e2} (left) and $K_{\mu e}$ (right) samples in bins of the positron momentum.

The acceptances for K_{e2} and $K_{\mu e}$ samples are:

$$Acc_{K_{e2}} = (6.11 \pm 0.02) \times 10^{-2} \tag{3.15}$$

$$Acc_{K_{\mu e}} = (1.696 \pm 0.008) \times 10^{-5} \tag{3.16}$$

Table 3.2 summarizes the changes in the acceptances after each of the analysis steps, while the acceptances in bins of the positron momentum are reported in Figure 3.12.

3.8 Kaon and Pion MC normalization

MonteCarlo simulation of kaon and pion decays is scaled to the number of kaon and pion decays collected in data. The number of kaon decays is obtained from the events in the K_{e2} region as:

$$N_K = \frac{N_{K_{e2}}}{BR_{K_{e2}} \cdot Acc_{K_{e2}}} \tag{3.17}$$

In the data sample used for this analysis, the number of kaon decays collected are:

$$N_K = (5.346 \pm 0.019_{stat} \pm 0.024_{ext}) \times 10^{11} \tag{3.18}$$

In the last equation, the first error contains the contributions due to $N_{K_{e2}}$ and from the acceptance, while the second term is due to the uncertainty on K_{e2} Branching Ratio. The number of kaon decays is used only to scale MonteCarlo simulation in order to extract the number of expected background

events in the K_{e2} and $K_{\mu e}$ regions, therefore the effect of N_K on the final result is negligible.

Following a similar approach, the number of pion decays has been estimated counting the number of π_{e2} events in data with a slightly modified selection: the only differences with respect to the selection described above are related to the timing conditions, where only a coincidence between RICH, trigger and GTK is applied, and to the CDA, where a tighter cut at 0.4 mm is used. This allows to select a pure π_{e2} samples applying a cut on the squared missing mass in the beam pion hypothesis:

$$\pi_{e2}\ region : |m^2_{miss\pi e}| < 0.001\ \mathrm{GeV}^2/\mathrm{c}^4 \tag{3.19}$$

The distribution of $m^2_{miss\pi e}$ is reported in Figure 3.13.

The total π_{e2} events in data and acceptance of the π_{e2} selection are:

$$N_{\pi_{e2}} = (1.714 \pm 0.004_{stat}) \times 10^5 \tag{3.20}$$

$$Acc_{\pi_{e2}} = (1.837 \pm 0.008) \times 10^{-3} \tag{3.21}$$

The number of pion decays, then, is:

$$N_\pi = \frac{N_{\pi_{e2}}}{BR_{\pi_{e2}} \cdot Acc_{\pi_{e2}}} = (2.449 \pm 0.019 \pm 0.008) \times 10^{11} \tag{3.22}$$

As for N_K, the first uncertainty is due to $N_{\pi_{e2}}$ and to the selection acceptance while the second term is due to the experimental uncertainty of $BR(\pi_{e2})$.

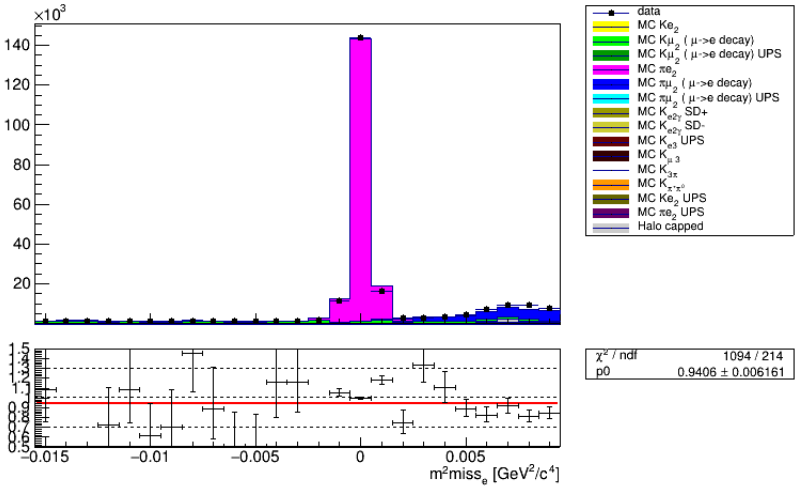

Figure 3.13: Distribution of the squared missing mass in the beam pion hypothesis for the upstream track: a clean peak at 0, corresponding to π_{e2} decays, is clearly visible.

Chapter 4

Results

4.1 Number of K_{e2} and $K_{\mu e}$ events

The measurements of R_K has been performed in 8 bins of momentum, 2.5 GeV/c wide, from 12.5 to 32.5 GeV/c. A constant fit is used on the binned data to extract the measured value with its statistical uncertainty. In Figures 4.1 and 4.2, the number of events collected in the two signal regions in bins of the positron momentum are reported.

The K_{e2} region, as stated before, contains tiny background contributions compared to previous experiments; the domininant background is due to $K_{\mu e}$ tail and $K_{\mu e}$ upstream decays. On the other hand, several decay modes can enter in the $K_{\mu e}$ region, the most relevant ones being upstream $K_{\mu e}$ and beam pion decays. Radiative $K_{e2\gamma}$, K_{e3} and events from muon halo decays play a less relevant role compared to the previous measurement performed by NA62 [27] thanks to the high-efficiency and hermetic photon veto system. No K_{e3} events, in particular, are observed due to the limited MC sample available. Since the contributions due to $K_{e2\gamma}$ and halo decays are reduced by more than one order of magnitude compared to the previous measurement, no systematic effects due to the uncertainty on $K_{e2\gamma}$ Branching Ratio and halo description are considered.

The number of K_{e2}, $K_{\mu e}$ and the number of background events in each momentum bin are reported in Table 4.1. The uncertainty on the number of background events is dominated by the number of events entering K_{e2} and $K_{\mu e}$ regions, due to the limited MonteCarlo sample size; therefore, the contributions to the uncertainty due to N_K and the BRs can be considered

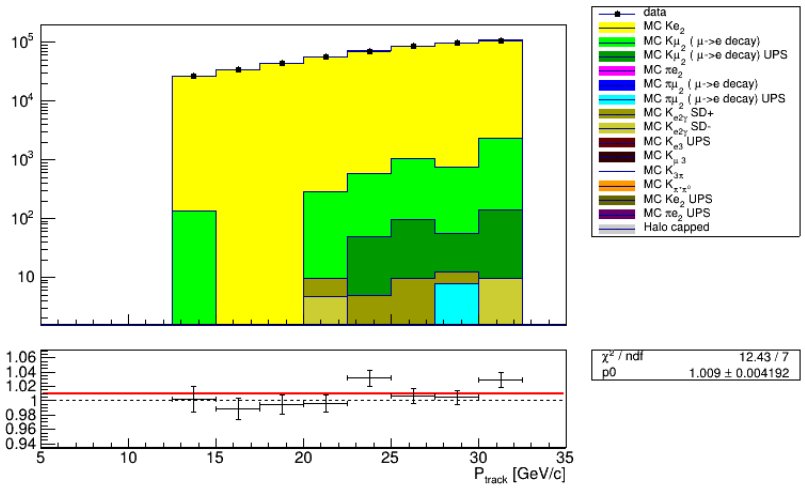

Figure 4.1: Distribution of events entering K_{e2} region in bins of positron momentum.

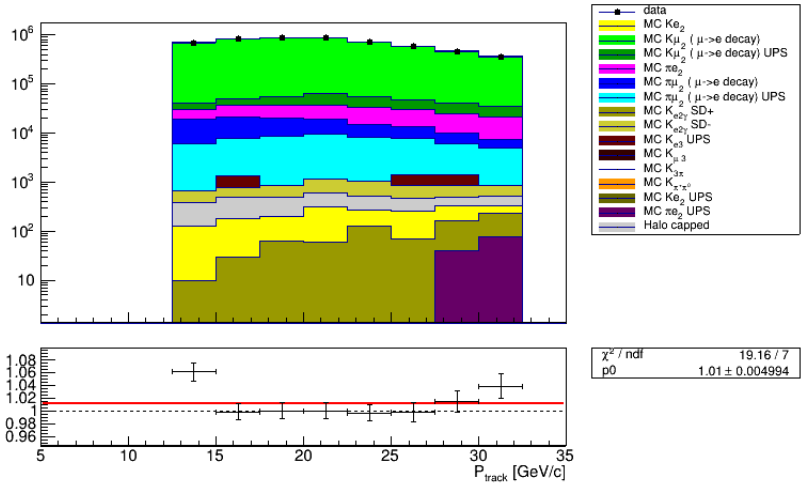

Figure 4.2: Distribution of events entering $K_{\mu e}$ region in bins of positron momentum.

Bin	$N^{data}_{K_{e2}}$ ($\times 10^4$)	$N^{bg}_{K_{e2}}$	$N^{data}_{K_{\mu e}}$	$N^{bg}_{K_{\mu e}}$ ($\times 10^4$)
1	2.616 ± 0.016	138 ± 138	$(1.0793 \pm 0.0010) \times 10^6$	7.72 ± 0.13
2	3.459 ± 0.018	-	$(1.0967 \pm 0.0010) \times 10^6$	8.04 ± 0.14
3	4.34 ± 0.02	-	$(1.0103 \pm 0.0010) \times 10^6$	7.31 ± 0.13
4	5.59 ± 0.02	$(2.8 \pm 1.9) \times 10^2$	$(8.745 \pm 0.009) \times 10^5$	6.49 ± 0.12
5	7.05 ± 0.03	$(6 \pm 3) \times 10^2$	$(7.257 \pm 0.008) \times 10^5$	5.54 ± 0.11
6	8.46 ± 0.03	$(1.1 \pm 0.4) \times 10^3$	$(5.877 \pm 0.008) \times 10^5$	4.79 ± 0.12
7	9.61 ± 0.03	$(7 \pm 3) \times 10^2$	$(4.632 \pm 0.007) \times 10^5$	4.06 ± 0.11
8	10.51 ± 0.03	$(2.3 \pm 0.8) \times 10^3$	$(3.559 \pm 0.006) \times 10^5$	3.48 ± 0.08

Table 4.1: Number of K_{e2}, $K_{\mu e}$ and respective background events in each momentum bin.

at first approximation negligible.

After the background subtraction, the total number of K_{e2} and $K_{\mu e}$ decays collected are

$$N_{K_{e2}} = (5.112 \pm 0.007 \pm 0.010) \times 10^5 \tag{4.1}$$

$$N_{K_{\mu e}} = (5.719 \pm 0.002 \pm 0.003) \times 10^6 \tag{4.2}$$

where the first uncertainties are due to the poissonian fluctuations of the number of events obtained from data and the other ones correspond to the uncertainty on the background.

The size of $K_{\mu e}$ sample is larger than $N_{K_{e2}}$ because the larger BR of $K_{\mu 2}$ decay compensates the smaller acceptance due to muon decays in flight. At the moment, the uncertainty on the number of background events is the largest, due to the limited MonteCarlo samples size; this uncertainty will drop down as soon as a massive production is started. The measurement, then, is statistically limited by the number of K_{e2} decays collected; however, using only a subsample of the total 2017 dataset, a more than three times greater K_{e2} sample, compared to the most precise R_K measurement, has been collected. From an estimation on the number of kaon decays in full 2017+2018 samples, a factor $O(10)$ larger K_{e2} sample is expected.

4.2 Statistical uncertainties

In each bin, the value of R_K is computed using (3.2) and its statistical error is estimated using the following formula:

$$\sigma_{R_K} = \sigma^{data}_{R_K} \oplus \sigma^{MC}_{R_K} \tag{4.3}$$

where

$$\sigma^{data}_{R_K} = \left(\frac{\sigma_{N^{data}_{K_{e2}}}}{N^{data}_{K_{e2}} - N^{bg}_{K_{e2}}} \oplus \frac{\sigma_{N^{data}_{K_{\mu e}}}}{N^{data}_{K_{\mu e}} - N^{bg}_{K_{\mu e}}} \right) \cdot R_K \tag{4.4}$$

$$\sigma^{MC}_{R_K} = \left(\frac{\sigma_{N^{bg}_{K_{e2}}}}{N^{data}_{K_{e2}} - N^{bg}_{K_{e2}}} \oplus \frac{\sigma_{N^{bg}_{K_{\mu e}}}}{N^{data}_{K_{\mu e}} - N^{bg}_{K_{\mu e}}} \oplus \frac{\sigma_{Acc_{K_{e2}}}}{Acc_{K_{e2}}} \oplus \frac{\sigma_{Acc_{K_{\mu e}}}}{Acc_{K_{\mu e}}} \right) \cdot R_K \tag{4.5}$$

This expression is useful to disentangle the contribution to the statistical uncertainty due to the data sample size, represented by $\sigma^{data}_{R_K}$, and the one due to the MonteCarlo sample size: while the former is fixed once the data collected is fully analyzed, a larger MC production will make the latter smaller.

The number of signal and background events, the acceptances and the statistical uncertainties obtained for R_K in each momentum bin are reported in Table 4.2. The measurement is statistically dominated by the uncertainty due to the limited MonteCarlo sample sizes, which at the moment is larger by a factor ~ 3 with respect to $\sigma^{data}_{R_K}$. In particular, $\sigma^{MC}_{R_K}$ is dominated by the uncertainties on the signal acceptances in each bin, which are estimated with a relative error of about 2%. A larger signal production, then, is mandatory to reduce the statistical uncertainty on R_K. The current MonteCarlo sample size depends mainly on the recent implementation of the L0 PNN trigger emulator and its subsequent validation. In addition, other aspects of the simulation still need a refinement: for instance, the description of pileup activity in the simulation is missing for some detectors such as the RICH and in L0 calo emulator, therefore a massive production will start only when these missing ingredients are added.

The fit result, shown in Figure 4.3 is:

$$R_K = (2.492 \pm 0.017) \times 10^{-5} \tag{4.6}$$

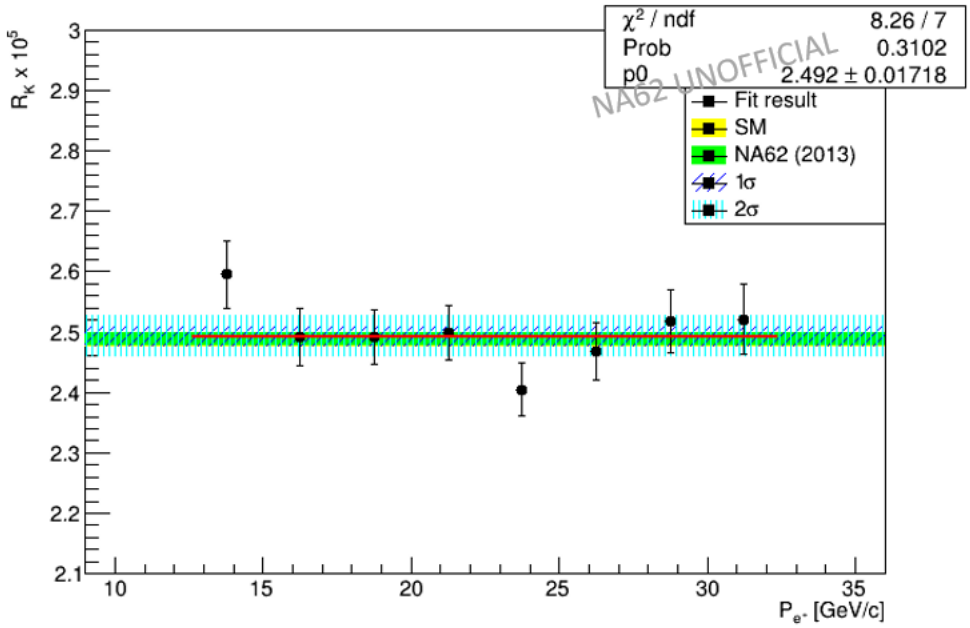

Figure 4.3: Measured values of R_K - multiplied by 10^5 - in bins of positron momentum. The red line is the result of the constant fit. 1σ and 2σ intervals are also shown in figure, as well as NA62 2013 result [27] (green) and the SM expectation [20] (yellow), barely visible due to its smaller uncertainty. **NA62 UNOFFICIAL**

Bin	$N_{K_{e2}}$	$Acc_{K_{e2}}$	$N_{K_{\mu e}}$	$Acc_{K_{\mu e}}$	R_K	$\sigma_{R_K}^{data}$	$\sigma_{R_K}^{MC}$
1	2.6×10^4	3.08 ‰	1.00×10^6	3.08×10^{-6}	2.596	0.016	0.053
2	3.46×10^4	4.04 ‰	1.02×10^6	2.96×10^{-6}	2.492	0.014	0.046
3	4.34×10^4	5.11 ‰	9.37×10^5	2.74×10^{-6}	2.492	0.012	0.043
4	5.56×10^4	6.55 ‰	8.10×10^5	2.38×10^{-6}	2.498	0.011	0.044
5	6.99×10^4	8.52 ‰	6.70×10^5	1.96×10^{-6}	2.404	0.010	0.043
6	8.35×10^4	9.93 ‰	5.40×10^5	1.58×10^{-6}	2.468	0.009	0.047
7	9.54×10^4	1.13 %	4.23×10^5	1.26×10^{-6}	2.518	0.009	0.050
8	1.03×10^5	1.25 %	3.21×10^5	9.85×10^{-7}	2.521	0.009	0.057

Table 4.2: Values obtained from R_K analysis in bins of positron momentum. R_K and the statistical errors have been multiplied by 10^5 **NA62 UNOFFICIAL**

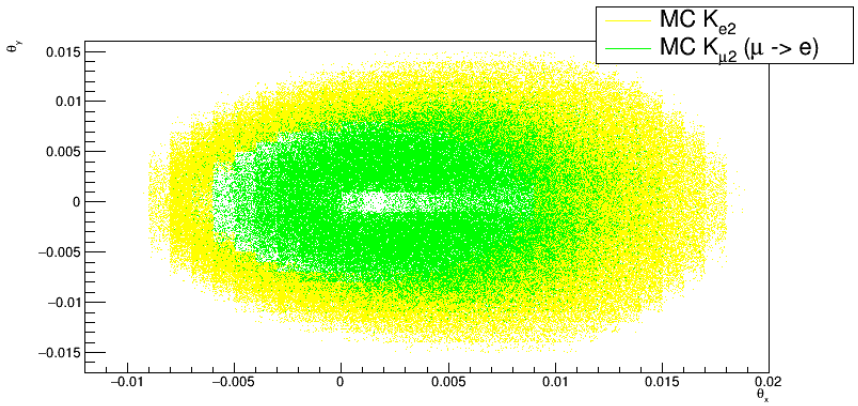

Figure 4.4: Distributions of K_{e2} and $K_{\mu e}$ events in the track slopes plane $(\theta_x; \theta_y)$.

4.3 Systematic uncertainties

4.3.1 MonteCarlo validation

K_{e2} and $K_{\mu e}$ present very different distribution in the track slopes plane $(\theta_x; \theta_y)$, as shown in Figure 4.4; the muon decay in flight makes $K_{\mu e}$ events reach regions of the (θ_x, θ_y) plane not accessible to K_{e2} mode, with an almost zero overlap between the two samples.

Different distributions can lead to different selection efficiencies; this effect, however, is taken into account in the acceptance computation, estimated from MonteCarlo simulation. A validation of the simulation and its comparison with data, then, is necessary in order to spot possible discrepancies and take them into account as systematic effects. Only downstream selection efficiencies have been evaluated, since the upstream part of the selection is exactly the same for both cases; in particular, the efficiency has been factorized into track and PID efficiency:

$$\sigma_{tot} = \sigma_{track} \times \sigma_{PID} \tag{4.7}$$

To avoid any bias, selection efficiencies have been studied using control samples that could be considered representative of the K_{l2} decays: for track selection efficiency a sample of K_{e3} has been used - in order to have a single track decay with positron in the final state - while PID efficiency has been studied with a sample of $K_{2\pi}$ followed by a Dalitz decay of the neutral pion

- i.e $\pi^0 \to e^+e^-\gamma$ - called in the following $K_{2\pi D}$, which offers a clean sample of positrons.

K_{e3} selection This selection, of course, is not based on track information. A minimum bias trigger is used, asking only for the presence of a signal in the NA48-CHOD. A photon pair has to be present in LKr, compatible with a π^0. The average of the photon cluster times, weighted by their energies, is used as a reference time for the following steps of the analysis. An additional cluster has to be selected in the calorimeter, in a $\pm$10 ns time window centered around t_{π^0}. A RICH ring has to be reconstructed, in time with the π^0 within $\pm$2 ns; the ring candidate radius has to be greater than 185 mm, compatible with a Cherenkov signal produced by a positron. A track momentum and direction estimation is obtained in the following way: LKr energy deposition and positron mass, while an extrapolation from the cluster position to the decay vertex - identified by the netural pion - provides a measurement of the track direction. For background purposes, track momentum in the pion mass hypothesis is also computed, then the expected RICH radii for pion and positron are evaluated. Background from $K_{2\pi}$ decays is suppressed asking for a smalller distance between the measured RICH radius and the expected positron radius compared to the ΔR in the pion hypothesis; ΔR_e, however, has not to be greater than 400 mm. In addition, no activity in MUV1 has to be present in a $\pm$20 ns with respect to the π^0 time. Muons are rejected asking for no MUV3 candidates in a $\pm$10 ns around the reference time.

$K_{2\pi D}$ selection $K_{2\pi D}$ offers a clean sample of positrons useful to study PID efficiency in LKr and RICH.

Three tracks have to be present in the event, in a $\pm$20 ns time window around the time of the trigger, and in acceptance of the four STRAW chambers, CHOD, LKr, RICH and MUV1-2-3. Good quality tracks are selected cutting on χ^2_{trk} and the total charge of the three good tracks has to be +1. A least squares fit is used to estimate the kaon decay vertex, which has to be between 110 and 180 m from T10. The vertex time, defined as the average of the track times measured by the spectrometer, is used as reference time for the events. The closest KTAG and GTK candidates with respect to the vertex time are selected: the KTAG candidate has to have signal from at least 4 sectors, while the GTK candidate momentum has to be between 73 and 77 GeV/c. No activity has to be present in LAV, IRC and SAC in a $\pm$10 ns

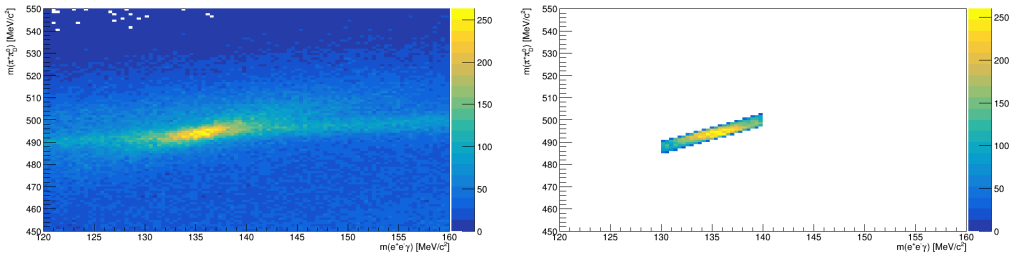

Figure 4.5: Distribution in the $m(e^+e^-\gamma); m(\pi^+\pi^0)$ plane for all the events reaching the final step of $K_{2\pi D}$ selection (left) and for the selected events (right) obtained from 2017 dataset.

with respect to the vertex time, while no more than one photon cluster - i.e. a cluster not spacially associated to any track - is required in LKr in a ± 6 ns with respect to the reference time. Finally, kinematic constraints are used to select signal candidates, based on the reconstructed π^0 and K^+ masses:

$$m_{\pi^0} = \sqrt{(P_{e^+} + P_{e^-} + P_\gamma)^\mu (P_{e^+} + P_{e^-} + P_\gamma)_\mu} \tag{4.8}$$

$$m_{K^+} = \sqrt{(P_\pi + P_{\pi^0})^\mu (P_\pi + P_{\pi^0})_\mu} \tag{4.9}$$

While the electron is univocally identified being the only negatively charged track in the event, there is an ambiguity between the positron and the pion; to overcome this ambiguity, both combinations of the masses are computed, and a discriminant has been build as:

$$discr = \sqrt{(m_{\pi^0} - m_{\pi^0}^{PDG})^2 + (m_{K^+} - m_{K^+}^{PDG})^2} \tag{4.10}$$

where $m_{\pi^0}^{PDG}$ and $m_{K^+}^{PDG}$ are the neutral pion and charged kaon masses obtained from PDG respectively.

A final cut in the $(m_{\pi^0}; m_{K^+})$ plane is applied; Figure 4.5 shows the selected region.

Results The STRAW efficiency curves obtained from K_{e3} control sample is reported in Figure 4.6 and a clear discrepancy between data and Monte-Carlo can be observed. The cause of this discrepancy is the requirements on STRAW-RICH association, for essentially two reasons: the first reason is that the requirement on the $\Delta_{Ringcentre}$ makes the efficiency curves to saturate at

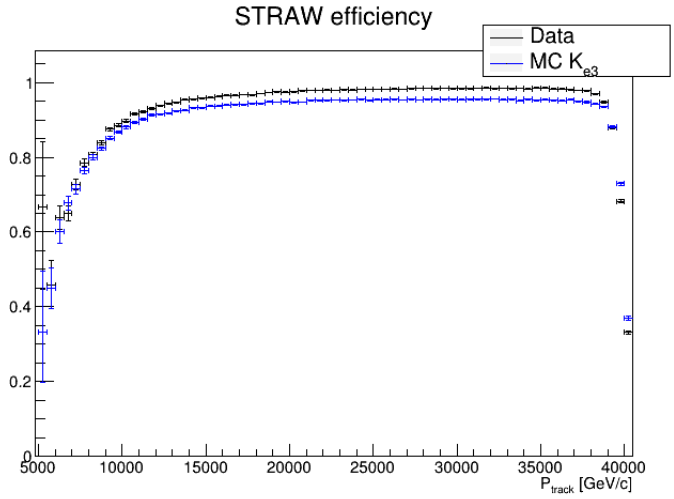

Figure 4.6: STRAW efficiency as a function of the track momentum measured with K_{e3} control sample. The track selection conditions are those described in Chapter 3

higher momenta and the second one is the lack of pileup activity in the RICH for MonteCarlo, which decreases the downstream selection efficiency. As a comparison, Figure 4.7 shows the pure STRAW reconstruction efficiencies, not looking at the STRAW-RICH association: in this case, a discrepancy at the level of permille is observed. From a study of the efficiencies in the $(\theta_x; \theta_y)$, the effect results to be more relevant at low track momentum. As an example, the ratio between STRAW efficiency in data over the efficiency estimated by MonteCarlo in the slopes plane for two bins of momentum is reported in Figure 4.8: while at higher momentum the distribution can be considered uniform, affecting K_{e2} and $K_{\mu e}$ distributions in the same way, at lower momentum the ratio $\epsilon_{data}/\epsilon_{MC}$ have sizable variation, which are translated into a systematic uncertainty due to the low momentum cut and estimated in the next sections.

Particle identification efficiencies, instead, are reported in Figures 4.10 and 4.9 and do not show a statistically relevant difference.

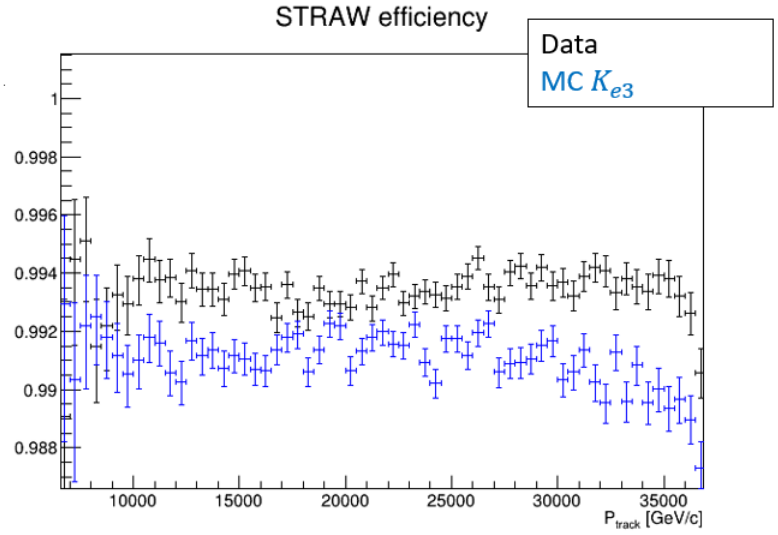

Figure 4.7: STRAW efficiency as a function of the track momentum measured with K_{e3} control sample. The track selection conditions are those described in Chapter 3 without the requirements on RICH ring

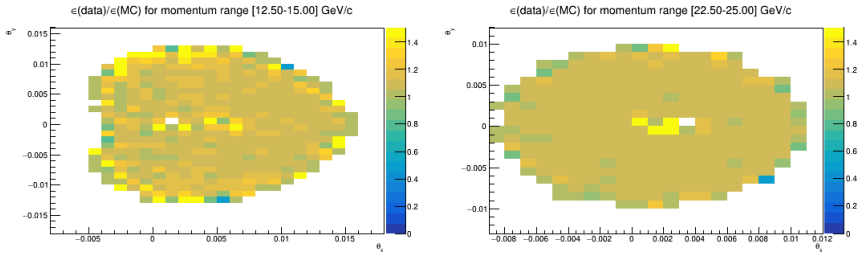

Figure 4.8: Ratio $\epsilon_{data}/\epsilon_{MC}$ of the STRAW efficiency for two bins of positron momentum.

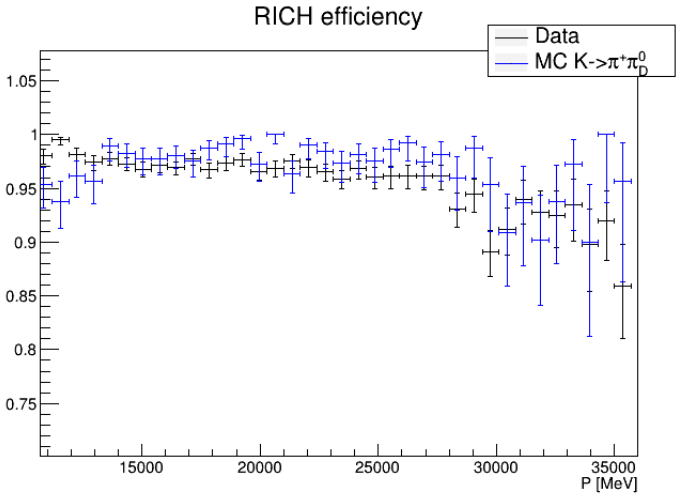

Figure 4.9: RICH particle identification efficiency as a function of the positron momentum measured with $K_{2\pi D}$ control sample.

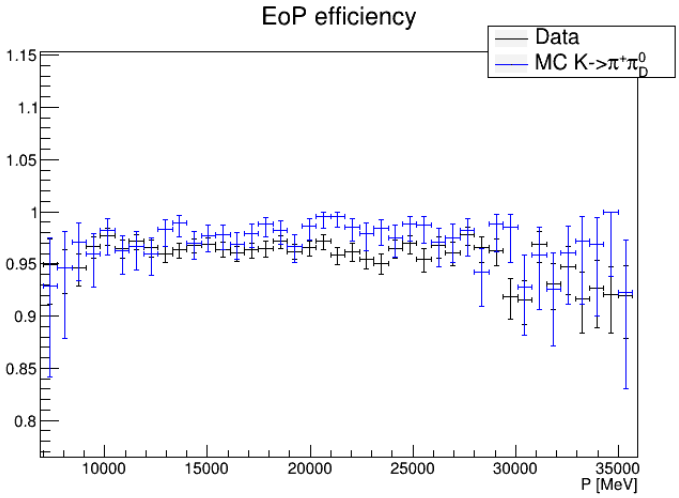

Figure 4.10: E/p particle identification efficiency as a function of the positron momentum measured with $K_{2\pi D}$ control sample.

4.3.2 Effect of L0 trigger

The effect of the L0 PNN trigger mask on R_K measurement has been evaluated performing the analysis enabling and disabling the L0 trigger emulators for MonteCarlo simulation. In this way, the observed discrepancy between the two central values of R_K can be considered as the maximal effect of the trigger on the measurement. Without using the L0 trigger emulator, the measured value of R_K is

$$R_{K\,NoL0emu} = (2.494 \pm 0.017_{stat}) \times 10^{-5} \tag{4.11}$$

which corresponds to a difference of $\Delta R_K = 0.002 \times 10^{-5}$ with respect to the result reported in Eq. 4.6. A systematic uncertainty, then, can be quantified dividing ΔR_K by $\sqrt{12}$, namely the standard deviation of the uniform distribution:

$$\sigma^{syst}_{Trig} \times 10^5 = 0.0006 \tag{4.12}$$

This value provides a strong confirmation on the validity of the experimental strategy, as the relative contribution to R_K is 2×10^{-4}. New MonteCarlo production will allow to test also the systematic effect due to L1 algorithms, since they were not implemented yet. The expected systematic uncertainty due to PNN trigger, however, is one order of magnitude smaller than the current experimental precision.

4.3.3 Systematic uncertainties due to analysis cuts

The effect of the cuts adopted for the event selection as systematic uncertainties for the measurement has been studied evaluating the differences of R_K measurement varying each cut. In the following figures, ΔR_K as a function of the analysis cuts is reported; the error quoted on the differences is the "uncorrelated error", i.e. the uncertainty on the difference which takes into account the overlaps between the samples due to the change of a cut. The uncorrelated error between two configurations, A and B, can be written as[41]:

$$\sigma_{uncorr} = \sqrt{|\sigma^2_A - \sigma^2_B|} \tag{4.13}$$

In order to establish if one cut gives a systematic uncertainty on the measurement, the following procedure has been adopted. A constant linear fit is performed on each plot: if the fit probability is above a confidence level of

5 % then the observed difference is considered compatible with a statistical fluctuation; otherwise, the systematic uncertainty due to a specific cut is estimated as the standard deviation of the ΔR_K distribution corresponding to that cut.

The relevant systematic uncertainties are reported in Table 4.3.

The most relevant contribution is due to the lower cut on the track momentum, which is due to the not perfect implementation of STRAW-RICH association; then the definition of the K_{e2} region also contribute to the systematic uncertainty because of the discrepancies in the kaon momentum measured by GTK. A new improved procedure of GTK stations alignment, which is essential for a correct momentum measurement, is under development and will reduce this contribution. Maximum bremsstrahlung photon energy also gives a sizeable systematic effect and in this case the origin is the lack of pileup activity for L0calo emulator, which is not able to reproduce perfectly the real trigger. Finally, the upper cut on E/p gives a contribution due to the different shape of the right tail of E/p peak, as can be seen in Figure 4.23. A larger MonteCarlo sample will help also in this case since it will allow to set a larger upper cut.

The final result is, then

$$R_K = (2.492 \pm 0.017_{stat} \pm 0.009_{syst}) \times 10^{-5} \tag{4.14}$$

which is in agreement with the measured value and with the SM expectation. As mentioned before, the statistical uncertainty is dominated by the MonteCarlo samples size.

Source	$\epsilon^{syst} \times 10^5$
Min Z_{vtx}	-
Max Z_{vtx}	-
Min P_K	-
Max P_K	-
Min E/p	-
Max E/p	0.002
Max E_γ	0.002
Min P_{e^+}	0.008
Max P_{e^+}	-
CDA	-
$K_{e2}region$	0.003
$K_{\mu e}region$	-
Total	0.009

Table 4.3: Contributions to the systematic uncertainties due to analysis cuts.

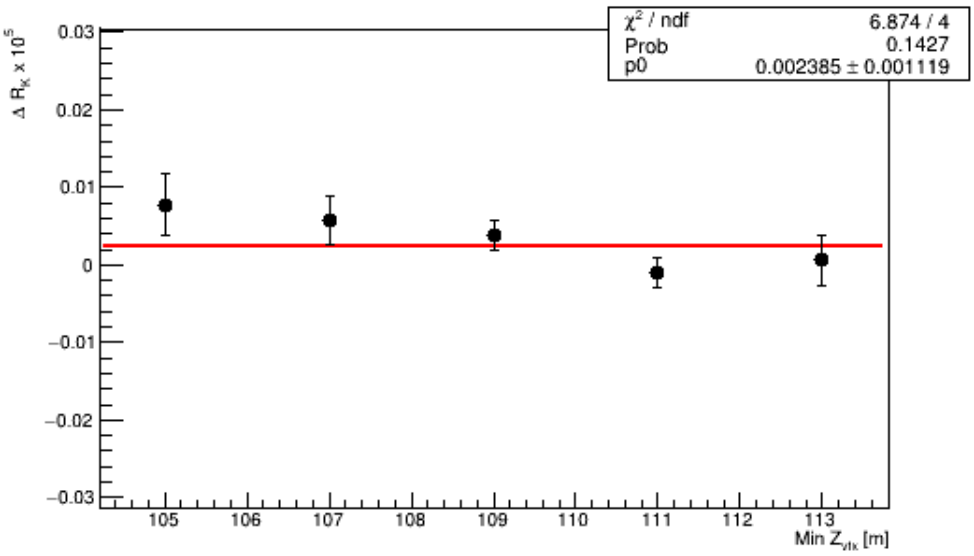

Figure 4.11: ΔR_K as a function on the lower cut on the Z coordinate of the decay vertex.

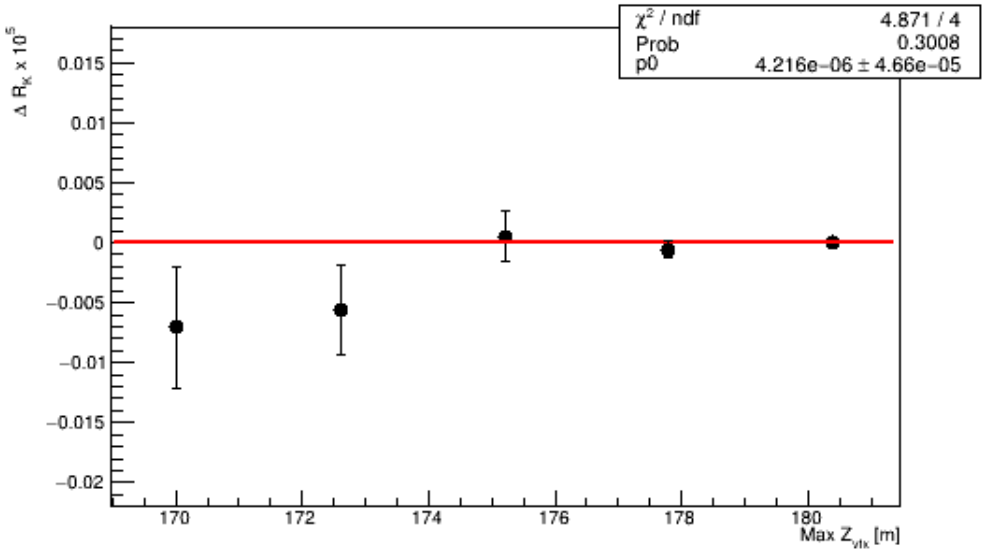

Figure 4.12: ΔR_K as a function on the upper cut on the Z coordinate of the decay vertex.

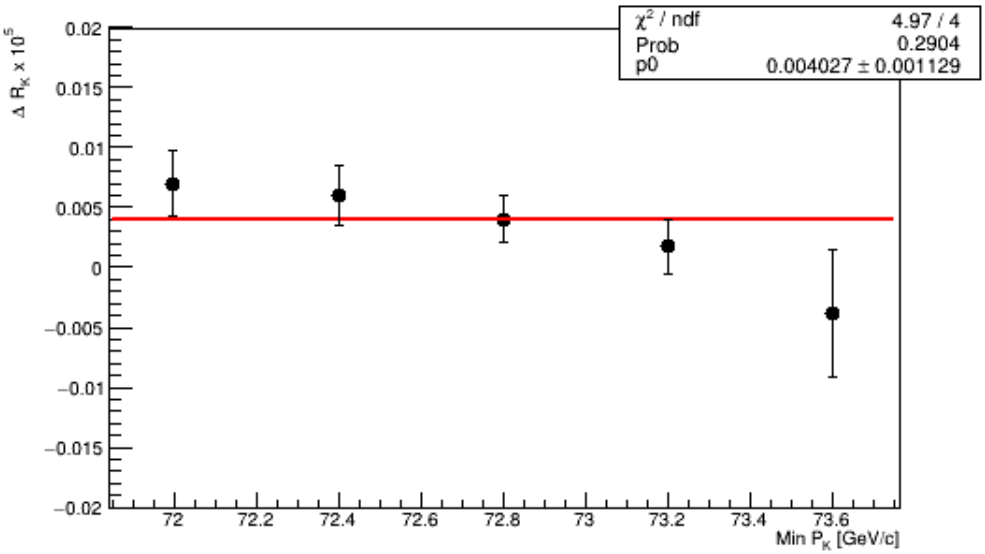

Figure 4.13: ΔR_K as a function on the lower cut on the kaon momentum.

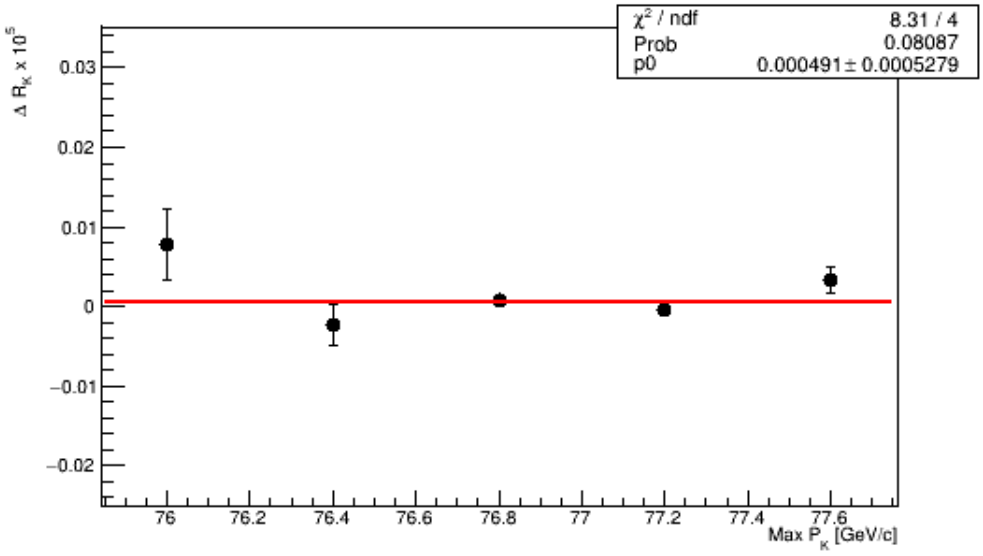

Figure 4.14: ΔR_K as a function on the upper cut on the kaon momentum.

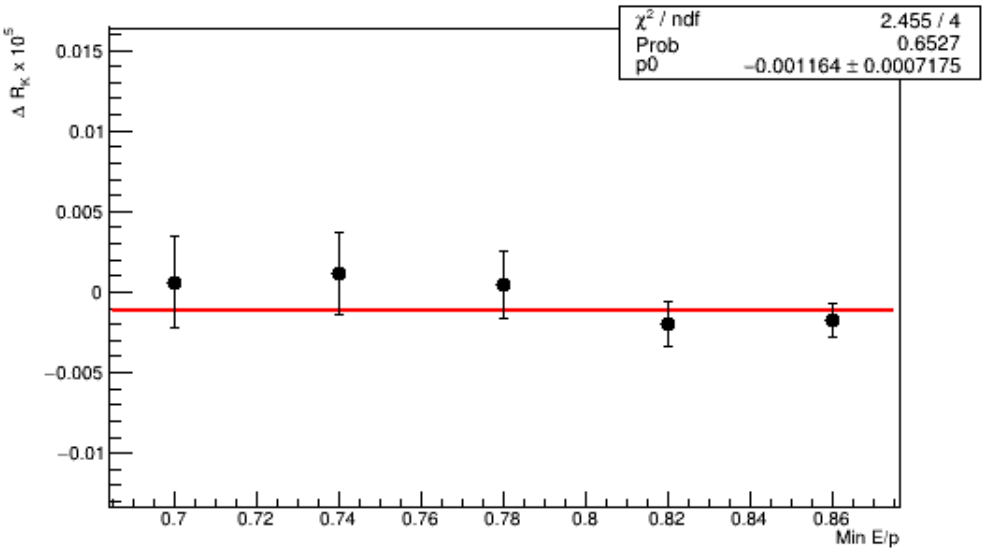

Figure 4.15: ΔR_K as a function on the lower cut on the E/p ratio.

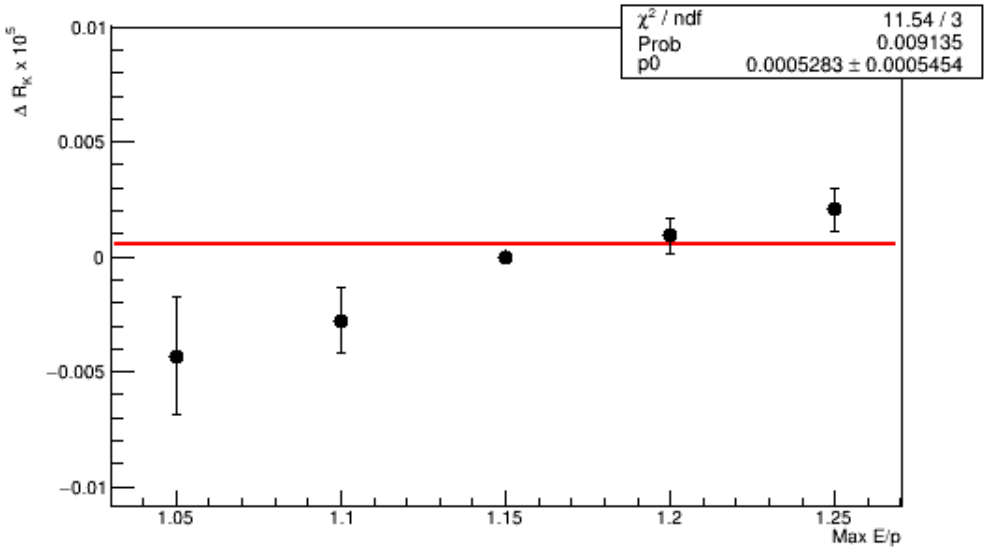

Figure 4.16: ΔR_K as a function on the upper cut on the E/p ratio.

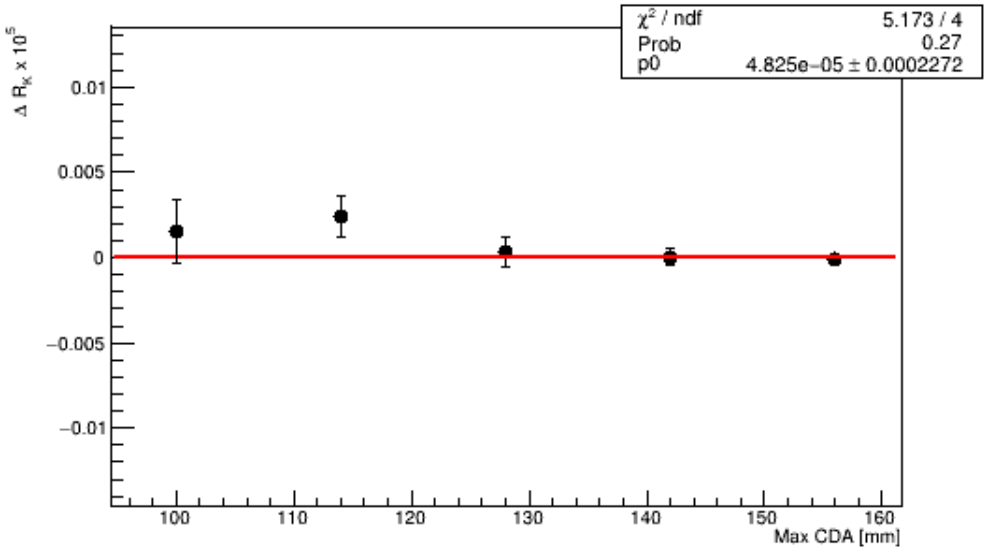

Figure 4.17: ΔR_K as a function on the upper cut on the CDA.

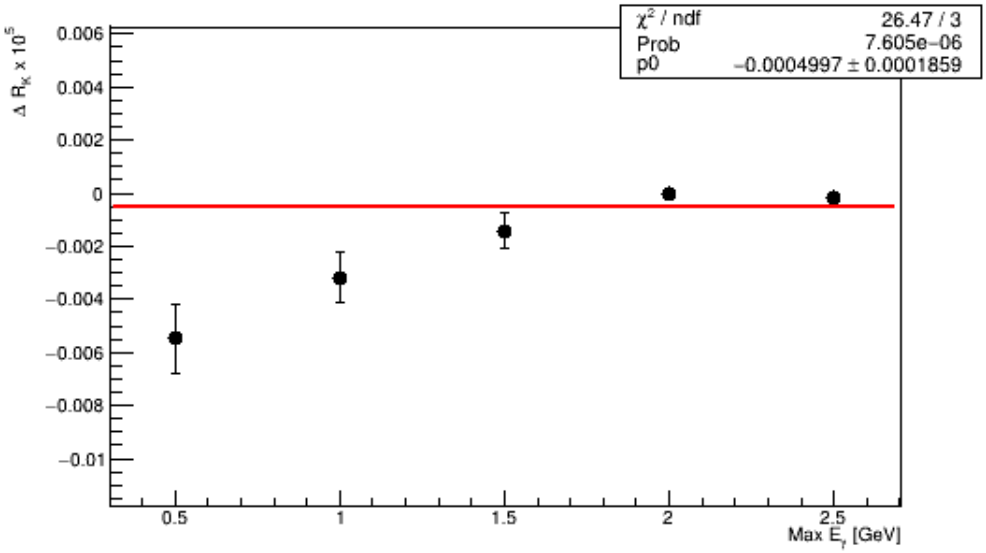

Figure 4.18: ΔR_K as a function on the upper cut on the bremsstrahlung photon energy.

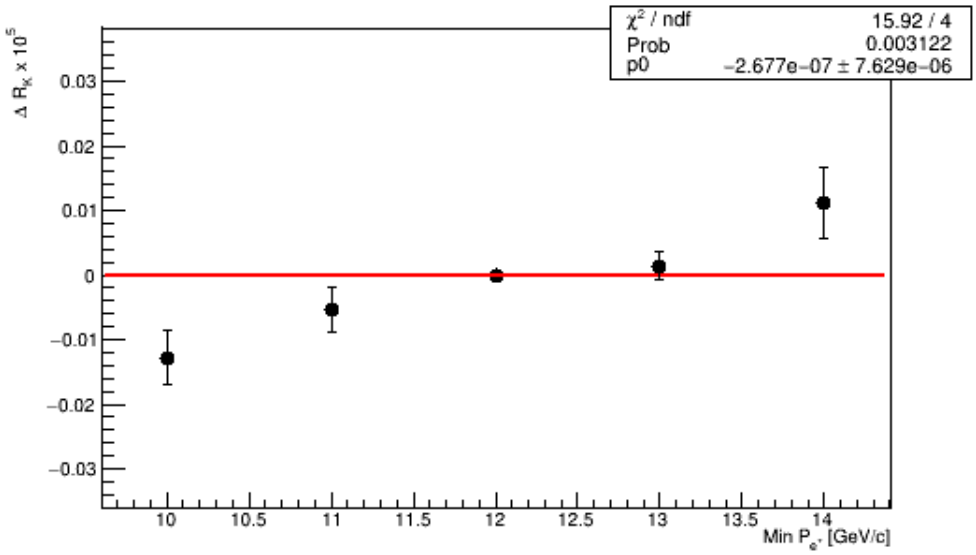

Figure 4.19: ΔR_K as a function on the lower cut on the positron momentum.

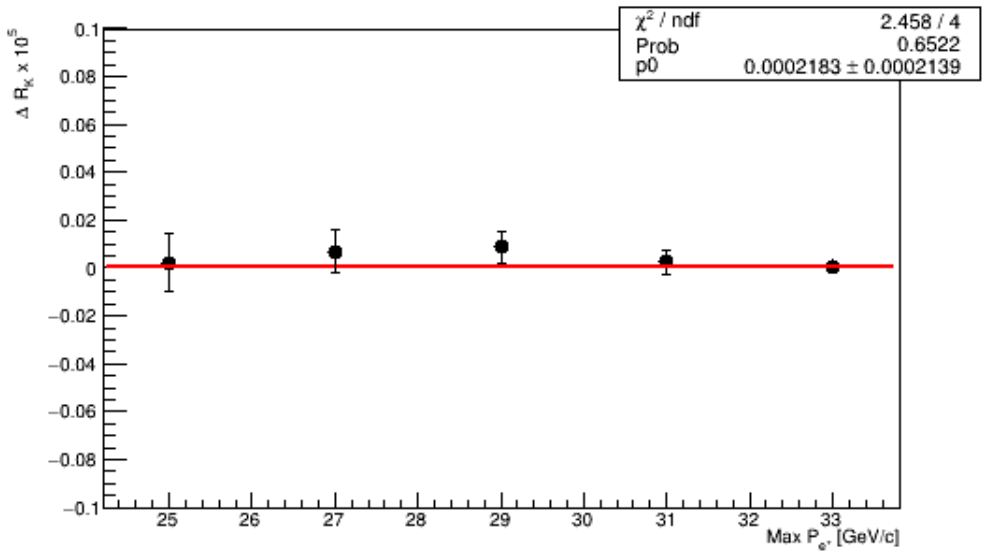

Figure 4.20: ΔR_K as a function on the upper cut on the positron momentum.

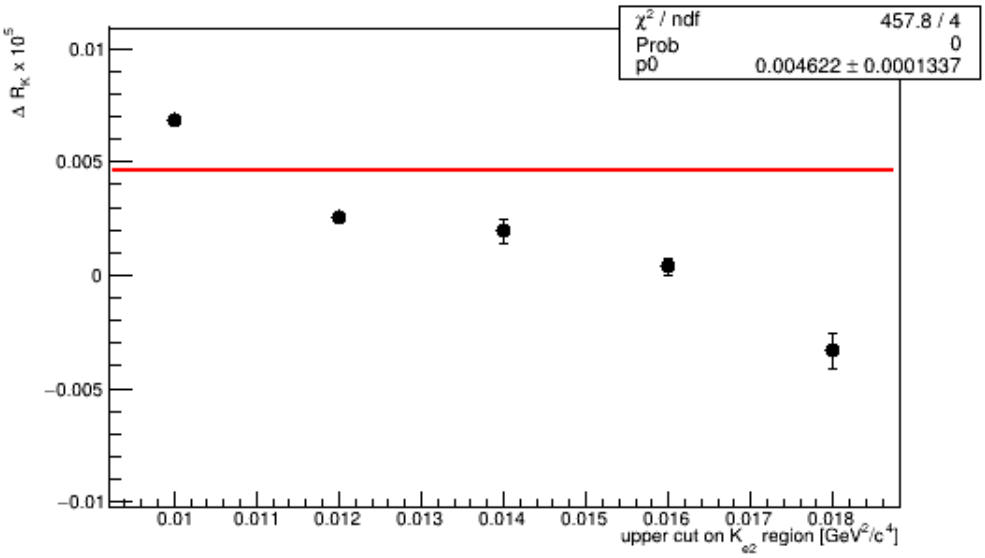

Figure 4.21: ΔR_K as a function on the upper cut on the K_{e2} region.

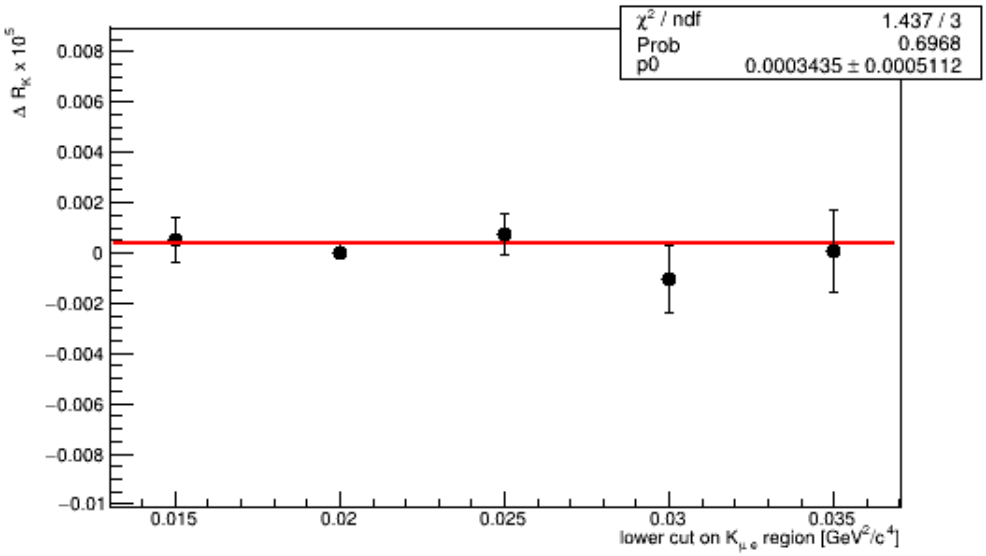

Figure 4.22: ΔR_K as a function on the lower cut on the $K_{\mu e}$ region.

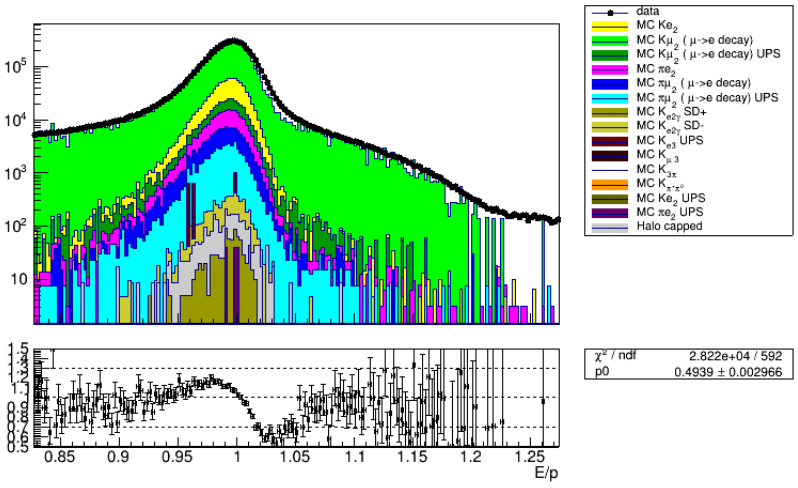

Figure 4.23: E/p distriution. A discrepancy between data and MonteCarlo is clearly visible in the righ tail of the peak.

Conclusions

The goal of this work was to present a novel technique to perform a competitive measurement of R_K, with the possibility to improve the experimental precision. A common selection has been developed, using the same trigger stream for K_{e2} and $K_{\mu 2}$ and extracting the latter from events with muon decays in flight in the decay region. Following this approach, the trigger mask with the lowest downscale was used for this analysis, and most of the systematic uncertainties due to the trigger were canceled in the definition of R_K. Thanks to the high intensity beam of NA62 experiment, a more than three times greater sample compared to previous R_K measurements has been collected analyzing only a subset of 2017 dataset. From the total 2017+2018 periods, a O(10) larger sample is expected. The most relevant background for K_{e2} is represented by the tails of the $K_{\mu e}$ distribution, with almost negligible additional contributions. Background in $K_{\mu e}$ region, on the other hand, is dominated by upstream $K_{\mu e}$ and beam pion decays.

The statistical uncertainty is currently dominated by the uncertainties on the expected background events and mostly on the uncertainty on the signal acceptances. The limited MonteCarlo size is due to the recent developments of the L0 trigger emulators; also other improvements on the simulation, such as the description of pileup activity in the detectors, are ongoing. After the validation of the new refinements of the simulation, a larger production will be started.

The systematic effect of the PNN trigger on the measurement, as expected, is $O(10^{-4})$ which is one order of magnitude smaller than the current experimental precision. NA62 hermetic photon veto system is also able to reject $K_{e2\gamma}$, K_{e3} and muon halo background, making their contributions to the systematic uncertainties negligible. A O(4‰) total systematic uncertainty has been obtained, due to the analysis cuts on E/p, the maximum energy of the IB photons and on the definition of K_{e2} region. Concerning

the uncertainty due to E/p distribution, a cut on the maximum value of E/p is necessary only because of the lack of MonteCarlo events, therefore larger simulation samples will allow to avoid the cut and to neglect its systematic effect. The IB photon energy distribution shows a discrepancy between data and MonteCarlo due to a not perfect description of L0 calo emulator: improvements on this side are foreseen to reduce the systematic uncertainty. K_{e2} region is defined by the squared missing mass between the kaon and the positron and its systematic uncertainty is likely due to the different distribution between data and MonteCarlo of the momentum measured by the GTK. A new procedure to perform GTK station alignment - which is essential to properly measure beam particles momenta - is currently under development and a reduced systematic uncertainty is expected.

The result obtained for R_K is

$$R_K = (2.492 \pm 0.017_{stat} \pm 0.009_{syst}) \times 10^{-5} \tag{4.15}$$

which is in agreement with the most precise experimental value [27] and with the SM expectation [20].

Appendix A

Optimization of π^0 rejection and random veto for $K^+ \to \pi^+\nu\bar{\nu}$ analysis

A.1 Introduction

One of the main backgrounds for the measurement of the BR of $K^+ \to \pi^+\nu\bar{\nu}$ is $K^+ \to \pi^+\pi^0(\gamma)$ ($K_{2\pi}$). The number of these background events entering the signal region is given by two numbers: the fraction of events that has the missing mass inside the signal regions because of resolution effects (" kinematic tails") and the fraction of $K_{2\pi}$ events which pass all the selection compared to the total number of events in the normalization sample; the latter is called π^0 rejection. Since the kinematic tail are of the order of 1‰[39], in order to keep $K_{2\pi}$ background at the level of 10^{-11}, the π^0 rejection factor should not exceed $O(10^{-8})$.

To achieve this level of suppression, any activity in time in LKr, LAV, IRC and SAC must be discarded. In addition, other criteria are used to suppress extra activity in time between LKr and NA48-CHOD, LKr and CHOD and NA48-CHOD and CHOD ("multiplicity cuts" in the following). Finally, events with partially reconstructed tracks in the spectrometer ("segments") are discarded as well.

Nevertheless, all the criteria mentioned above have the effect to discard signal events because of random activity in the detectors. This effect ("random veto") is quantified using a control-triggered $K_{\mu 2}$ sample: the fraction

of events which are not rejected with respect to the total sample is defined as "random veto efficiency", labelled as ϵ_{RV}; it is straightforward that $1 - \epsilon_{RV}$ represent, on the contrary, the fraction of events which are randomly vetoed. By definition, ϵ_{RV} strongly depends on the instantaneous beam intensity, decreasing at higher intensity, as reported in Figure A.1[39].

The π^0 rejection is computed via the following formula:

$$\pi^0_{rej} = \frac{N^{PNN}_{\pi\pi}}{N^{CTRL}_{\pi\pi} \cdot D \cdot \epsilon_{trigger} \cdot \epsilon_{RV}} \tag{A.1}$$

Here, $N^{PNN}_{\pi\pi}$ and $N^{CTRL}_{\pi\pi}$ represent the number of events in $K_{2\pi}$ region collected by PNN and control trigger streams respectively, $D = 400$ is the downscale factor between the two streams and $\epsilon_{trigger}$ is the PNN trigger efficiency. This work aims to optimize the working point between π^0 rejection

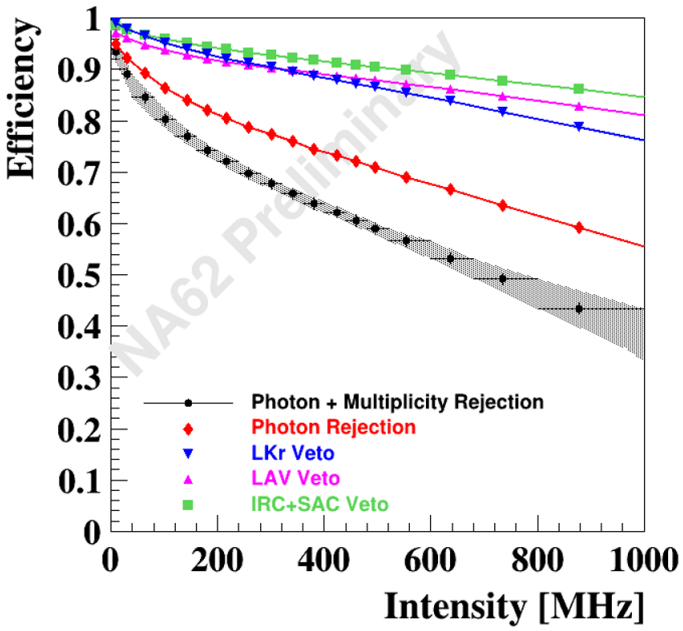

Figure A.1: Distribution of ϵ_{RV} as a function of the instantaneous beam intensity.

factor and random veto. It is focused on NA62 Liquid Krypton calorimeter (LKr) because of its central role in the photon veto system thanks to is high efficiency and acceptance.

Energy	Time cut
$E < 1$ GeV	$\|\Delta t\| < 5$ ns
$1 < E < 2$ GeV	$\|\Delta t\| < 5 \cdot \sigma_t$
$2 < E < 15$ GeV	$\|\Delta t\| < 15 \cdot \sigma_t$
$E > 15$ GeV	$\|\Delta t\| < 70 \cdot \sigma_t$
$E > 2$ GeV	$\|\Delta t \pm 25\text{ns}\| < 5\text{ns}$

Table A.1: Standard LKr time matching criteria

A.2 LKr

The time difference between LKr clusters not associated to the track and pion time as a function of energy deposits in the calorimeter for events collected in 2016 is reported in Figure A.2. Despite a core resolution smaller than 1 ns, non-gaussian tails are visible in the Δt distribution, as well as additional peaks around ± 25 ns. The origin of these peaks was a CREAM firmware problem ("jitter"), appearing many times during the data taking.

Table A.1 summarizes the time windows used in 2016 analysis, depending on the cluster energy. The parameter σ_t is the LKr time resolution, given by:

$$\sigma_t(ns) = 0.53 + 1.53/E(GeV) + 0.233/\sqrt{(E(GeV))}. \quad \text{(A.2)}$$

For high energy clusters, σ_t is rougly constant and its value is around ~ 600 ps, which means that no clusters with energies greater than 15 GeV must be present in a ± 42 ns time window. A rejection factor of $\sim 3 \times 10^{-8}$ was achieved with total random veto losses around 25%; based on this value, the expected total random veto for 2017 dataset is about 40%.

In the following sections the possible improvements related to LKr veto will be addressed, focusing on the treatment of non gaussian tails of Δt distribution and additional time windows.

A.2.1 In time resolution

The LKr reconstruction is based on two different algorithms, usually called "standard" and "auxiliary" reconstructions. Standard reconstruction is based on NA48 FORTRAN routines. Hits are clusterized around a "seed", defined as a local energy maximum in a 3x3 cells square; if a dead cell is present there, the 5x5 cells square is considered. Cluster position is given by the

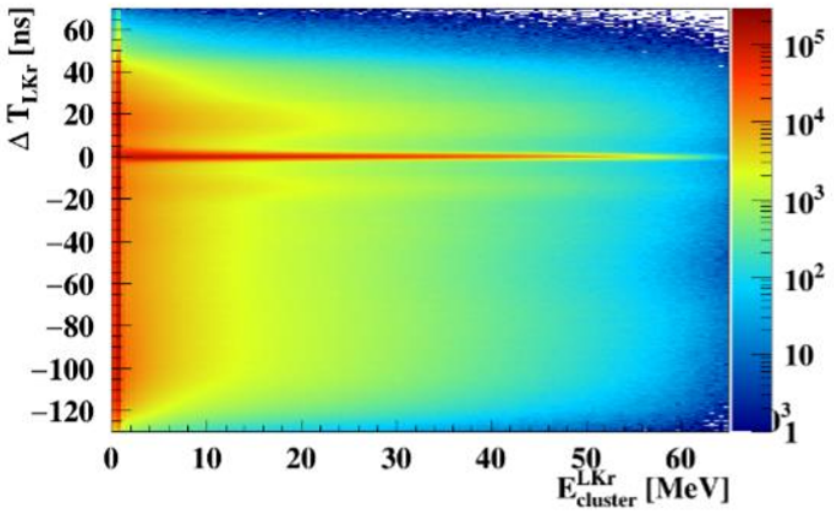

Figure A.2: Distribution of the time difference between LKr clusters and CHOD time associated to the π versus cluster energy for 2016A dataset. Only clusters not belonging to the π candidate are plotted

barycentre of energy deposits in the 3x3 cells located around the seed. Hit energy and time are obtained using the digital filter method starting from the pulse shapes, sampled in 8 time windows, 25 ns wide. The time of the cluster is set to the time of the seed. Auxiliary reconstruction uses an opposite approach: close hits are clusterized, without asking for a seed, in a circle with radius equal to 10 cells; the position of the cluster is gives by the weighted average of the hits position and its time is provided by the time of the seed as in the standard reconstruction; the efficiency of this algorithm is higher at low energies than the standard routine, while it gives worse results at high energy.

Using the cuts reported in Table A.1 and the latest version of PNN selection, one obtains for 2017 dataset:

$$\pi^0_{rej} = (1.87 \pm 0.07) \times 10^{-8} \tag{A.3}$$

$$\epsilon_{RVLKr} = 0.881 \pm 0.001 \tag{A.4}$$

$$\epsilon_{RV} = 0.619 \pm 0.001 \tag{A.5}$$

where ϵ_{RVLKr} represent the random veto efficiency due to LKr only; these values have to be intended as a reference to the optimization process.

A $K_{\mu 2}$ selection has been used to evaluate the contribution of each time window on the total LKr random veto and the results are reported in Figure A.3.

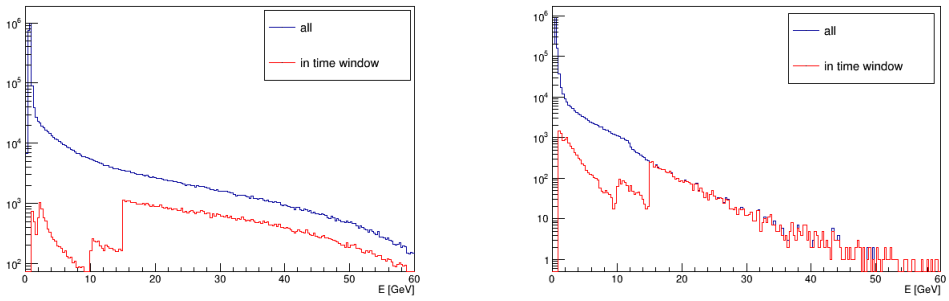

Figure A.3: Left: Energy distribution for all clusters (in blue) and for in-time clusters (red) in a $K_{\mu 2}$ sample obtained by standard reconstruction. Right: same plots for cluster reconstructed via auxiliary algorithm. The plots show clearly that the main contribution to LKr random veto come from the window for clusters with energy greater than 15 GeV, which has the biggest integral of the in-time distribution.

Reducing the cut for $E > 15$ GeV from $70\sigma_t$, i.e. 42 ns, to $15\sigma_t$ (10 ns) the π^0 rejection factor become one order of magnitute greater, reaching $O(10^{-7})$ as shown in Figure A.4.

The characteristics of the accepted events in the $K_{2\pi}$ region decreasing this cut allowed a clear understanding of the problem: the cause of these clearly non gaussian tails of Δt distribution is the cluster merging between a triggered event and accidental activity before or after it.

As an example, Figure A.5 shows the energy and the time distribution of a PNN triggered event which is not rejected using $15\sigma_t$ as threshold. In the event, 5 clusters can be easily identified. The track that triggered the event corresponds to the top cluster, while the others are photons. The topology of the timing plot indicates that the event is the result of two $K^+ \to \pi^+\pi^0$ decays, roughly at 60 ns of time difference, with two photon clusters merged (bottom cluster).

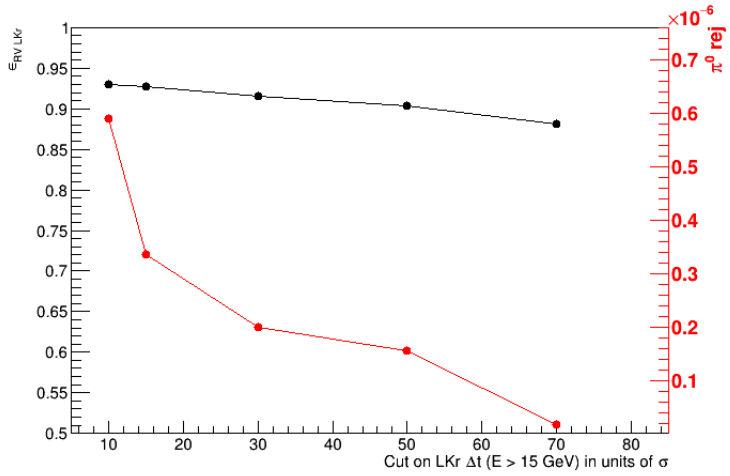

Figure A.4: ϵ_{RVLKr} (black) and π^0 rejection (red) as a function of the cut on the Δt for clusters with energies greater than 15 GeV in units of σ_{LKr}

This event is not rejected by LKr veto criteria because of the combination of two issues in the current reconstruction scheme. The cluster to the left of the beam hole, which is in time with the track, is not reconstructed by the standard reconstruction because its seed does not satisfy the local maximum condition and the auxiliary reconstruction associates all these hits with the bottom cluster because of few cells between them that act as a bridge. The seed of the cluster is in the region where the two populations of the bottom cluster are merged and its time is ~ 11 ns away from the track, which makes it outside the $15\sigma_t$ window.

These events with mis-reconstructed cluster times can be recovered cutting on the total energy, not associated to the track, in time with the trigger: in the example plot, the right part of the bottom cluster has indeed several GeV in few ns with respect to the track. The additional condition depends on two parameters, namely the energy threshold and the time window between LKr hits and the track. The choice made in the following is to ask for more than 5 GeV deposited in ± 5 ns with respect to the reference time.

Figure A.6 shows the values of ϵ_{RVLKr} and π^0 rejection as a function of the cut on the Δt for clusters with energies greater than 15 GeV in units of σ_{LKr} after the cut on the in-time energy is applied. In this configuration, reducing the cut on high energy clusters down to 10 σ will keep the π^0 rejection at the

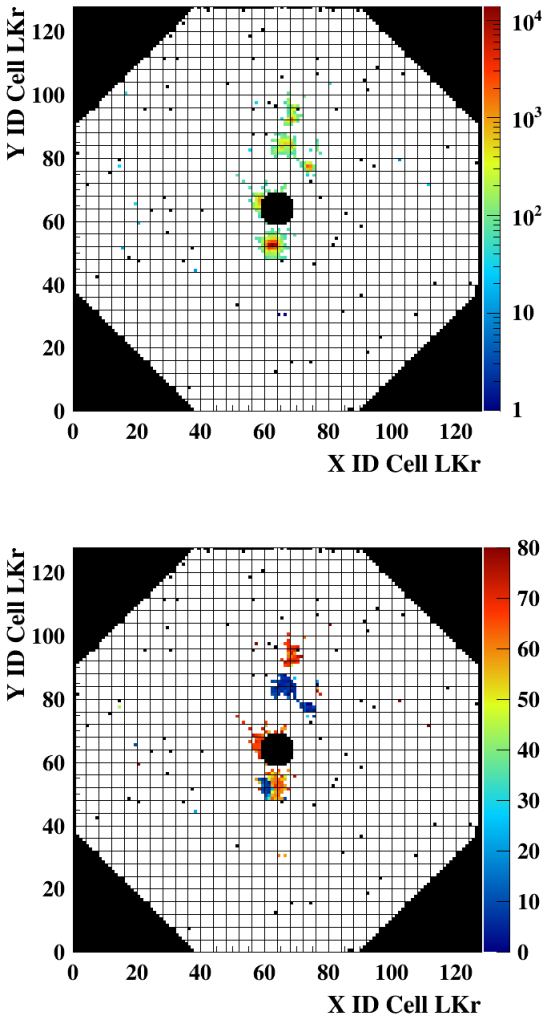

Figure A.5: Energy (top, in MeV) and time (bottom, in ns) distribution of LKr hits for an event in which a cluster merging is present

level of 10^{-8}, with a slightly higher value with respect to (A.3) . LKr random veto efficiency at 10 σ is $\epsilon_{RV\,LKr} = 0.916(1)$, which means that the random losses by LKr would be reduced by a quarter in relative terms. On the other hand, the absolute gain in terms of total RV efficiency is not as much as the LKr random veto because of a correlation between the ΣE conditions and

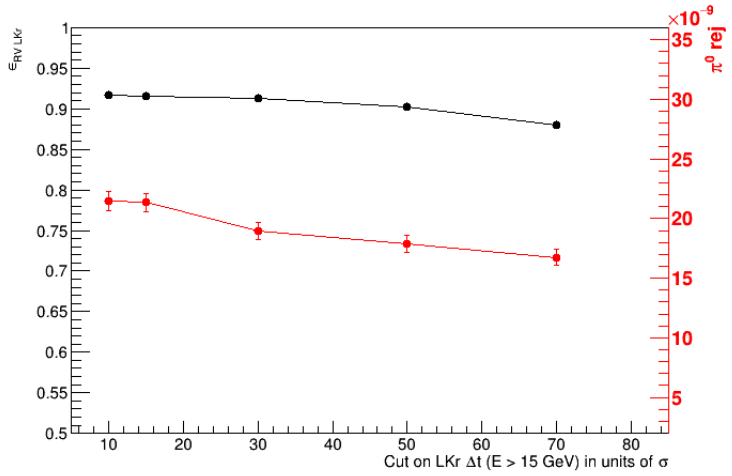

Figure A.6: $\epsilon_{RV\,LKr}$ (black) and π^0 rejection (red) as a function of the cut on the Δt for clusters with energies greater than 15 GeV in units of σ_{LKr} when the cut on the in-time energy is applied

the multiplicity criteria, which actually increases ϵ_{RV} only by 2% absolute, as shown in Figure A.7.

Another possibility would be to use in-time energy cut together with the standard cut in order to obtaining a better π^0 rejection without decreasing ϵ_{RV}. In this configuration the results are:

$$\pi^0_{rej} = (1.67 \pm 0.07) \times 10^{-8} \tag{A.6}$$

$$\epsilon_{RV} = 0.619 \pm 0.001 \tag{A.7}$$

A.2.2 Jitter treatment

In case of jitters, all or a part of the hits in one CREAM are out of time by a multiple of 25 ns: the former can be simply corrected, after the detection, subtracting the offset to the LKr hits belonging to that CREAM, while the latter case has to be treated with an additional time window centered around the time of the jitter. Examples of these jitters are reported in Figure A.8. An automatic procedure to detect jitters has been implemented in NA62 Reconstruction, running burst by burst; it looks for "cluster cores", i.e. a group of 3x3 cells with enough energy deposits, at the edges of a CREAM. Energy

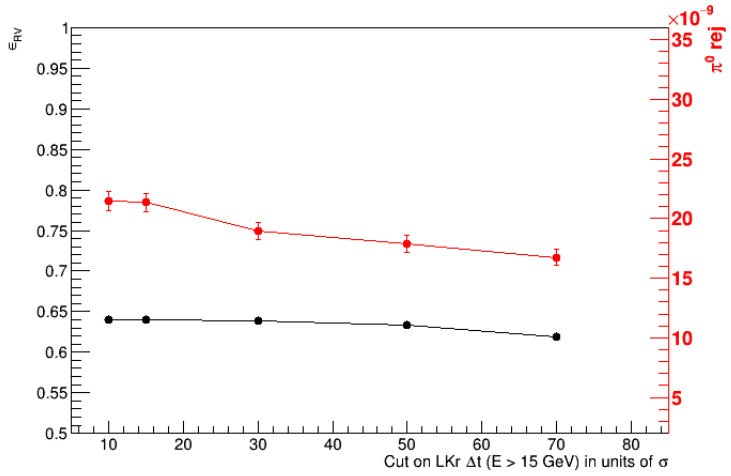

Figure A.7: Total random veto efficiency ϵ_{RV} (black) and π^0 rejection (red) as a function of the cut on the Δt for clusters with energies greater than 15 GeV in units of σ_{LKr} when the cut on the in-time energy is applied

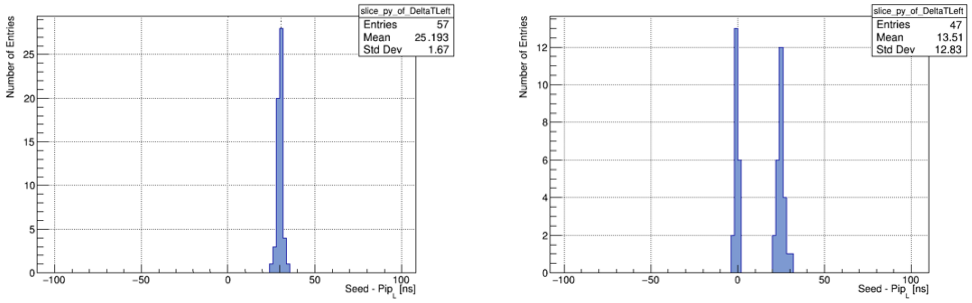

Figure A.8: Time difference between two adiacent CREAMs in case of full jitters (left) or "50-50" jitters (right)

deposits and their times are obtained before proper LKr reconstruction fitting the samplings ("digi") with a parabolic function. The central cell of the core (seed) has to be at least 400 MeV, while the surrounding hits ("pips") have to be more than 100 MeV. For each cluster core, one can compute the variables:

$$\Delta t_{ij} = t_{SEED} - t_{PIP_{ij}} \qquad i,j = 0,1,2 \quad i \cdot j \neq 1 \tag{A.8}$$

The indices i and j identify one of the 8 cells surrounding the seed, defining the top left pip as $(i, j) = (0, 0)$ and the seed position as (1,1). Depending on the seed position, part of Δt_{ij} are in the same CREAM of the seed while the remaining part measures the time difference between two adiacent CREAMs. Looping on all the cluster cores with the seed in a CREAM, one obtains 8 distributions of time difference between that CREAM and the neighbours: in case of jitters, these distribution will not be centered at zero, as reported in Figure A.9.

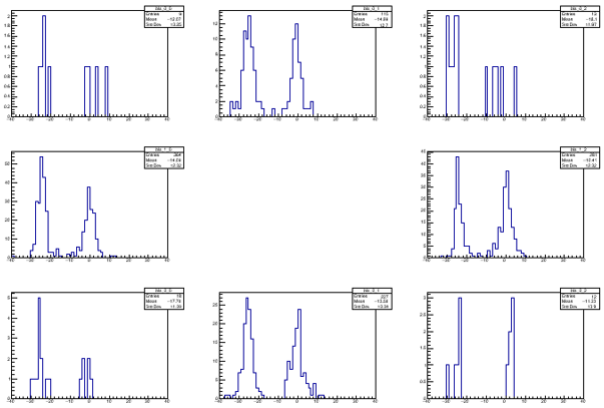

Figure A.9: Example of time difference distributions between one CREAM and the 8 neighbours in case of jitter.

Jitters are gathered over 2017 dataset in two subperiods, with sporadic runs affected by the issue outside them (Figure A.10). Since their origin was a board misbehaviour, jitter were accidentally fixed by reloading CREAM firmware to solve other problems appeared during data taking.

Jitter detection have been implemented in the NA62 framework; once detected, full jitters are corrected in LKr reconstruction by subtracting an offset equal to t_{jitt} to all the hits in the affected CREAMs, while "50-50" jitters are handled by an appropriate class, which set additional time windows around the time of a jitter, if present in the current burst, only for hits belonging to problematic CREAMs. This treatment reduces the contribution to random veto coming from the extra windows by two order of magnitudes.

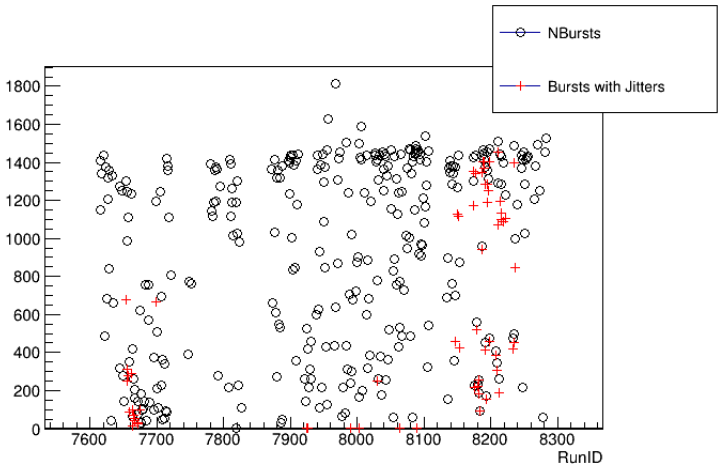

Figure A.10: Distribution of numer of burst with jitters (red crosses) compared to the total number of bursts (black circles) in 2017 dataset. The black circles are the number of bursts in each run while the red crosses refer to the number of bursts with jitters.

A.3 Results and conclusions

In this work, the causes of long non gaussian tails and additional peaks in the LKr time distribution have been identified. An optimization of LKr time matching criteria has been addressed: a better π^0 rejection factor has been achieved without increasing the random veto but the correlation between the additional condition used for the optimization and the multiplicity rejection cuts prevented to achieve bigger improvements. Jitters treatment has been also addressed, allowing users to check LKr activity in time also in presence of this firmware misbehaviour.

Future developments of this work could lead to further reduction of LKr random veto but modifications are needed at the reconstruction level: for instance, using a different algorithm to fit the time of the clusters in case of merged events would keep π^0 rejection at the level of (A.3) without introducing correlation with other rejection criteria.

Bibliography

[1] S. Weinberg. "A model of leptons". In: *Physical Review Letters* 19.21 (1967), pp. 1264–1266. ISSN: 00319007. DOI: 10.1103/PhysRevLett.19.1264.

[2] S. L. Glashow. "Partial-symmetries of weak interactions". In: *Nuclear Physics* 22.4 (Feb. 1961), pp. 579–588. ISSN: 0029-5582. DOI: 10.1016/0029-5582(61)90469-2.

[3] A. Salam et al. "Electromagnetic and weak interactions". In: *Physics Letters* 13.2 (Nov. 1964), pp. 168–171. ISSN: 0031-9163. DOI: 10.1016/0031-9163(64)90711-5.

[4] Peter W. Higgs. "Broken Symmetries and the Masses of Gauge Bosons". In: *Physical Review Letters* 13.16 (Oct. 1964), pp. 508–509. ISSN: 0031-9007. DOI: 10.1103/PhysRevLett.13.508.

[5] F. Englert et al. "Broken Symmetry and the Mass of Gauge Vector Mesons". In: *Physical Review Letters* 13.9 (Aug. 1964), pp. 321–323. ISSN: 0031-9007. DOI: 10.1103/PhysRevLett.13.321.

[6] J. P. Lees et al. "Evidence for an excess of $\bar{B} \to D^{(*)}\tau^-\bar{\nu}_\tau$ decays". In: *Physical Review Letters* 109.10 (May 2012). ISSN: 00319007. DOI: 10.1103/PhysRevLett.109.101802.

[7] J. P. Lees et al. "Measurement of an Excess of $\bar{B} \to D^{(*)}\tau^-\bar{\nu}_\tau$ Decays and Implications for Charged Higgs Bosons". In: *Physical Review D* 88.7 (Mar. 2013). DOI: 10.1103/PhysRevD.88.072012.

[8] M. Huschle et al. "Measurement of the branching ratio of $\bar{B} \to D^{(*)}\tau^-\bar{\nu}_\tau$ relative to $\bar{B} \to D^{(*)}l^-\bar{\nu}_l$ decays with hadronic tagging at Belle". In: *Physical Review D* 92.7 (Oct. 2015), p. 072014. ISSN: 1550-7998. DOI: 10.1103/PhysRevD.92.072014.

[9] R. Aaij et al. "Measurement of the ratio of branching fractions $B(\bar{B} \to D^{(*)}\tau^-\bar{\nu}_\tau)/B(\bar{B} \to D^{(*)}\mu^-\bar{\nu}_\mu)$". In: *Physical Review Letters* 115.11 (June 2015). DOI: 10.1103/PhysRevLett.115.111803.

[10] S. Hirose et al. "Measurement of the τ lepton polarization and $R(D^*)$ in the decay $\bar{B} \to D^{(*)}\tau^-\bar{\nu}_\tau$". In: *Physical Review Letters* 118.21 (Dec. 2017). DOI: 10.1103/physrevlett.118.211801.

[11] S. Hirose et al. "Measurement of the τ lepton polarization and $R(D^*)$ in the decay $\bar{B} \to D^{(*)}\tau^-\bar{\nu}_\tau$ with one-prong hadronic τ decays at Belle". In: *Physical Review D* 97.1 (Aug. 2018). DOI: 10.1103/PhysRevD.97.012004.

[12] R. Aaij et al. "Measurement of the ratio of the branching fractions $B(\bar{B} \to D^{(*)}\tau^-\bar{\nu}_\tau)/B(\bar{B} \to D^{(*)}l^-\bar{\nu}_l)$ using three-prong τ^- lepton decays". In: *Physical Review Letters* 120.17 (Aug. 2017). DOI: 10.1103/PhysRevLett.120.171802.

[13] R. Aaij et al. "Test of lepton universality with $\Lambda_b^0 \to pK^-l^+l^-$ decays". preprint on https://arxiv.org/abs/1912.08139. 2019.

[14] A. Abdesselam et al. "Measurement of $R(D)$ and $R(D^*)$ with a semileptonic tagging method". preprint on https://arxiv.org/abs/1904.08794. Apr. 2019.

[15] *Heavy Flavor Averaging Group (HFLAV) 2019 URL https://hflav.web.cern.ch.*

[16] R. Aaij et al. "Search for Lepton-Universality Violation in $B^+ \to K^+l^+l^-$ Decays". In: *Physical Review Letters* 122.19 (May 2019), p. 191801. ISSN: 0031-9007. DOI: 10.1103/PhysRevLett.122.191801.

[17] R. Aaij et al. "Test of lepton universality with $B^0 \to K^{*0}l^+l^-$ decays". In: *JHEP* 08.55 (May 2017). DOI: 10.1007/JHEP08(2017)055.

[18] T. Humair on behalf of LHCb collaboration. *Lepton Flavour Universality tests with heavy flavour decays at LHCb, Talk at Rencontres de Moriond EW 2019.*

[19] R. Aaij et al. "Test of lepton universality with $B^0 \to K^{*0}l^+l^-$ decays". In: (May 2017). DOI: 10.1007/JHEP08(2017)055.

[20] V. Cirigliano et al. "Two-loop effective theory analysis of π $(K) \to e\nu_e(\gamma)$ branching ratios". In: *Physical Review Letters* 99.23 (Dec. 2007). DOI: 10.1103/PhysRevLett.99.231801.

[21] A Abada et al. "Tree-level lepton universality violation in the presence of sterile neutrinos: impact for R_K and R_π". In: *JHEP02* (2013), p. 48. DOI: 10.1007/JHEP02(2013)048.

[22] Z. Maki et al. "Remarks on the Unified Model of Elementary Particles". In: *Progress of Theoretical Physics* 28.5 (Nov. 1962), pp. 870–880. ISSN: 0033-068X. DOI: 10.1143/ptp.28.870.

[23] R. N. Mohapatra et al. "Neutrino mass and baryon-number nonconservation in superstring models". In: *Physical Review D* 34.5 (Sept. 1986), pp. 1642–1645. ISSN: 05562821. DOI: 10.1103/PhysRevD.34.1642.

[24] A Masiero et al. "Probing new physics through μ-e universality in $K \to l\nu$". In: *Physical Review D - Particles, Fields, Gravitation and Cosmology* 74.1 (2006). ISSN: 15507998. DOI: 10.1103/PhysRevD.74.011701.

[25] A. Brignole et al. "Lepton flavour violating decays of supersymmetric Higgs bosons". In: *Physics Letters B* 566.3-4 (July 2003), pp. 217–225. ISSN: 0370-2693. DOI: 10.1016/s0370-2693(03)00837-2.

[26] E. Arganda et al. "Lepton flavor violating Higgs boson decays from massive seesaw neutrinos". In: *Physical Review D* 71.3 (Feb. 2005). ISSN: 1550-2368. DOI: 10.1103/physrevd.71.035011.

[27] C. Lazzeroni et al. "Precision measurement of the ratio of the charged kaon leptonic decay rates". In: *Physics Letters, Section B: Nuclear, Elementary Particle and High-Energy Physics* 719.4-5 (Feb. 2013), pp. 326–336. ISSN: 03702693. DOI: 10.1016/j.physletb.2013.01.037.

[28] V. Fanti et al. "The beam and detector for the NA48 neutral kaon CP violation experiment at CERN". In: *Nuclear Instruments and Methods in Physics Research, Section A: Accelerators, Spectrometers, Detectors and Associated Equipment* 574.3 (May 2007), pp. 433–471. ISSN: 01689002. DOI: 10.1016/j.nima.2007.01.178.

[29] F. Ambrosino et al. "Precise measurement of $\Gamma(K \to e\nu(\gamma))/\Gamma(K \to \mu\nu(\gamma))$ and study of $K \to e\nu\gamma$". In: *European Physical Journal C* 64.4 (2009), pp. 627–636. ISSN: 14346052. DOI: 10.1140/epjc/s10052-009-1177-x.

[30] M Adinolfi et al. "The tracking detector of the KLOE experiment". In: *Nuclear Instruments and Methods in Physics Research Section A: Accelerators, Spectrometers, Detectors and Associated Equipment* 488.1-2 (Aug. 2002), pp. 51–73. ISSN: 0168-9002. DOI: 10.1016/S0168-9002(02)00514-4.

[31] A. J. Buras et al. "$K^+ \to \pi^+\nu\bar{\nu}$ and $K_L \to \pi^0\nu\bar{\nu}$ in the Standard Model: status and perspectives". In: *Journal of High Energy Physics* 2015.11 (Nov. 2015), pp. 1–34. ISSN: 10298479. DOI: 10.1007/JHEP11(2015)033.

[32] A. V. Artamonov et al. "Study of the decay $K^+ \to \pi^+\nu\bar{\nu}$ in the momentum $140 < P_\pi < 199$ MeV/c". In: *Physical Review D - Particles, Fields, Gravitation and Cosmology* 79.9 (May 2009), p. 092004. ISSN: 15507998. DOI: 10.1103/PhysRevD.79.092004.

[33] E. Cortina Gil et al. "The beam and Detector of the NA62 experiment at CERN". In: *Journal of Instrumentation* 12.5 (May 2017). ISSN: 17480221. DOI: 10.1088/1748-0221/12/05/P05025.

[34] F. Ambrosino et al. "CHANTI: a fast and efficient charged particle veto detector for the NA62 experiment at CERN". In: *Journal of Instrumentation* 11.03 (Mar. 2016), P03029–P03029. DOI: 10.1088/1748-0221/11/03/p03029.

[35] E. Cortina Gil et al. "First search for $K^+ \to \pi\nu\bar{\nu}$ using the decay-in-flight technique". In: *Physics Letters, Section B: Nuclear, Elementary Particle and High-Energy Physics* 791 (Apr. 2019), pp. 156–166. ISSN: 03702693. DOI: 10.1016/j.physletb.2019.01.067.

[36] R. Ammendola et al. "The integrated low-level trigger and readout system of the CERN NA62 experiment". In: *Nuclear Instruments and Methods in Physics Research, Section A: Accelerators, Spectrometers, Detectors and Associated Equipment* 929 (Mar. 2019), pp. 1–22. ISSN: 01689002. DOI: 10.1016/j.nima.2019.03.012.

[37] B Angelucci et al. "TEL62: an integrated trigger and data acquisition board". In: *Journal of Instrumentation* 7.02 (Feb. 2012), pp. C02046–C02046. ISSN: 1748-0221. DOI: 10.1088/1748-0221/7/02/C02046.

[38] G. Anzivino et al. "Precise mirror alignment and basic performance of the RICH detector of the NA62 experiment at CERN". In: *Journal of Instrumentation* 13.07 (July 2018), P07012–P07012. DOI: 10.1088/1748-0221/13/07/p07012.

[39] NA62 collaboration. *2018 NA62 Status Report to the CERN SPSC*. Tech. rep.

[40] *GEANT4, URL https://geant4.web.cern.ch*.

[41] O. Behnke et al., eds. *Data analysis in high energy physics*. Weinheim, Germany: Wiley-VCH, 2013. ISBN: 9783527410583, 9783527653447, 9783527653430.